Spring 1996

Cross-tail current carriers in a two-dimensional equilibrium magnetotail model

Douglas Johnston Larson
University of New Hampshire, Durham

INFORMATION TO USERS

CROSS-TAIL CURRENT CARRIERS IN A TWO-DIMENSIONAL

EQUILIBRIUM MAGNETOTAIL MODEL

BY

DOUGLAS JOHNSTON LARSON
B.S.E.E., University of New Hampshire, 1986
M.S., University of New Hampshire, 1989

DISSERTATION

Submitted to the University of New Hampshire
in Partial Fulfillment of
the Requirement for the Degree of

Doctor of Philosophy

in

Physics

May, 1996

UMI Number: 9627160
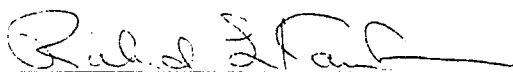
UMI
300 North Zeeb Road
Ann Arbor, MI 48103

This dissertation has been examined and approved.

Dissertation Director, Richard L. Kaufmann
Professor of Physics
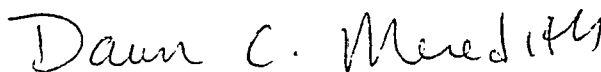
John R. Calarco
Professor of Physics
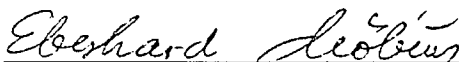
Terry G. Forbes
Research Professor of Physics and Earth,
Oceans, and Space
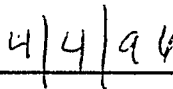
Dawn C. Meredith
Associate Professor of Physics

Eberhard S. Möbius
Professor of Physics and Earth,
Oceans, and Space

4|4|94
Date

This dissertation is dedicated to

my parents

ACKNOWLEDGMENTS

I would like to express my thanks to my advisor, Professor Richard L. Kaufmann. Without his thoughtful guidance (pushing and prodding?) and invaluable help, this thesis would never have been possible. I am grateful to Drs. John Calarco, Terry Forbes, Dawn Meredith, and Eberhard Möbius, for their helpful suggestions and their critical reading of this thesis. I also thank Dr. Lynn Kistler for her help and humor.

My long time office-mate Dr. Chen Lu deserves special appreciation for all her help, friendship, and above all her dumplings. Dr. Guang Yang also helped me understand critical phrases of the Chinese language. Bryan Ball and Alan Tutein have helped with generating many of the plots in the final revision of this thesis and deserve special recognition. I also acknowledge Dr. Ben Hersh, Korac MacArthur, Dr. "Spare Doug" Biesecker, "Silent" Mike, Dean, Scott, and the entire Friday night pizza posse who have kept a tradition alive in the face of much abuse from the Tin Palace staff.

Future graduate students should remember five survival rules for the University of No Holidays (UNH). One, never become too useful to your advisor (or too useless); two, do not point out how long a fellow grad student has spent working on their thesis, somehow you will end up with added years for your *hubris*; three, always give an annual report to your committee; four, if you eat the cookies you *must* attend the talk; and five, there is NO rule five! There other rules which must remain secret until you learn through experience :-)

iv

TABLE OF CONTENTS

LIST OF TABLES

LIST OF FIGURES

ABSTRACT

CROSS-TAIL CURRENT CARRIERS IN A

TWO-DIMENSIONAL EQUILIBRIUM MAGNETOTAIL

by

Douglas Johnston Larson

University of New Hampshire, May, 1996

The purpose of this study is to gain physical insight into how charged particles, that violate the guiding center approximations, contribute to cross-tail current in a self-consistent plasma sheet. A technique to generate self-consistent two-dimensional (2D) current sheets is described. Groups of monoenergetic protons are followed in a model magnetic field. The sample current sheets are characterized by resonant quasiadiabatic and stochastic orbits. Several ion and electron groups are combined to produce a plasma sheet in which the charged particles carry the currents needed to generate the magnetic field in which the orbits are traced. An electric field also is required to maintain charge neutrality. Numerous plasma parameters are calculated for the generated current sheets. It was found that ions which were trapped near $z = 0$, ions that magnetically mirrored throughout the current sheet, and ions that mirrored near the Earth all were needed in order to produce the model current sheets.

Research Advisor: Professor Richard L. Kaufmann

Chapter I

INTRODUCTION

The interaction of the solar wind with the dipole field of the Earth creates a rich local environment for plasma study due to the many distinct plasma regions. The region of space on the nightside of the Earth, comprising the antisunward portion of the magnetosphere, is called the magnetotail. This name is due to the characteristic elongated shape of magnetic field lines traced in the observed fields. When the solar wind plasma connects the interplanetary magnetic field (IMF) to the Earth's magnetic field, the characteristic dipole field lines are stretched with some actually disconnecting from their counterpoint in the other hemisphere. These open field lines form the northern and southern tail lobes with their opposing fields. The region where the lobes separate forms a current sheet. This current sheet, called the neutral sheet, contains exciting plasma phenomena that directly affect the study of magnetospheric substorm triggering mechanisms.

The overall goal of the present study is to obtain a better physical understanding of the structure of the neutral sheet. This work introduces the Self Consistent Orbit Tracing (SCOT). This technique is similar to that employed by *Kaufmann and Lu* [1993] and generalizes their results for two-dimensional magnetotail models. The underlying assumptions of the SCOT are substantially different from those normally employed in simulations.

Most workers are familiar with plasma simulations which are carried out by injecting particles into a fixed spatial region. The simulation technique requires knowledge about

the source of the particles and the boundary conditions. An initial magnetic and electric field configuration is needed to start the simulation, but detailed knowledge about the fields is not required. The electric and magnetic fields generated by the particles are calculated self-consistently as the system evolves in time.

In contrast, the SCOT method used here requires that the basic magnetic and electric fields be known throughout the region of interest. However, very little is assumed about the particles, their sources, or any boundary conditions. The plasma is constructed from individual particle trajectories with the principal goal of finding a distribution of ions and electrons that will as nearly as possible generate the preselected magnetic field. One major consequence of this is that we can study only steady state conditions. Since this work does not evolve a plasma from initial conditions but constructs it from individual particle trajectories, the approach should be considered a *particle experiment* rather than a simulation. The utility of the SCOT technique is demonstrated by the construction of several self-consistent models of the magnetotail.

In this chapter a background section is presented on two approaches to plasma physics. Information about the orbital regimes that are used to classify particle orbits will also be presented. A review of papers on magnetotail current sheets is also given as well as a more detailed description of the SCOT. Results of the original one-dimensional model SCOT technique of *Lu* [1993] will also be discussed.

1.1 Background

A weakly couple plasma is a statistical system of mobile charged and neutral particles where the kinetic energy of the individual particles is large compared to the potential energy. If the position and velocity of each individual particle that comprises the system

were known the plasma would be completely described. The Lorentz force law, which is the equation of motion for charged particles, in conjunction with Maxwell's equations, which describes the electromagnetic field dynamics, can exactly describe a plasma. As reference we state the Lorentz force law,

$$F = q(E + v \times B) \,,$$
(1.1)

and Maxwell's equations for a vacuum,

$$\nabla \bullet E = \rho/\varepsilon_o$$

$$\nabla \times E = -\frac{\partial B}{\partial t}$$

$$\nabla \bullet B = 0$$

$$\nabla \times B = \mu_o J + \mu_o \varepsilon_o \frac{\partial E}{\partial t}$$

(1.2)

In light of the fact that it would be nearly impossible to use these equations to follow all of the particles composing a particular plasma, considerable effort is devoted by plasma physicists to devising useful approximations to these equations. The two most popular approaches are kinetic theory and fluid theory.

The fluid theory, where particles make up fluid elements analogous to those in ordinary hydrodynamics, is treated in many excellent texts [*Chen*, 1990; *Krall and Trivelpiece*, 1986; *Nicholson*, 1992]. *Tajima* [1989] discusses the computer simulation techniques for solving the magnetohydrodynamic (MHD) equations of the fluid theory. Although the MHD approach is used to solve a rich variety of problems it is not the focus of this work.

Kinetic theory simulation techniques using particles can be found in [*Birdsall and Langdon*, 1991; *Hockney and Eastwood*, 1988]. This work does not evolve a plasma from initial conditions but does construct a plasma from individual particle trajectories. Particle

experiments require that the plasma be comprised of only those particles that contribute to self consistency. A brief description of kinetic theory as it pertains to this study follows.

1.2 Kinetic Theory

The kinetic theory uses the Lorentz force law in a six dimensional phase space defined by the position and velocity. The number of particles of species s occupying some unit of this space at a time t defines the distribution function, $f_s(\mathbf{x}, \mathbf{v}, t)$. The evolution of this distribution function, when particle collisions are unimportant, is the Vlasov equation,

$$\left[\frac{\partial}{\partial t} + \mathbf{v} \cdot \frac{\partial}{\partial \mathbf{x}} + \frac{q_s}{m_s}(\mathbf{E}(\mathbf{x}, t) + \mathbf{v} \times \mathbf{B}(\mathbf{x}, t)) \cdot \frac{\partial}{\partial \mathbf{v}}\right] f_s(\mathbf{x}, \mathbf{v}; t) = 0. \tag{1.3}$$

The derivation of the Vlasov equation from the Klimontovich equation can be found in *Ichimaru* [1973]. The time independent version of the Vlasov equation which is used in this study is:

$$\left[\mathbf{v} \cdot \frac{\partial}{\partial \mathbf{x}} + \frac{q_s}{m_s}(\mathbf{E}(\mathbf{x}) + \mathbf{v} \times \mathbf{B}(\mathbf{x})) \cdot \frac{\partial}{\partial \mathbf{v}}\right] f_s(\mathbf{x}, \mathbf{v}) = 0. \tag{1.4}$$

The distribution function is an observable that provides a statistical description of the plasma. By taking velocity moments of the distribution function, macroscopic variables such as density, bulk velocity, current density, temperature, heat flux, and the pressure tensor can be calculated. These quantities are more easily interpreted and are given in Appendix A.

The combination of Maxwell's equations and the Vlasov equation is the *Vlasov-Maxwell* approach. The solution of the Vlasov-Maxwell equations requires that the distribution function be expressed in an analytic form, such as a Maxwellian distribution, or be constructed from single particle trajectories in a self-consistent fashion. The former approach will be discussed as background to the section on the SCOT as an example of using

a Vlasov-Poisson method. The latter method will be discussed as it relates to the SCOT which is a Vlasov-Ampere method.

1.3 Previous Studies

This review begins with some of the results at the microscopic end of the spatial scale devoted to the understanding of single particle orbits in tail-like magnetic fields. The work concerning chaotic and resonant particle orbits motivates the choices made in the direction taken with this research. Next, the projects which are currently being carried out on the Earth's magnetic field with particular emphasis to the magnetotail will be examined. The relative strengths and deficiencies inherent to each of the studies will be discussed. Finally, an overview of the approach taken in this work will be presented.

Orbit Types and Magnetotail Regions

In the course of the many studies of particle orbits in one-dimensional field reversal regions designed to reflect magnetotail characteristics [*Chen*, 1992], a nomenclature for labeling the orbital regimes has come into use. When typical magnetotail parameters are used, four distinctive orbital regimes are found; guiding-center, resonant, chaotic, and non-resonant [*Kaufmann and Lu*, 1993]. In order to quantify these regimes for a simple parabolic magnetic field reversal, *Büchner and Zelenyi* [1985; 1989] introduced the κ parameter

$$\kappa = B_{zo}\left[\frac{Lq}{B_{xo}mv}\right]^{1/2} \tag{1.5}$$

where q, m, and v are the ion charge, mass, velocity, respectively. The constant parameters B_{xo} and B_{zo} are representative values of a one-dimensional tail field where L is the characteristic thickness of the plasma sheet. This was later generalized while studying a modi-

fied Harris equilibrium field [*Harris*, 1962] to be

$$\kappa^2 = \frac{R_{min}}{\rho_{max}},\qquad(1.6)$$

where R_{min} is the minimum magnetic field line radius of curvature for the magnetotail

model being studied and ρ_{max} is the maximum particle Larmor radius [*Büchner and Zele-*

nyi, 1989].

The guiding-center regime corresponds to $\kappa > 2$ because nonrelativistic ions in this

kappa range can be adequately described by the guiding center approximations [*Northrup*,

1963]. A guiding center orbit is analyzed by separating the rapid spiral motion about a field

line from the slow drift of the cyclotron averaged particle location or guiding center. These

guiding center particles often are referred to as "adiabatic" because the magnetic moment

$\mu = mv_\perp^2/(2B)$ is nearly conserved. Thermal ions and electrons have $\kappa > 2$ in the radi-

ation belts and near-Earth tail. Here the dipole nature of the field dominates due to its large

radius of curvature and the particles' relatively small Larmor radius. The particles only

cross the $z = 0$ plane once during each current sheet interaction. During this brief period

of lower **B** they can experience gradient and curvature guiding center drifts.

At the opposite extreme are particles in the limit of very small κ. These particles,

which we call non-resonant, were originally studied by *Speiser* [1965]. Speiser orbits are

characterized by separating their rapid bounce motion in the solar magnetospheric z direc-

tion from the slow semicircular cyclotron motion in the x-y plane, about B_z, of the bounce

averaged particle location. Ions in the distant tail, near a neutral line, and in the very thin

plasma sheet that is present at the end of a substorm growth phase are of the Speiser type.

Unlike the adiabatic particles, Speiser particles do not conserve their magnetic mo-

ment during their many plasma sheet interactions. However, when the particle eventually leaves the current sheet, the magnetic moment returns very nearly to the initial value it had when it entered the current sheet. This is a consequence of the action integral

$$I_z = \frac{1}{2\pi} \oint p_z dz \qquad (1.7)$$

being nearly conserved [*Speiser*, 1970; *Sonnerup*, 1971; *Whipple et al.*, 1986]. The feature of Speiser orbits most important to remember for magnetotail studies is that they are insensitive to the exact value of kappa. Nonresonant ions experience relatively little pitch angle scattering while encountering the current sheet. Given certain pitch and phase angles they can bounce back and forth between north-south reflection points contributing substantial $j_y(z)$ beyond the thickness of the current sheet [*Kaufmann et al.*, 1994]. Therefore, in order to generate a self-consistent current sheet, the number of non-resonant ions used must be low.

Guiding center motion breaks down for most ions when the dipole field no longer dominates. This point is usually between 5 R_E and 15 R_E in the magnetotail [*Pulkkinen et al.*, 1992a]. The two intermediate kappa regimes, resonant and chaotic, are typical of the midtail region. The ions which have large changes in their magnetic moment upon interacting with the current sheet and having comparable bounce and cyclotron periods are chaotic [*Kaufmann et al.*, 1993a]. These particles can exhibit stochastic orbits for some κ values [*Chen and Palmadesso*, 1986; *Büchner and Zelenyi*, 1987]. Many of these stochastic ions eventually leave the current sheet with such a small pitch angle that they can completely escape from a one-dimensional model field [*Gray and Lee*, 1982; *Kaufmann et al.*, 1994].

The resonant orbit class tends to follow very simple predictable orbits. Resonant orbits are symmetric [*Chen and Palmadesso*, 1986; *Chen et al.*, 1990]. They are similar in

appearance to Speiser orbits that involve small half-integral numbers of small north-south-north oscillations through the current sheet. As defined by *Büchner and Zelenyi* [1989], there are $N\pi$ radians of the bounce-type oscillations during each current sheet encounter. There are $(N+1)$ crossings of the $z = 0$ plane with this definition. The relationship between N and κ has been found for Harris type models to be approximately

$$N = \frac{0.80}{\kappa} - 0.5 \tag{1.8}$$

[*Chen*, 1992; *Ashour-Abdalla et al.*, 1993; *Kaufmann and Lu*, 1993]. Therefore, $\kappa = 0.53$ resonant ions have $N = 1$. The smallest κ resonance value for a modified Harris model is approximately $\kappa_r = B_{zo}/B_{xo}$ [*Burkhardt and Chen*, 1991].

Speiser orbits differ from resonant orbits in that they have enough energy during z oscillations to reach or even exceed the current sheet thickness. An example and discussion of resonant particle invariant tori is found in *Kaufmann and Lu* [1993]. A self-consistent one-dimensional current sheet using a modified Harris equilibrium model was generated using resonant particles and is described in *Lu*, [1993] and *Kaufmann and Lu*, [1993]. The technique used took advantage of the relative predictability of the orbits and their sensitivity to the κ parameter.

1.4 Magnetohydrodynamic Simulations

The magnetohydrodynamic (MHD) approach to plasma physics, where the plasma can be treated as a fluid, can be derived by taking velocity moments of the Vlasov equation, thereby trading the seven-dimensional phase space of the kinetic approach for the three spatial dimensions and time [*Nicholson*, 1992]. This summing operation will destroy the details of any beam structures in the velocity space of the distribution function in favor of macroscopic plasma processes. The interaction between waves and particles is lost in

MHD so velocity dependent effects such as Landau-damping cannot be studied. Because ideal-MHD assumes no electric field parallel to the magnetic field (except in the case of discontinuities such as shocks), the assumption of infinite plasma conductivity breaks down.

The application of MHD to the magnetotail is covered in a series of papers in *Lui* [1987]. A review of quasi-static MHD processes in the magnetosphere was done by *Voigt and Wolf* [1988] while addressing the problem of whether a "ground state" energy for the magnetosphere can be defined.

The global resistive MHD simulations of *Ogino et al.* [1994] attempt to evolve a complete magnetosphere. The use of resistive MHD is the major assumption of the study since it incorporates an electric field parallel to the magnetic field. They further assume the Earth's dipole field and the particle input rate of the solar wind into their simulation box. The fields are calculated self-consistently and open field lines are permitted. The method used to advance their simulation is the leapfrog method combined with a two step Lax-Wendroff scheme [*Tajima*, 1993]. Although they use a solar wind temperature in the simulations roughly an order of magnitude higher than observations, they claim the results are temperature insensitive. The interplanetary magnetic field (IMF) is also a parameter in their model and permits them to study dayside reconnection as well as substorm growth and expansion phases.

Hesse and Birn [1994] concentrate on simulating the magnetotail region. They use the three-dimensional equilibrium configurations of *Birn* [1987, 1989]. Their simulations assume no gravity, no dipole, no IMF, and an isotropic pressure. The resistive MHD equations are integrated by an explicit leapfrog method. A uniform and constant finite resistivity

was imposed on their system. This work has been able to replicate the larger flank B_z relative to a low neutral sheet B_z during quiet times which was reported in the observations [*Fairfield*, 1979].

In contrast, a modified set of single fluid equations, called magnetoplasma dynamics (MPD) has been proposed [*Winglee*, 1994]. Essentially, this method includes electron terms from the generalized Ohm's law equation [see *Krall and Trivelpiece*, 1986]

$$\mathbf{E} + \mathbf{V} \times \mathbf{B} \cong \eta \mathbf{J} + \frac{1}{en_e}(\mathbf{J} \times \mathbf{B} - \nabla P_e) \ . \tag{1.9}$$

Winglee's two-dimensional simulation is performed using geocentric solar magnetic (GSM) coordinate system. The electric and magnetic fields directly associated with the flow of plasma around an object or body are given the subscript b and plasma currents tied to the surface of the body are given the subscript s. The new effective resistivity used by Winglee, $\eta_{eff} = (\mathbf{J}_s \times \mathbf{B}_b)_y / (en_e(\mathbf{J}_b)_y)$, is claimed to spread the dissipation rate more uniformly across the current enabling better magnetotail energy storage during substorm growth. The author shows that this method can be successfully applied to yield surface current effects at both the dayside magnetopause and the magnetotail. These are two regions which are difficult to study using MHD models. However, as with all the fluid methods discussed here, the method requires a supercomputer.

1.5 Local Kinetic Simulations

Pritchett [1991, 1992] uses a two-dimensional simulation model based on the Darwin approximation to Maxwell's equations [*Birdsall and Langdon*, 1985]. In this approximation the transverse displacement current term is dropped from the Ampere's equation. Electrons are assumed to be a neutralizing background fluid. Protons are loaded on a grid consistent with an assumed drifting Maxwellian [*Pritchett*, 1991]. His initial

magnetic field is a quasi parabolic equilibrium model [*Lembege and Pellat*, 1982]. Upon

progressing his particles, the new j_y current is accumulated on the simulation grid directly

from the canonical momentum using an area weighting scheme. The new **B** is found by

solving Ampere's equation, $\nabla^2 A_y = -(4\pi/c)j_y$. The vector potential is found via an

iterative method that divides A_y into assumed initial and perturbed components. The

perturbed portion is extrapolated and fed back until the solution converges. This simulation

method is used to study current sheet equilibria.

Hybrid particle in cell (PIC) codes use a grid. In this method electrons are consid-

ered to be a cold, massless fluid. Usually particles are loaded on the grid. All particles are

then advanced with the same timestep. Charge is assigned to the nearest grid point. The

fields are recalculated with the resulting current; then the process repeats itself. In the case

studied by *Burkhardt* [1992a], a drifting Maxwellian boundary distribution of inflowing

protons is assumed. Each trajectory is integrated until it leaves the simulation domain. At

each timestep in the integration the particle contribution is summed to the grid points via

linear interpolation. The sums are then normalized at each cell to the number at the bound-

ary, then the fields are recalculated and the process is iterated. Burkhardt requires that there

be no trapped particles and he varies the boundary conditions with time.

1.6 Plasma Sheet Studies Using Test Particles

Although the Lorentz equation of motion for a charged particle in an electromag-

netic field is straightforward, the numerical labor necessary to follow a statistically useful

number in a reasonable amount of time has only come about with the advent of computers.

Even with the guiding center approximations of *Northrup* [1963] to reduce computation,

workers still did not expend valuable computer resources in computing particle trajectories [*Speiser*, 1965, 1967; *Cowley*, 1971; *Eastwood*, 1972, 1975]. In order to study nonadiabatic guiding-center particle pitch angle diffusion in a Harris type model, *Gray and Lee* [1982] began using the rational polynomial extrapolation to integrate the equations of motion. This method is faster than Runge-Kutta but it sacrifices the detail of a trajectory with a finer timestep.

The wholesale injection of vast numbers of ions in a prescribed magnetic field model at two arbitrary injection locations to study the resulting distributions came into popularity with the availability of relatively inexpensive supercomputer time [*Ashour-Abdalla et al.*, 1990]. Using 60,000 particles in a test simulation with a reduction of the *Tsyganenko* [1989] model to its noon-midnight plane had become routine by 1993 using a fourth order Runge-Kutta method [*Ashour-Abdalla et al.*, 1993]. The study method is not self-consistent since it neither addresses electrons in the magnetotail or selects ions that will generate the prescribed magnetic field. In addition, the following of ions in the $K_p = 1$ version of T89 introduces many problems associated with the model's range of validity such as excessive flaring beyond $x_{sm} = -30$ R_E, the unrealistic B_{zo} depression near $x_{sm} = -20$ R_E in the equatorial plane [*Kaufmann et al.*, 1993], and the model creator's warning against using it beyond $x_{sm} = -70$ R_E [*Stern and Tsyganenko*, 1992]. In addition, the use of only the $y = 0$ noon-midnight slice is not divergence free. Given the complexity of the empirical model used it seems difficult to envision what effect a particular component of the model may have on an ion orbit. Separating fundamental physical understanding from modeling effects could give rise to anomalous results.

1.7 The Self-Consistent Orbit Tracing Method (SCOT)

The SCOT resembles a *Bernstein, Green and Kruskal* [1957] or BGK study of large-amplitude plasma waves more than a plasma simulation or the test particle approach. The BGK technique assumes that it is possible to find a self-consistent equilibrium distribution of ions and electrons for virtually any preselected electrostatic potential. Subject to the boundary conditions of the problem, the electrostatic potential, $\Phi(\mathbf{x})$, is produced self-consistently by the distribution functions through Poisson's equation

$$\nabla^2 \Phi(\mathbf{x}) = 4\pi e \left[\int_{-\infty}^{\infty} f_e(\mathbf{x}, \mathbf{v}) d^3v - \int_{-\infty}^{\infty} f_i(\mathbf{x}, \mathbf{v}) d^3v \right]. \tag{1.10}$$

The method has been used to generate models of nonlinear wave trains, solitons, static spatial structures, and shocks. The resulting plasmas often contain groups of trapped and untrapped particles, with trapping in this context meaning bound in an electrostatic potential well.

Self-consistency for the SCOT means that, to a good approximation, the final collection of ions and electrons carries the electric current that is needed to generate the preselected magnetic and electric fields in which the ion orbits were traced.

The first step is to trace many groups of individual ion orbits in the original magnetic and electric fields. The strength of the SCOT method lies in its capability to calculate and save complete ion distribution functions $f_i(\mathbf{x}, \mathbf{v})$ in the region of interest. These $f_i(\mathbf{x}, \mathbf{v})$ are generated by binning the timestep of many individual ion trajectories in the phase space location of the distribution function. The Lorentz equation of motion,

$\mathbf{F} = q_s(\mathbf{E}(\mathbf{x}) + \mathbf{v} \times \mathbf{B}(\mathbf{x}))$, is used to calculate the exact position, $\mathbf{x}$, and velocity, $\mathbf{v}$, of the individual ions in the preselected electromagnetic field. The ion density and current can

then be calculated as a velocity moment of the distribution function.

The use of very accurate trajectory tracing permits the inclusion of all non-guiding-center effects. In our studies to date, each particle group has consisted of 1000 ions randomly selected from a monoenergetic energy distribution. Ion orbits are traced from a starting point until they have drifted Earthward well beyond the region of interest. Earthward drift is produced by a uniform dawn to dusk electric field. The ion trajectories are then traced backwards in time from the starting point until they have moved far enough tailward so they will not again enter the region of interest. The particle starting points and the specific points at which orbit tracing is stopped therefore have little significance. Physically, all current sheet particles come in from tailward of our region of interest and drift Earthward completely through the region we wish to study. The starting point and starting distribution are used primarily as a way to label a group of particles. No specific boundary conditions are imposed at the edges of our region of interest, and no physical boundaries exist in the system except for the very rare particles that hit the Earth.

The second step is to include the effects of electrons. The electron current is included by assuming charge neutrality, and by assuming the electrons are isotropically distributed. Additionally it is assumed that the electrons have $1/7$ the energy of ions in each box [*Baumjohann et al.*, 1989]. The assumed energy, electron mass, and the tail field insure that the electrons obey the guiding center approximations. Step three involves adding the ion and electron currents together for each group.

Step four involves finding some combination of the ion and electron groups that can satisfy Amperes law for the preselected magnetic field,

$$J_{goal}(\mathbf{x}) = (1/\mu_o)\nabla\times\mathbf{B}(\mathbf{x}) = \sum_{g=1}^{k} \omega_g[q_{i,g}\int \mathbf{v}f_{i,g}(\mathbf{x},\mathbf{v})d^3v + J_{e,g}(\mathbf{x})] . \qquad (1.11)$$

Here g is the group number, k is the total number of plasma groups, and ω_g is a weight

assigned by a least squares fitting routine. The fitting procedure is used to find those groups

that can best sustain the preselected electric and magnetic fields in which the orbits were

traced. The selection of weighting factors for each group is done to make the final current

sheet as nearly self-consistent as possible. One restriction that has been imposed is that a

group is discarded if its inclusion does not enhance the self-consistency of the final plasma

at a 95% confidence level. The procedure is iterative in the sense that the electron contri-

bution can still be insufficient to achieve self-consistency so a new electric field could re-

place the previous electric field and the ion groups could then be retraced. More detail of

the SCOT implementation is given in chapter three.

The principal difference between our BGK-type analysis and a computer simulation

is that we assume that magnetometer measurements are adequate to provide a reasonable

model of the actual tail magnetic field. Our method imposes a fixed magnetic field every-

where but no extra explicit conditions at the boundaries. Unlike a simulation, or a test par-

ticle method, no assumptions are made about particle sources. Groups of particles are

randomly started at various locations and with various angular distributions. Groups are

only retained if they carry a portion of the current required to sustain the magnetic field.

The similarity to the BGK analysis lies in treating the source of the electric or magnetic

field, charge or current, through Maxwell's equations. Since the SCOT uses a prescribed

magnetic field, the current is determined through Ampere's law. The BGK method in con-

trast assumes a preselected electrostatic potential and determines the potential through

Poisson's equation.

1.8 The SCOT: Harris Model Results

An earlier version of the SCOT technique was used by *Lu* [1993] to construct an

approximately self-consistent one-dimensional (1-D) model magnetotail. Although orbits

are always traced in three dimensions, the model is referred to as a 1-D magnetotail because

the modified Harris current sheet magnetic field was used [*Harris*, 1962]. The modified

Harris model consists of a constant B_{zo} and a $B_x(z) = B_{xo} \tanh(z/L)$ that varies only in

the z direction.

The study of *Lu* [1993] found that κ is a good parameter to use when classifying

particle orbits. Two intermediate κ regimes are common in the midtail region; resonant

particles, where $\kappa = 0.53, 0.32,$ or $0.23,$ and chaotic particles: where $\kappa = 0.82, 0.40,$ or

0.27. Three types of orbits which carry different current distributions were identified; ring

like, mirror, and untrapped. Contributions from all three types were needed in order to gen-

erate a typical quiet-time self-consistent current sheet. The generated plasma exhibited

"firehose" instability in the current sheet. A density of 1 particle/cm^3 was required to carry

the cross tail current. This is about three times larger than is typically observed in the

Earth's magnetotail in the $x = -10$ to $-30\,R_E$ range. An unrealistically high density is need-

ed because there is no net cross tail drift of those charged particles that are trapped in a 1-

D magnetic field [*Stern and Palmadesso*, 1975]. Trapped particles carry cross tail current

near the center of the current sheet, but an equal and opposite cross-tail current in the outer

current sheet. Only untrapped particles carry a net cross-tail current in the 1-D model.

It is well known that streaming or a strong anisotropy, near the firehose instability

limit $\mu_o(P_{\parallel} - P_{\perp})/B^2 = 1$, is needed at the edge of any 1-D current sheet to produce

force balance [*Rich et al.*, 1972; *Cowley*, 1978]. The problem is that 1-D models have no x dependence, so require anisotropies much larger than those observed to balance what is usually referred to as the tension force of the sharply curved magnetic field lines. This effect was reflected in the temperature which was not isotropic for $|z| > 0.1$ R_E in this plasma. At the edge $T_\parallel / T_\perp \cong 3$. For these reasons, it was concluded that no 1-D current sheet can produce a reasonable model of the middle magnetotail, below approximately 30 R_E.

Much of the physics learned in the one-dimensional study has helped in developing the two-dimensional fitting methodology. The identification of resonant energies and the various types of orbits have seen direct application in analyzing groups of particles. The low density and very high energies needed by the modified Harris equilibrium model indicated that a more realistic $B_z(x)$ is needed. The results of the *Lu* [1993] study showed that the physics that can be observed in the real magnetotail can only be partially understood with a one-dimensional model. Equilibrium models of the Harris type seem a natural advance for workers doing particle orbit studies but they must be extended to higher dimensions.

A new two-dimensional magnetotail model will be presented in chapter two that uses a Harris type equilibrium field for the magnetotail superposed with an Earth centered dipole and a ring current field. Chapter three will present the underlying software paradigm of this work. Chapter four presents the results from three cases. Chapter five is a discussion of the results in terms of force and energy. The final chapter summarizes the results and speculates on future directions of the methodology developed.

Chapter II

THE MODEL MAGNETOTAIL

The test particle method employed in this thesis requires that many ions be traced

in a model magnetotail field that resembles the noon-midnight field with special emphasis

on the plasma sheet of the midtail region. Since the ion motions cannot be described by the

guiding center approximations in the neutral sheet region [*Kaufmann and Lu*, 1993], the

complete Lorentz equation of motion is used for all particle tracing. The magnetic field

chosen must therefore be relatively simple in order to minimize computing time.

2.1 Global magnetospheric models

The relative quality of a magnetosphere model can really only be determined by

how faithfully it can match *in situ* observations of satellites and whether it is easy to use.

The most elaborate series of models to date are those developed by N. A. Tsyganenko and

his collaborators [*Tsyganenko and Usmanov*, 1982; *Tsyganenko*, 1987; *Tsyganenko*, 1989;

Tsyganenko et al., 1993; *Tsyganenko and Peredo*, 1994]. The most widely accepted version

of these models is the T89 model [*Tsyganenko*, 1989]. In this model, the ring and tail

current systems as well as the Earth's internal field and the magnetopause contributions to

the total field are each represented by separate mathematical expressions. The resulting

expressions have 22 polynomial coefficients and 13 parameters with physical meanings

such as ring current characteristic radius and current sheet half thickness. The coefficients

are set by a least squares fitting procedure involving an averaged magnetic field dataset of
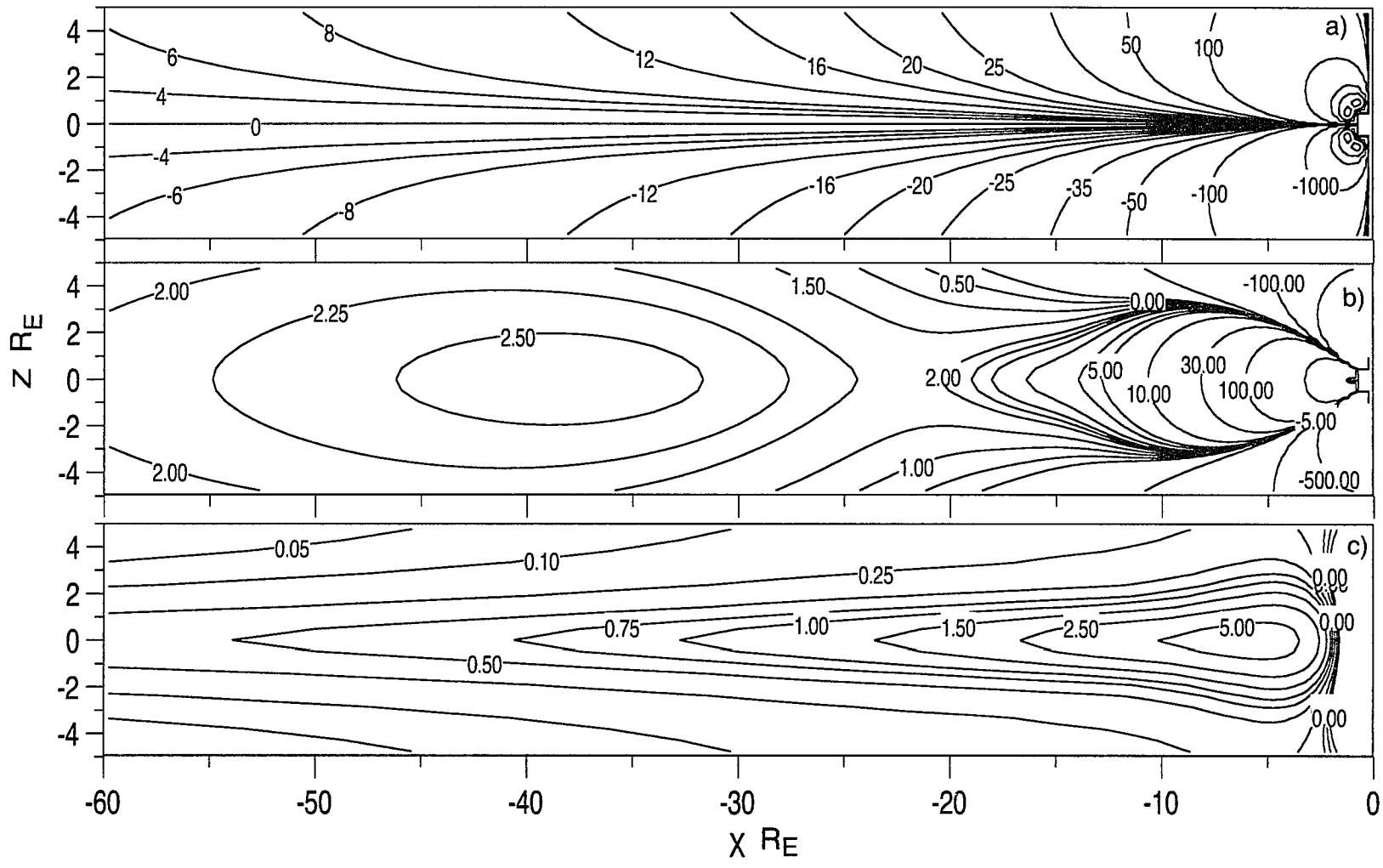
Figure 2.1: Tsyganenko 1989 Model, $Kp = 4$a) B_x, (nT) b) B_z, (nT) c) j_y, (nA/m^2).

over 45000 points. The magnetic field datasets come from the IMP and HEOS series of satellites. The satellites and the datasets of the T89, as well as its descendent empirical models, are described by *Fairfield et al.* [1994].

Although the T89 model makes use of an extensive dataset, it does have limitations [*Kaufmann et al.*, 1993a, 1993b]. First, the satellites did not exceed 70 R_E, so the model is unlikely to be realistic beyond this point. Second, because the model lacks a true magneto-pause, for all K_p levels the flank regions, $|y| > 20$ R_E, are unrealistic. Third, strong Birke-land currents mapped to the flanks [*Kaufmann et al.*, 1993b]. Fourth, a neutral line and a region of very weak B_z exist in the $K_p = 0$ version of T89. The T89 model can be con-sidered reliable for higher K_p levels in the $(-70\ R_E < x_{sm} < 10\ R_E)$, $(0 < y_{sm} < 20\ R_E)$ region. The K_p index is an indicator of solar wind disturbance ranging from 0 to 9 [*Parks*, 1991].

Despite being a reliable empirical model in the midtail region, the T89 model uses far too much computer time to be the primary magnetic field in a test particle study. How-ever, since the T89 models the average magnetic field of many satellite measurements, it can be considered useful as a guide in developing a simpler model that can represent a lim-ited region of the magnetotail. This is precisely what has been done using the $K_p = 4$ model in the noon-midnight plane as the guide. The B_x and B_z magnetic field components and the current density, j_y, for the nightside are shown in figure 2.1. The next sections will describe the details of the new model.

2.2 A simple magnetotail model

The model magnetotail developed for this work is a superposition of three fields; an Earth centered dipole, the magnetic field generated by a ring current [*Tsyganenko and*

Usmanov, 1982], and an equilibrium tail field [*Zwingmann*,1983] plus a uniform B_{zn}. The final model configuration is then

$$\mathbf{B}(\mathbf{x}) = \mathbf{B}_{Dipole}(\mathbf{x}) + \mathbf{B}_{Ring}(\mathbf{x}) + \mathbf{B}_{Tail}(\mathbf{x}) + B_{zn}.$$ (2.1)

Since each of the main components of the model taken individually are divergence free

$\nabla \bullet \mathbf{B} = 0$, the entire model is also divergence free. It should be noted that if we were to force $y = 0$ everywhere only the equilibrium tail field would be divergence free. The complete model would then not be self consistent. The present work uses 3-D versions of the dipole and ring current fields so the mirroring of particles at low altitudes is as realistic as possible. Two dimensional versions of these modules are more appropriate in other studies.

The components of the models presented here will be expressed in solar magnetospheric coordinates. In this coordinate system the positive x axis points from the center of Earth toward the Sun, the z axis is directed to the north along the geomagnetic dipole axis, and the y axis is perpendicular to the Earth-Sun line and points from dawn to dusk.

The Dipole Field

Since the compass was discovered to be an aid to navigation, interest in the Earth's magnetic field and its secular changes has only increased. A chronology beginning with the observation by William Gilbert in 1600 that the Earth is a great magnet through spherical harmonic expansion techniques pioneered by Gauss in 1835 and the modern high order models based on extensive ground station data are detailed in the book by *Akasofu and Chapman* [1972]. As early as 1635 Gellibrand noted that the geomagnetic field of the Earth slowly changes. This stems from a number of factors including the slightly squashed shape of the planet from an ideal sphere and the resulting complex dynamics of the molten magma below the crust. The currents generated by the motion of the magma in the earth's interior

account for nearly 99% of the magnetic field observed at ground level. This field can be approximated through the use of spherical harmonic expansions [*Stern*, 1976].

The details of expansion models which include secular variations to the Earth's field are unnecessary to this study of current carriers in the midtail region. In this region the geomagnetic field contribution is essentially a dipole and will be treated as such. The vector magnetic potential of a dipole is given by

$$\mathbf{A}_{Dipole}(\mathbf{x}) = \frac{m}{r^3}(y\hat{e}_x - x\hat{e}_y) \qquad (2.2)$$

where m is the dipole moment and $r^2 = x^2 + y^2 + z^2$. In the case of Earth, the z-axis is parallel but opposite to m and the dipole is at the center of the coordinate system.

$$m = -m\hat{e}_z = -31100 \; \hat{e}_z \; nT \; R_E^{\;3} \qquad (2.3)$$

The associated magnetic field is

$$\mathbf{B}_{Dipole}(\mathbf{x}) = \left(-\frac{3mxz}{r^5}\right)\hat{e}_x + \left(-\frac{3myz}{r^5}\right)\hat{e}_y + \left(-\frac{m(3z^2 - r^2)}{r^5}\right)\hat{e}_z. \qquad (2.4)$$

There is no net current contributed by the dipole; however the magnetic field components are essential to the matching of the kappa parameter in the region of interest.

The Ring Current Field

The westward traveling current encircling the Earth in the inner magnetosphere is called the ring current. This current is created by protons drifting westward and electrons drifting eastward. The ring current tends to decrease the strength of the Earth's dipole field at low altitude. The dipole nature of the Earth's magnetic field can confine particles over a wide range of energies. The Active Magnetospheric Particle Tracer Explorer/Charge Composition Explorer (AMPTE/CCE) mission of the mid 1980's was the first to measure the composition of the main part of the ring current.

A simple analytic form for the ring current is needed to couple the model dipole field to the model magnetotail field. The ring current of [*Tsyganenko and Usmanov*, 1982] was selected for this task. Tsyganenko and Usmanov base their ring current model on the experimentally deduced changes in the magnetic field of the inner magnetosphere done by *Sugiura* [1973]. They further assume that the ring current is localized near the equatorial plane [*Sugiura*, 1972]. This model of the ring current provides an adequate representation of the magnetic field and has been used in other studies [*Lui and Hamilton*, 1992]. The vector potential is the same as the pure dipole except for the addition of $4\rho_o^2$ in the denominator which eliminates the singularity at the origin.

$$\mathbf{A(x)} = \frac{-B_o}{(r^2 + 4\rho_o^2)^{3/2}}(y\hat{e}_x - x\hat{e}_y) \tag{2.5}$$

The B_o parameter is a negative number that scales the field depression near the Earth and ρ_o is the characteristic radius of the ring current. The magnetic field associated with the ring current is then

$$\mathbf{B}_{Ring}(\mathbf{x}) = \left(\frac{3B_o xz}{(r^2 + 4\rho_o^2)^{5/2}}\right)\hat{e}_x + \left(\frac{3B_o yz}{(r^2 + 4\rho_o^2)^{5/2}}\right)\hat{e}_y + \left(\frac{B_o(3z^2 - r^2 + 8\rho_o^2)}{(r^2 + 4\rho_o^2)^{5/2}}\right)\hat{e}_z \tag{2.6}$$

The components of the ring current are given by

$$\mathbf{J}_{Ring}(\mathbf{x}) = \frac{1}{\mu_o}\nabla\times\mathbf{B}_{Ring}(x) = \frac{1}{\mu_o}\left[\left(\frac{-60B_o\rho_o^2 y}{(r^2 + 4\rho_o^2)^{7/2}}\right)\hat{e}_x + \left(\frac{60B_o\rho_o^2 x}{(r^2 + 4\rho_o^2)^{7/2}}\right)\hat{e}_y\right]. \tag{2.7}$$

The current density profile for the ring current as well as the B_x and B_z magnetic field components for the noon-midnight plane on the nightside are shown in figure 2.2. The scale of the field depression near the Earth used throughout the study is $B_o = -30$ nT and the characteristic radius is $\rho_o = 10$ R_E. The ring current is useful for reducing the B_z component of the field near the Earth.
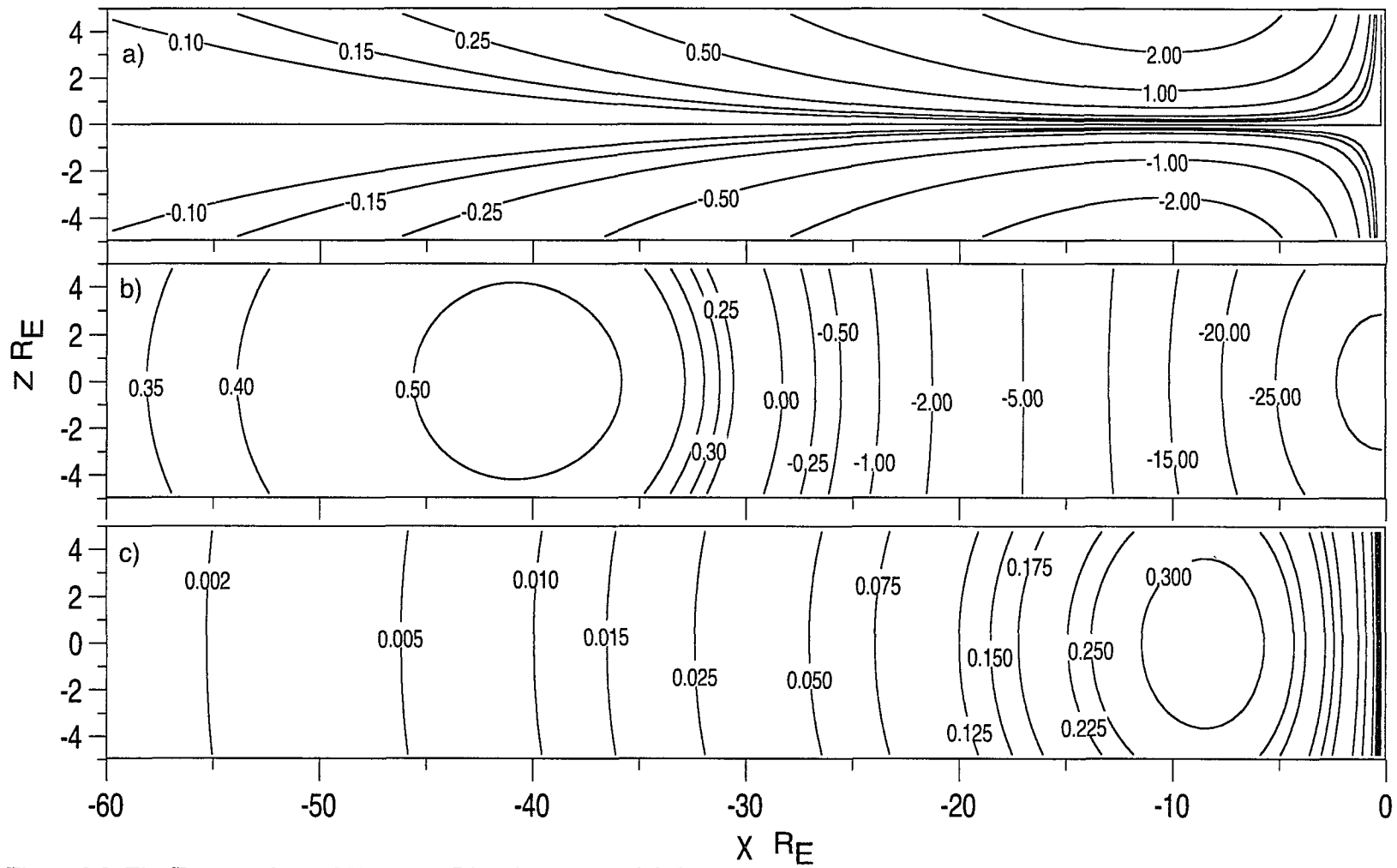
Figure 2.2: The Tsyganenko and Usmanov Ring Current Model, [1982]. B_o=-30, ρ =10 R_E ,a) B_x, (nT) b) B_z, (nT) c) j_y, (nA/m^2).

Without the ring current the location of the kappa minimum could not be adjusted to correspond to that of the Tsyganenko model.

The Equilibrium Tail Model

The magnetotail of the Earth is the result of the magnetized solar wind particles interacting with the geomagnetic field. The solar wind compresses the magnetosphere on the "upwind" or dayside and elongates on the magnetosphere "downwind" or nightside. The balance between the solar wind energy and the Earth's magnetic field determines the size of the magnetosphere. Embedded within the midplane of the magnetotail is the cross-tail current sheet. The cross-tail current sheet arises as a separator between the magnetic field of the northern lobe, which is directed towards the earth, and the field of the southern lobe, which is directed away from earth. The particles of the plasma sheet must satisfy Ampere's law as well as exert enough pressure to balance the magnetic field pressure of the lobes. Understanding how the particles of the plasma sheet accomplish this is complicated by the particles which do not obey the guiding center approximation.

A simple model of a plasma sheet formed at the interface of two regions of opposing magnetic field would be useful for studying the nonlinear dynamics of single particle orbits. In the midtail region a two-dimensional equilibrium tail field module would be convenient for studying the neutral sheet. The equilibrium models represent magnetic fields that are derivable with approximately isotropic particle distributions. The most widely used magnetotail models for such studies are variations on the exact solution to the Vlasov-Maxwell equations by *Harris* [1962]. The Harris study of plasma sheet equilibria in one dimensional magnetic fields is rooted in the earlier work of Walker. This can be extended to two dimensions.

The equilibrium distribution of a plasma was explored in a series of papers by *Walker* [1900, 1904, 1915]. In these papers Walker needed to solve a two dimensional Liouville equation of the form

$$\frac{\partial^2 A}{\partial x^2} + \frac{\partial^2 A}{\partial z^2} = A_c e^{-2A/A_c}.$$
(2.8)

In this work the solar magnetospheric coordinates are used instead of general cartesian coordinates. The general solution, attributed to *Pockels* [1891], is

$$A = -\frac{A_c}{2} \ln \left[4 \frac{\left(\left(\frac{\partial \phi}{\partial x} \right)^2 + \left(\frac{\partial \phi}{\partial z} \right)^2 \right)}{(1 + \phi^2 + \psi^2)^2} \right]$$
(2.9)

A more available derivation can be found in *Ames* [1967]. The functions $\phi(x, z)$ and $\psi(x, z)$ are the real and imaginary parts of an arbitrary analytic function

$$G(\zeta) = G(x + iz) = \phi(x, z) + i\psi(x, z)$$
(2.10)

An interesting family of generating functions start with the general form

$$G(\zeta) = e^{i\zeta} = \exp i(f_r(x, z) + if_i(x, z))$$
(2.11)

where a more general complex function $\zeta(x, z) = f_r(x, z) + if_i(x, z)$ is used. Further manipulation yields

$$G(\zeta) = \exp\{if_r(x, z) - f_i(x, z)\}$$
$$= \cos(f_r(x, z))e^{-f_i(x, z)} + i\sin(f_r(x, z))e^{-f_i(x, z)}$$
(2.12)

which results in the assignment of the general functions $\phi(x, z)$ and $\psi(x, z)$ to the first and second terms respectively. Taking the partial derivatives of $\phi(x, z)$ with respect to both x and z as well as the sum of the squares of $\phi(x, z)$ and $\psi(x, z)$ gives

$$\frac{\partial \phi(x, z)}{\partial x} = -e^{-f_i(x, z)}\left(\sin f_r \frac{\partial f_r}{\partial x} + \cos f_r \frac{\partial f_i}{\partial x}\right)$$

$$\frac{\partial \phi(x, z)}{\partial z} = -e^{-f_i(x, z)}\left(\sin f_r \frac{\partial f_r}{\partial z} + \cos f_r \frac{\partial f_i}{\partial z}\right)$$

(2.13)

$$1 + \phi^2(x, z) + \psi^2(x, z) = 1 + e^{-2f_i(x, z)}$$

(2.14)

Substituting into the general solution and simplifying yields

$$A(x, z) = A_c \ln\{\cosh(f_i(x, z))\} - \frac{A_c}{2}\ln\left[\left(\left(\frac{\partial f_r}{\partial x}\right)^2 + \left(\frac{\partial f_r}{\partial z}\right)^2\right)\sin^2 f_r \right.$$

$$\left. + \left(\left(\frac{\partial f_i}{\partial x}\right)^2 + \left(\frac{\partial f_i}{\partial z}\right)^2\right)\cos^2 f_r + 2\sin f_r \cos f_r \left(\frac{\partial f_r}{\partial x}\frac{\partial f_i}{\partial x} + \frac{\partial f_r}{\partial z}\frac{\partial f_i}{\partial z}\right)\right]$$

(2.15)

The specific case of $f_r(x, z) = ax$ and $f_i(x, z) = az$, where a is a constant, is the

Harris solution, $\mathbf{A} = (0, A_y(z), 0)$; $A_y(z) = A_c \ln(\cosh(az)) - A_c \ln a$. The magnetic

field for the Harris model is then

$$\mathbf{B}(z) = B_{xo}\tanh\left(\frac{z}{L}\right)\hat{e}_x,$$

(2.16)

where B_{xo} scales the asymptotic magnetic field, and L is a parameter controlling the half-

thickness of the central plasma sheet. When a weak uniform normal field, B_{zn}, is added to

the magnetic field, the new field is called the Modified Harris model. The associated cur-

rent is

$$\mathbf{J}_{Harris}(z) = \frac{-A_c}{\mu_o L^2}\operatorname{sech}^2\left(\frac{z}{L}\right)\hat{e}_y.$$

(2.17)

Two dimensional equilibrium models that try to represent the magnetotail have

been studied by [*Birn et al.*, 1975; *Birn*, 1977; *Lembege and Pellat*, 1982; and *Zwingmann*,

1983]. All of these models belong to a class of equilibrium solutions of the form

$$A_y(x, z) = A_c \ln \left[\frac{\cosh\left(\frac{z}{L}F(x)\right)}{(F(x))} \right], \tag{2.18}$$

where L is a plasma sheet thickness and $F(x)$ is an arbitrary function of x. The stability of

these self-consistent taillike equilibrium solutions is extensively discussed in *Kiessling and*

Schindler [1987]. In order to generate this solution and exactly satisfy the Cauchy-Riemann

conditions, the terms of the real and imaginary parts to the analytic generating function

$G(\zeta)$ would have to satisfy

$$f_r(x, z) = -\frac{z^2}{2L}\frac{\partial F(x)}{\partial x} + \frac{1}{L}\int F(x)dx$$

$$f_i(x, z) = \frac{z}{L}F(x) \tag{2.19}$$
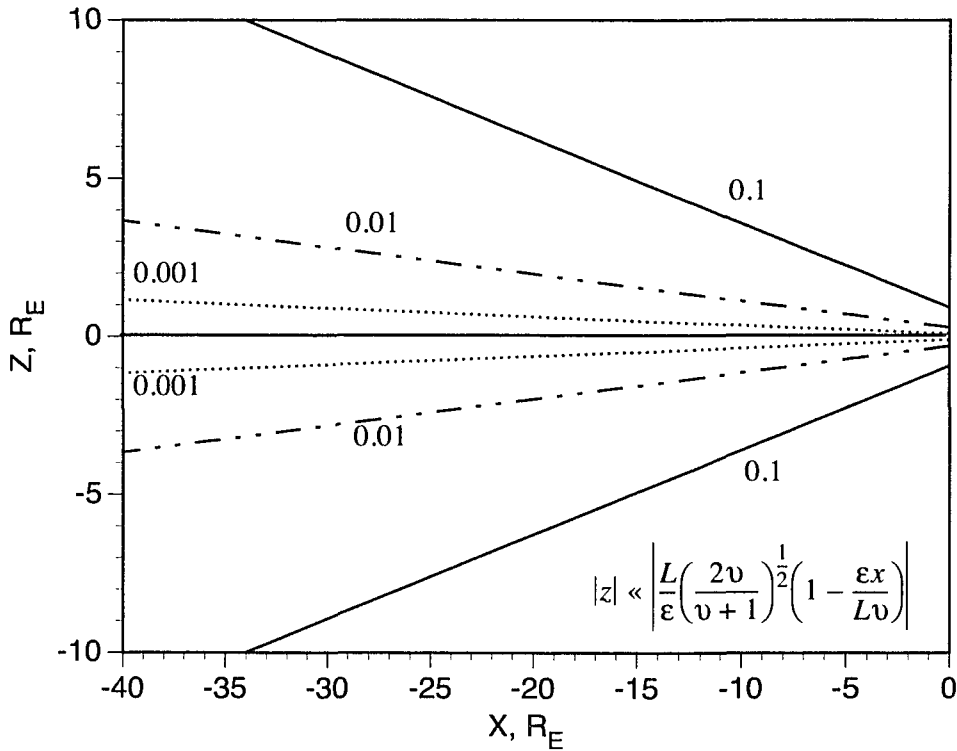
Figure 2.3: The relative error of higher order terms.

An exact solution is not known but a slowly varying function of x can achieve a result sufficiently accurate to model the magnetotail plasma sheet. In order to neglect higher order terms, the function $F(x)$ must meet the condition that $\dfrac{z^2}{2F(x)}\dfrac{\partial^2 F(x)}{\partial x^2} \ll 1$. The function which was found to best complement the dipole and ring current components of the new model was studied by *Zwingmann*, [1983]. This function is

$$F(x) = \left(1 - \frac{\varepsilon x}{L\upsilon}\right)^{-\upsilon} . \tag{2.20}$$

As can be seen in figure 2.3 the effect of the higher order terms for the Zwingmann function is less than one percent in the plasma sheet region.

The vector potential used for the equilibrium magnetotail is to second order

$$\mathbf{A}_{Tail} = (0, A_y(x, z), 0); \qquad A_y(x, z) = A_c \ln\left[\frac{\cosh\left(\frac{z}{L}F(x)\right)}{F(x)}\right] + O(\varepsilon^2) \tag{2.21}$$

and the associated magnetic field is

$$\mathbf{B}(x, z) = A_c F(x)\tanh\left(F(x)\frac{z}{L}\right)\hat{e}_x + \left(A_c\frac{\partial F(x)}{\partial x}\left[\frac{L}{F(x)} - z\tanh\left(F(x)\frac{z}{L}\right)\right] + B_{zn}\right)\hat{e}_z \tag{2.22}$$

where B_{zn} is a weak uniform normal field. The B_{zn} can be considered a simple adjustable northward IMF generated by infinite current sheets well outside the magnetosphere. The current for this case is

$$\mathbf{J}_{eq}(x, z) = \frac{-A_c}{\mu_o}\left\{\frac{F^2(x)}{L}\mathrm{sech}^2\left(F(x)\frac{z}{L}\right) - \frac{\partial^2 F(x)}{\partial x^2}\left[\frac{L}{F(x)} - z\tanh\left(F(x)\frac{z}{L}\right)\right]\right. \tag{2.23}$$
$$\left. + \left(\frac{\partial F(x)}{\partial x}\right)^2\left[\frac{L}{F^2(x)} + \frac{z^2}{L}\mathrm{sech}^2\left(F(x)\frac{z}{L}\right)\right]\right\}\hat{e}_y$$

The parameter values chosen for this study for the Zwingmann tail model are given in table 2.1 along with the values of the uniform normal field. The nomenclature of thin and thick

are with respect to what is referred to as the standard model. The distinction between the different current sheets can also be seen by looking at the relative thicknesses shown in figure 2.9.

Table 2.1: Zwingmann Model Parameters

Current Sheet Type	A_c	ε	L	n	B_{zn}
Thin	160	0.010	0.05	1.25	2.00
Standard	300	0.018	0.05	1.25	0.75
Thick	415	0.018	0.05	1.50	0.00

Tail Model Design Criteria

Ampere's law for steady conditions, $\nabla \times \mathbf{B} = \mu_o \mathbf{j}$, shows that selection of a magnetic field model for the magnetotail is equivalent to the selection of a model for $\mathbf{j}$ throughout the current sheet. For this reason, certain key features of the T89 model were relied upon to act as a proxy for the magnetotail while setting the parameters in the new model. These features include the individual magnetic field components, the current density j_y, the integrated sheet current K_y, and the kappa parameter.

Since B_z is critical to energization processes resulting from nonadiabatic particle effects, careful attention must be taken when choosing the magnitude of B_z in the magnetotail neutral sheet. Although the T89 model will be used as a guide, the question of how well it represents B_z at midnight in the neutral sheet is subject to what data were used in determination of the model parameters. In a study by *Fairfield* [1986], IMP 6, 7, and 8 data were selected for substorm-free periods where the spacecraft were within ± 3 R_E of the es-

timated location of the neutral sheet. Fairfield found that the average B_z was between 2 and

3 nT for the $-20 < x < -10$ R_E range and less than 2 nT on average for $x < -20$ R_E. These

results agree with the *Sergeev et al.* [1993] study that looked at only a single day of ISEE

data. These ISEE results are contradicted by a more extensive study using the ISEE dataset

[*Huang and Frank*, 1994]. Huang and Frank find the average B_z in the magnetotail neutral

sheet to vary from 5 to 8 nT in the range $-22 < x < -10$ R_E and $-10 < y < 10$ R_E. Another

study performed by *Rostoker and Skone* [1993] fit a combined ISEE and IMP 8 dataset

where ISEE was used for the $-22 < x < -10$ R_E range and IMP 8 for the $-38 < x < -22$ R_E

region. Their results reflect the choice of satellite to represent each range. Near the Earth

they have the higher B_z values of the ISEE dataset and down tail the lower IMP 8 values

dominate their functional fit. The seemingly contradictory results could reflect differences

in magnetometer design or possibly differences in the solar wind and interplanetary mag-

netic field (IMF) during the different periods of satellite operation. Because of the contro-

versy surrounding measurements of B_z, the new model allows for an additional constant

B_z. In this study B_z is higher than Fairfield's values but lower than the Huang and Frank

values.

The magnetic field lines for the T89 model and the three versions of the new model

are shown in figure 2.4. The top panel shows the T89 model for $Kp = 4$ with no dipole tilt.

This moderately disturbed version of the model has much more flaring in the region $|z| > 2$
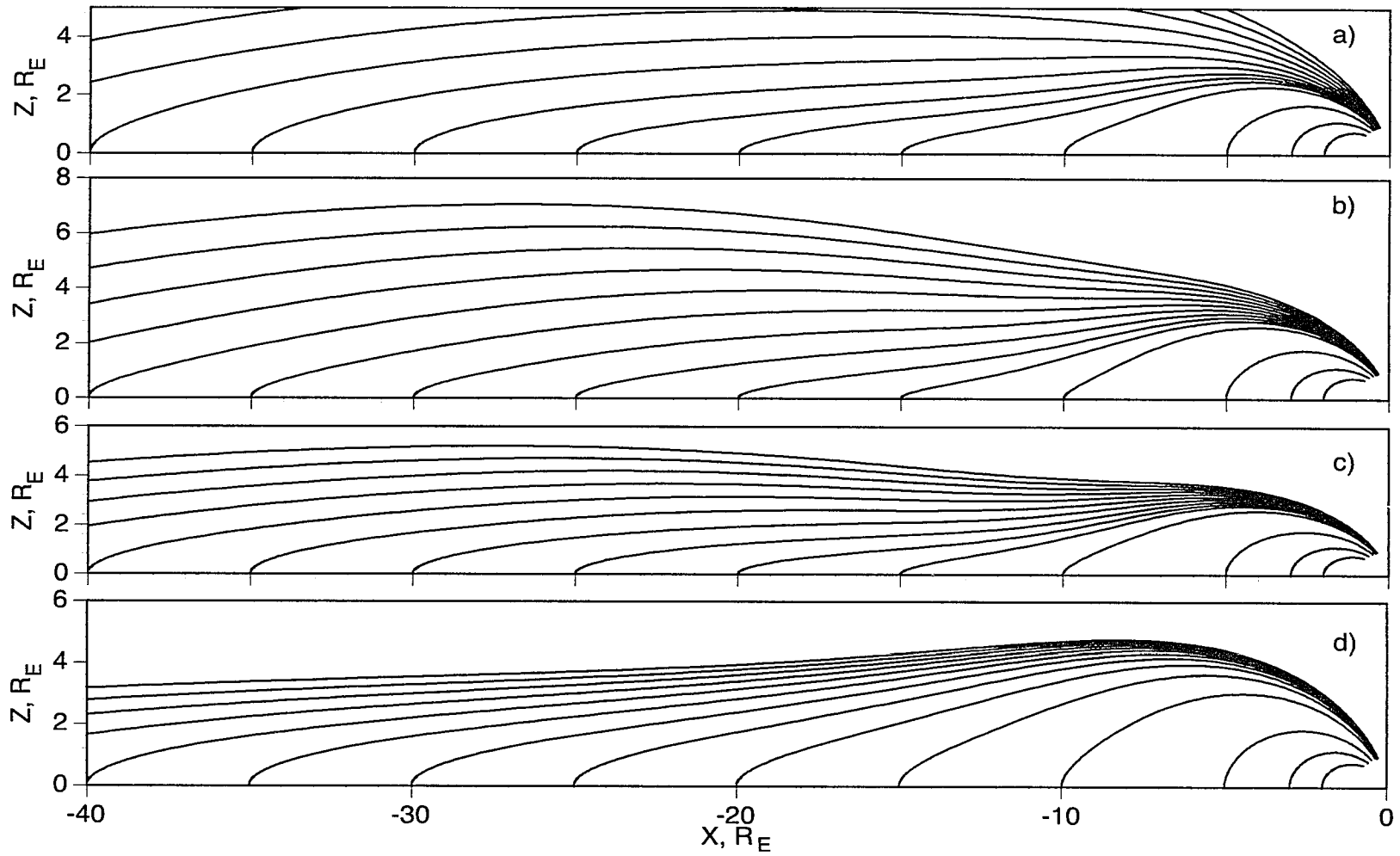
Figure 2.4: Comparison of the model fields to the empirical T89 model, a) Tsyganenko Model for Kp=4, b) Thin Model, c) Standard Model, d) Thick model
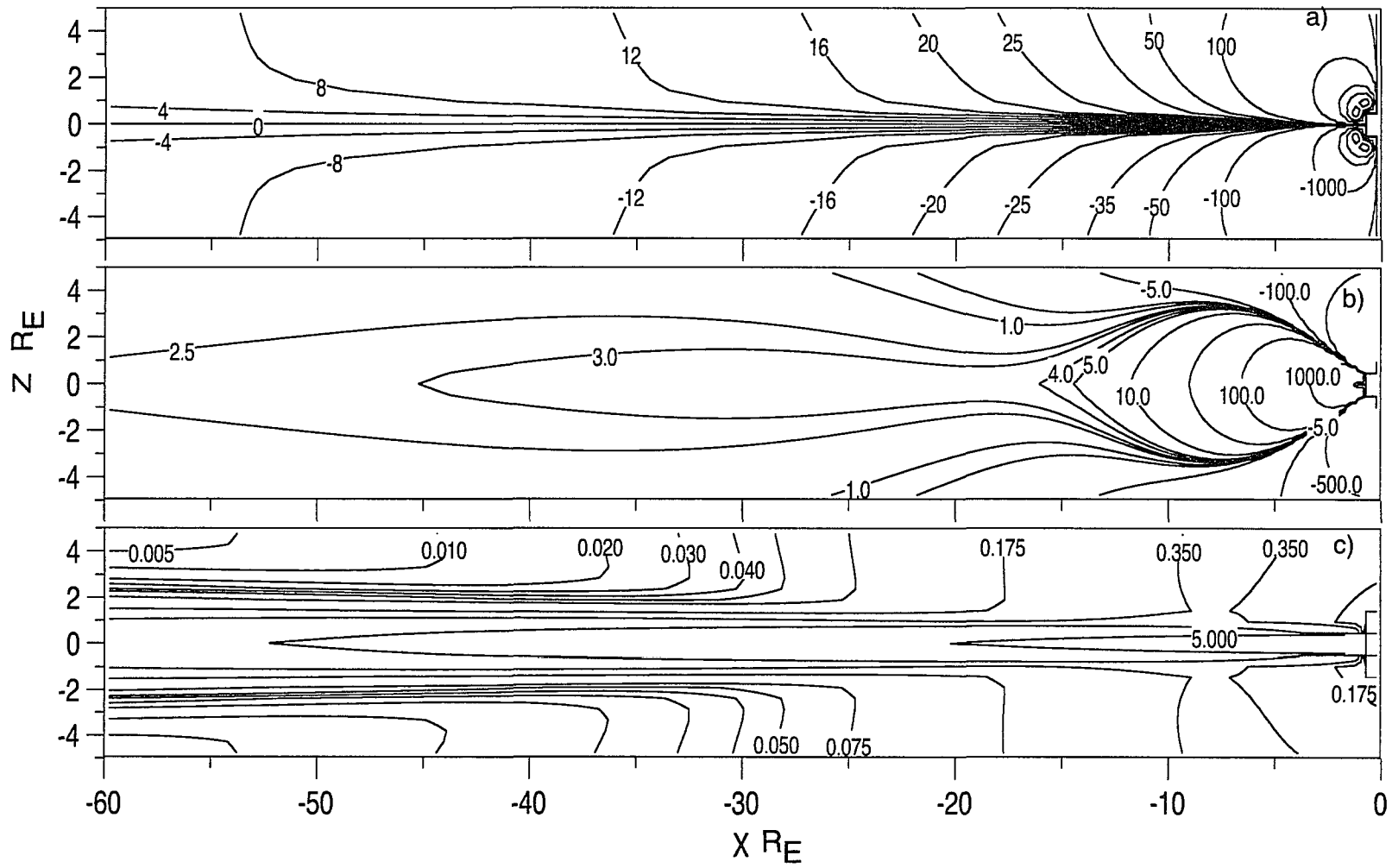
Figure 2.5: Thin Model $A_c = 160$, $\varepsilon = 0.010$, $L = 0.05$, $\nu = 1.25$, $B_{zn} = 2.0$, a) B_x, (nT) b) B_z, (nT) c) j_y, (nA/m^2).
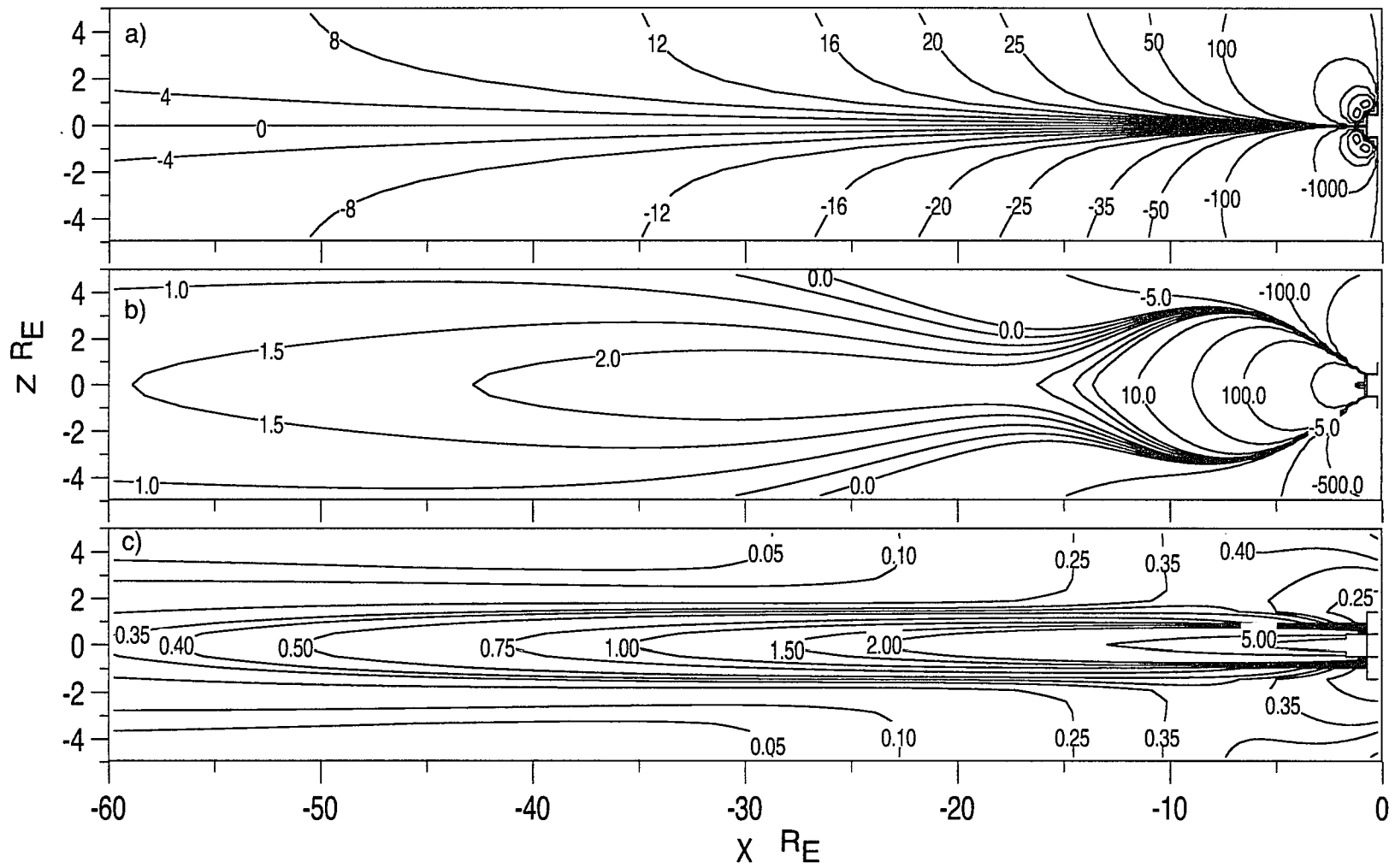
Figure 2.6: Standard Model $A_c = 300$, $\varepsilon = 0.018$ $L = 0.05$, $\nu = 1.25$, $B_{zn} = 0.75$ a) B_x, (nT) b) B_z, (nT) c) j_y, (nA/m^2).
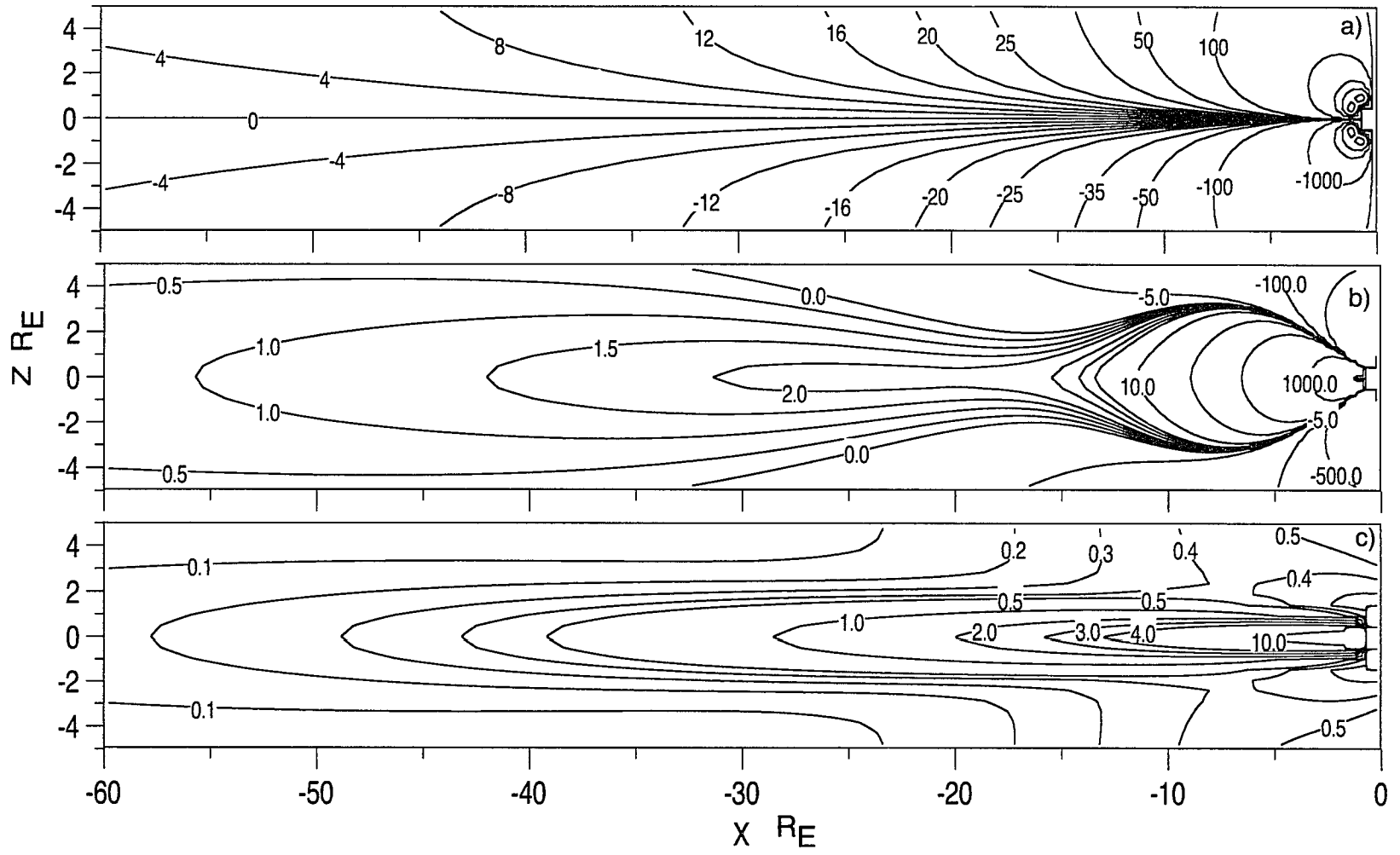
Figure 2.7: Thick Model $A_c = 415$, $\varepsilon = 0.018$, $L = 0.05$, $\nu = 1.5$, $B_{zn}=0.0$, a) B_x, (nT) b) B_z, (nT) c) j_y, (nA/m^2).

than the standard (Figure 2.4c) or thick (Figure 2.4d) models, but is similar to the thin

model (Figure 2.4b) for this region. In the current sheet region, $|z| < 2$, the thin and

standard model field lines most closely resemble the T89. However, beyond $x < -25$ R_E,

all three models begin to match the T89 in this region.
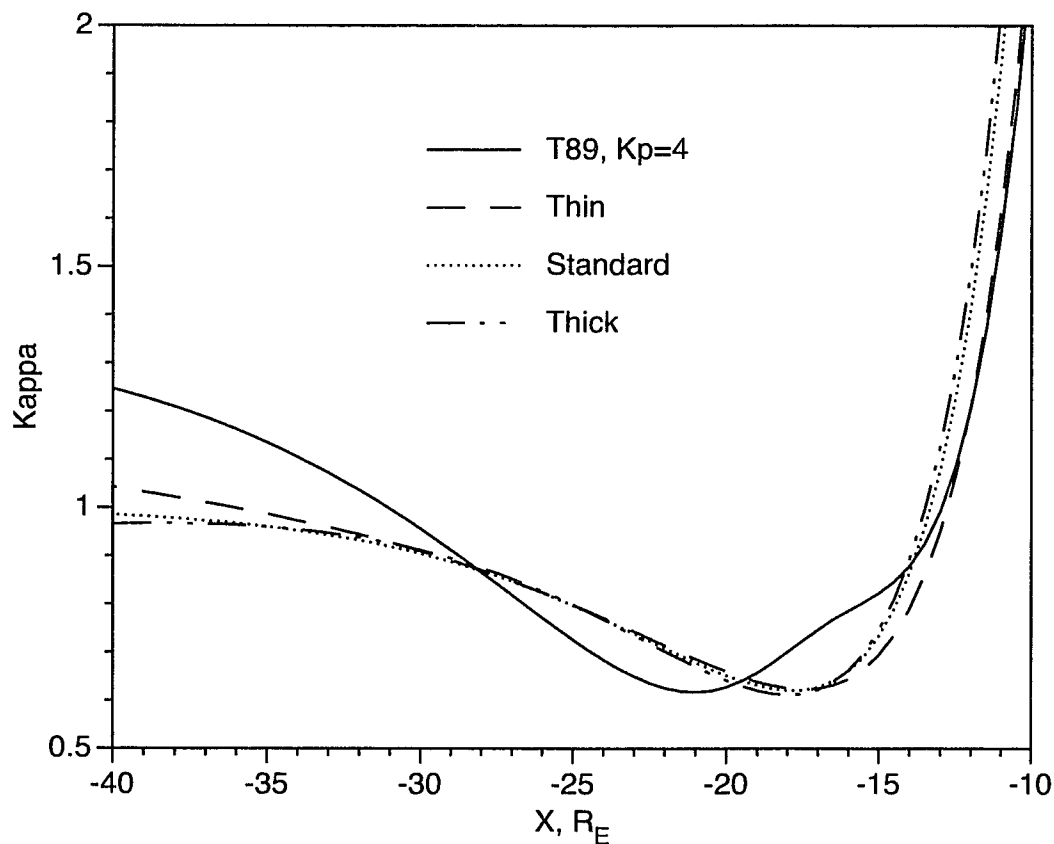
Figure 2.8: Kappa parameter $\kappa= \sqrt{R_c/\rho}$, where R_c is the magnetic field line radius of curvature and ρ is the particle gyroradius radius at $z = 0$ for a 1 keV proton.

The B_x, B_z, and j_y field components for the T89, thin standard, and thick models

are shown in figures 2.5-2.7. The top panel of each figure is the B_x component of the mod-

el. Within the midtail region, $-20 < x < -10$ R_E, this component closely resembles the

T89. The middle panel, for all four sets of figures, is the B_z component. Within

$x > -15$ R_E the new models and the T89 agree mostly due to the dominance of the dipole field. Beyond $x < -15$ R_E the T89 has a shape comparable to a drop of water just after dripping from a faucet. The new model does not have the low B_z separation zone of $-25 < x < -15$ R_E, but does have a moderate wineglass stem shape of similar magnitude to the T89 beyond $x < -25$ R_E.
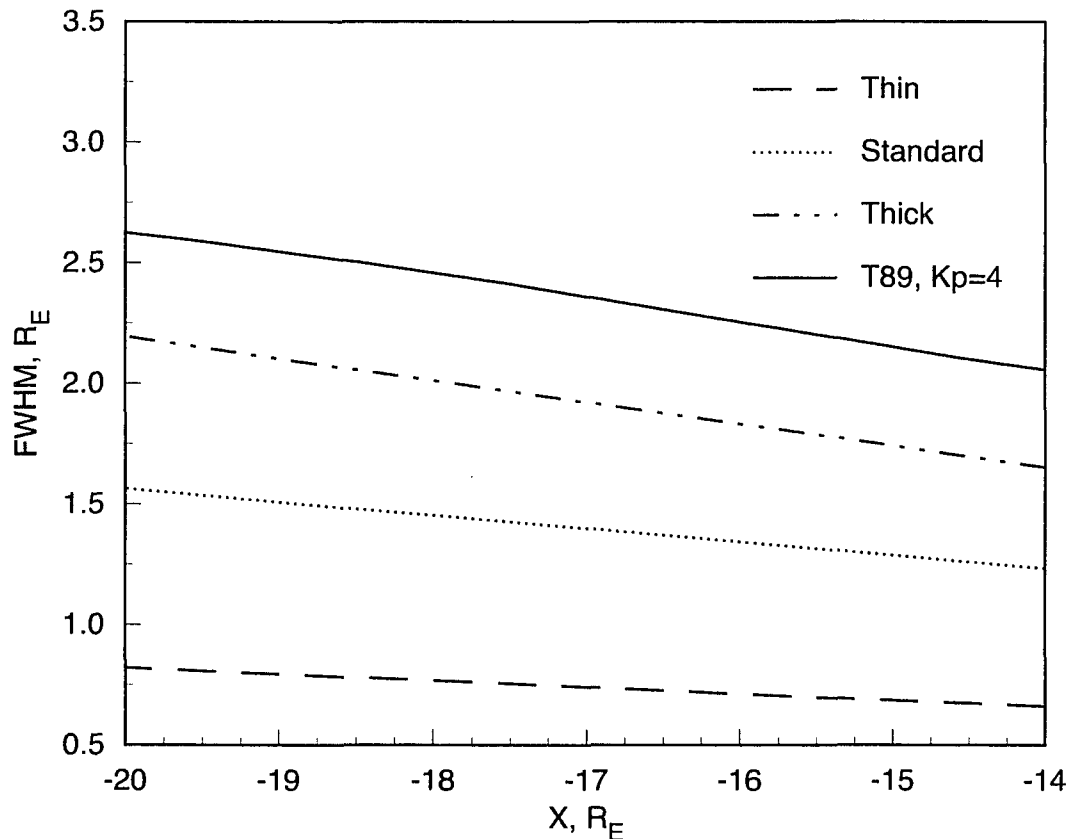
Figure 2.9: The Full Width at Half Maximum (FWHM) of j_y for each current sheet.

The B_z is key to the adjustment of the magnitude of kappa. In order to match the kappa profile of the T89 model seen in figure 2.8, an additional B_{zn} was added to both the thin and the standard models. This is because kappa is proportional to the radius of curvature of the magnetic field lines (see Equation (1.6)). These values are given in Table 2.1. The thick model did not require any additional B_{zn}.

Any empirical magnetotail model tends to have a thicker current sheet than is present in the actual magnetotail. This is because the actual magnetotail moves up and down in the z direction. Tail flapping broadens the apparent observed thickness obtained by averaging or binning satellite data. *McComas et al.*, [1986] and *Sanny et al.*, [1994], using the ISEE 1 and 2 satellite pair, concluded that the instantaneous scale size of the principal current sheet is on the order of 1 R_E. Because of these observations, we generated versions of the tail with current sheets that are thinner than the one in T89. We also selected the Kp = 4 version of T89 to model quiet time current sheets because this version is thinner and has a larger equatorial B_z than the quiet time versions of T89.

The relative thicknesses between the different current sheets can be seen in figure 2.9. The full width at half maximum (FWHM) of j_y for the T89 sheet is a factor of 3.1 greater than the thin sheet. The thick sheet is 2.5 times greater than the thin sheet and the standard sheet is about 1.9 times as great as the thin current sheet. These features show that the model current sheets are more well defined than the selected Tsyganenko model. Although the model current sheets we have developed drop off more rapidly than the T89 model, the integrated cross tail current is still able to match that of the T89 in the midtail region.

The A_c parameter scales the magnetic field, and consequently the current density j_y. The total cross sheet current density, K_y, given in figure 2.10, is also adjusted by A_c. It is calculated by integrating $j_y(x, y, z)$ through the plasma sheet from $-2R_E$ to $2R_E$, or in the case of the T89 model, $\pm 2D(x, y)$. Using the T89 K_y as a guide, the A_c parameter for each of the three models was set to best match in the midtail $-20 < x < -14$ R_E region. The K_x and K_y cross sheet current densities for the $Kp = 5$ T89 model in the equatorial

plane, for $0 < y < 20$ R_E and $-70 < x < 10$ R_E are presented in *Kaufmann et al.* [1993b].

The K_y of the new models reasonably matches the T89 model for the range $x < -5$ R_E and $|y| < 10$ R_E. The new model K_x are the same shape but an order of magnitude lower than the comparable T89 K_x for all three parameter sets and for the same range as the K_y values. Outside of this range the new model and T89 significantly diverge. This is understandable since the magnetotail component of the model is two-dimensional.
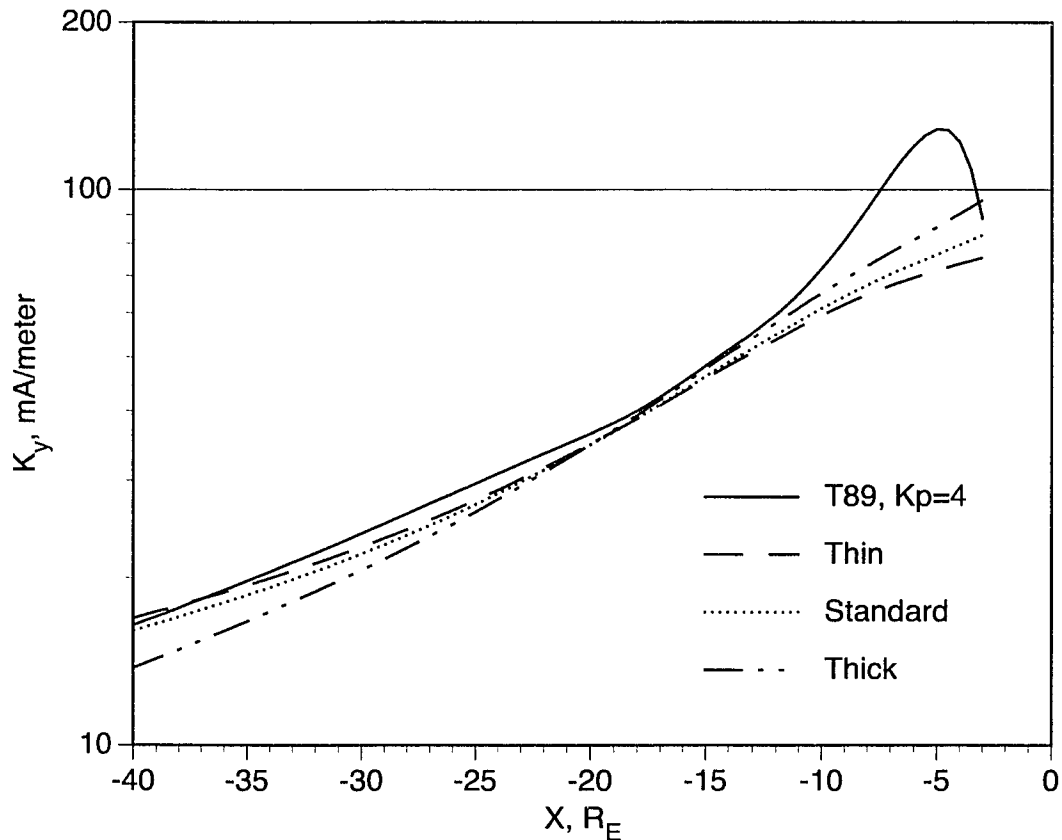
Figure 2.10: The total cross-tail current sheet density. These are found by integrating $j_y(\mathbf{x})$ between $z_{sm} = \pm 2D(x, y)$ in the T89 model and $z_{sm} = \pm 2$ R_E for the new model.

The integrated cross tail current is an important criteria for fixing the model parameters. This is because K_y was found to be nearly independent of y [*Kaufmann et al.*, 1993b].

The implication of this is that $j_y E_y$, the energization rate, varies across the width of the

magnetotail in the same way that E_y varies. *Kaufmann et al.* [1993b] mapped the *Heppner and Maynard* [1987] or HM87 electric field model, which was based on an average Kp of three, from the ionosphere to the equatorial plane using the T89 model. This study found that using 50 R_E as the distance between dawn and dusk flanks yields an average E_y that varies from 0.06 mV/m when $Kp = 0$ to 0.3 mV/m when $Kp = 5$. A confirmation of this result using the $Kp = 4$ model has been performed by *Maynard et al.* [1995]. The cross tail field used for all the particle tracing done in this study is set at the higher

$E_y = 0.3$ mV/m value.

The inclusion of the dipole was essential to creating realistic field lines. Unlike one-dimensional models used for particle studies, the particles are now free to mirror. This eliminates the need to distinguish between trapped and untrapped particles as was done with the Modified Harris model used by *Lu* [1993]. The ring current lowers B_z within $x > -10$ R_E which improves the K_y and the Kappa in this range. However, as can be seen in figures 2.8 and 2.10, the model is not reliable enough for particle studies of the inner edge to the current sheet.

The magnetotail model generated for this particle study fulfills the objective of providing a reasonable proxy for the more complicated T89 model. The magnetic field components, kappa, and the currents have been plotted for three sheets of differing thicknesses. The kappa profiles, which determine the orbit regimes that particles will follow are all similar to that of the T89. The cross sheet current K_y is similar to the T89 model for all three versions of the model, and the magnetic fields do not exhibit any unwanted features in the current sheet region that would cast doubt on our results.

Chapter III

SOFTWARE

3.1 Introduction

Computer software is the implementation of abstract ideas expressed as an ordered collection of simple mathematical and logical computer operations that must be sequentially executed. Physicists express their ideas with the symbolic language of math. When an analytic expression cannot be achieved, the gap between the symbolic representation of physical laws and computer language is bridged by the techniques of numerical methods. There are many books devoted to the details of carrying out numerical integration, differentiation, matrix inversion, etc. Some of these are [*Hildebrand*, 1962; *Ames*, 1977; *Koonin and Meredith*, 1990; and *Press et al.*, 1993].

The software design for this study of current sheet formation depends heavily on the algorithms chosen for solving systems of differential equations, differentiation, curve fitting, matrix operations, and other mathematical operations. However, the programs developed for this project also have to handle large amounts of output. This presents a set of problems primarily associated with the work of computer scientists such as graphical presentation (scientific visualization) and the management of large and numerous output files.

In order for the programs to be easily understood and maintained, as well as developed and debugged, a significant amount of time and thought must be applied to the computer science as well as the physics of the problem. The two primary constraints, fast and

41

relatively compact code that can run acceptably on a computer of workstation performance, had to be met in order to fulfill the science objective.

The goal of this project was to determine the types of ion orbits that are necessary to sustain the cross-tail current distribution of a preselected magnetic field. As discussed in Chapter 1, particles undergo chaotic motion in the neutral sheet as well as gyrotropic motion. Because of the chaotic nature of the particle orbits in the region of interest, a fully evolving MHD or Hybrid code will not be able to extract the kinetic processes relevant to sustaining a cross tail current. This is actually beneficial from a hardware standpoint since MHD codes still require supercomputers [*Tajima*, 1989]. This project has been implemented entirely on desktop workstations (e.g., an RS/6000 Model 320 and Silicon Graphics Indigo^2).

This chapter outlines the design choices that were made in developing the software that implements the Self Consistent Orbit Tracing (SCOT) technique. Details of the physics abstraction necessary to implement data structures, subroutine hierarchies, and other details will be presented.

3.2 Software design criteria

The study of plasma physics can be distilled down to looking at the collective behavior of a system of charged particles in an electromagnetic environment. The particle system is the collection of all particles evolving over time according to the same boundary conditions and laws of motion. The attributes of the individual particles, such as velocity, can change over time as a direct result of particle-particle interactions and particle-field interactions. In the case of the collisionless plasma of the Earth's magnetotail, where interactions between particles can be ignored, the number density is of the order of 10^6 m^{-3} with

a spatial range over tens of Earth radii. The number of particles that comprise this plasma would be staggering and unrealizable on a computer if it were required to follow each particle individually.

The limited number of particles that a computer can follow for a given time must accurately reflect the physical phenomena being explored. The orbit tracing method is one way to accomplish this and it is the basis of the technique used in this thesis. The idea of tracing individual orbits is based on the assumption that a small collection of particles can be found that will model the statistical behavior of a significantly larger ensemble. In order to design software centered on this idea we will first look at an abstraction of the data structures necessary rather than commit to a detailed description of the implementation. Fundamental to the abstraction is how particles are defined.

A particle is an object that occupies a point in space at a given instant of time. Particles evolve through time by acting and reacting to the properties of the environment within which they exist and based on their own specific characteristics. A particle cannot express multiple attributes of a given characteristic at one time. A particle may interact and alter attributes of other particles but it cannot occupy the same space at the same time. The state of a particle is the expression of it's attributes at a given moment.

This open definition of a particle can be applied to a broad range of particle types. A particle type further defines the parameters of a particle's existence. For example, a biologist seeking to model the interplay between organisms in an ecosystem might consider the individual organisms as particles and their type as the species to which they belong. Additional subclasses to the type of species could include gender, age, and size. The state of an individual organism is given by it's position, health, age, and other attributes. The state

of an organism can change according to factors in the environment such as food availability and predators as well as individual attributes such as health and age. To a software engineer seeking to implement the SCOT method or any other particle type code, the definition of "particle" is at the core of implementing the software objects and data structures.Thus the standard definition of a particle for a physicist can have different meanings to workers in other disciplines who wish to follow the SCOT paradigm.

Plasma properties	Velocity moments of a distribution function. Plasma properties such as number density, current density, pressure, temperature, bulk velocity, and heat flux can all be calculated from moments.		
Distribution function	An ensemble of trajectories binned over position and velocity $f(\mathbf{x}, \mathbf{v})$. A single Group or multiple Groups selected for certain characteristics are used to generate a distribution function.		
Library of Groups	A collection of Groups used to form the distribution function.		
Group	An ensemble of trajectories with similar initial parameters. (i.e. energy, pitch and phase angles, position, etc.)		
Trajectory	A time ordered set of position and velocity evolved according to its laws of motion. In the case of charged particles, the electric and magnetic fields are needed by the Lorentz force law.		
Particle	Type	Uncharged	neutrals
		Charged	electrons
			Ions : Species
	State	Position, velocity, energy, elapsed time.	
	Static Attributes	Mass (nonrelativistic), charge.	

Figure 3.1: Data hierarchy for the orbit tracing methodology

The type of particles making up the current sheet of the Earth's magnetotail are charged particles. This type of particle can be further broken down into additional subclasses such as electrons and ions. The ions can be differentiated further by their species. The charged particle class also has attributes such as mass, charge, and energy associated with each member of the class. The state of any member of the charged particle class is defined by the position, velocity, energy, and time. In order to change the state of a particle, the time attribute must be incremented and the position and velocity advanced according to the laws of motion governing charged particles.

In the case of charged particles, the Lorentz force law governs the motion of test charges in the presence of electric and magnetic fields. As a consequence, the attributes of position, velocity, and energy can be altered. The fields in the equation of motion can also be broken down into subclasses associated with the specific field models to be used. The model types are discussed in detail in Chapter Two.

The set of time ordered states associated with an individual particle is a trajectory. Many different trajectories of the same species may be combined into distribution functions. These individual distribution functions can be further combined to form the distribution function describing the system as a whole. The physical effects of the ensemble of all the trajectories acting in concert, such as number density, mass density, charge density, bulk velocity, current density, and pressure tensors, can be calculated from moments of the combined distribution function.

The environment within which particles interact encompasses many subclasses which can inherit attributes that overlap with other subclasses. This is not necessarily a direct feedback mechanism but more of a global knowledge of common attributes. The envi-

ronment superclass has two major subclasses, one which details the physical properties of the environment and another subclass that handles the computational model.

Examples of physical environments to which a charged particle could belong include vacuum tubes, semiconductors, stars, and the magnetotail of the Earth. Each of these examples has some boundary. Within the boundary, the density of matter, field strength variations, possibility of interparticle interactions, all must be accounted for when modeling the physical processes the particles undergo. In the specific case of current carriers in the Earth's magnetotail, particles are not allowed beyond the virtual confines of a region of space near the Earth; $-60 < x < -1$ R_E, $|y| < 25$ R_E, and $|z| < 5$ R_E. Particle tracing terminates when a trajectory exceeds these limits, these particles are considered complete and are designated as being *untrapped*. The electromagnetic variations are given by the field model discussed previously in chapter two. Unlike magnetohydrodynamics, it is assumed that there are no interparticle interactions so that the plasma is collisionless.

The computational model must attempt to reflect the reality of the physical world with a virtual world shaped by software and constrained by hardware. It is at this level where machine speed, memory, storage, and graphics, directly limit the scope of any model. The fundamental constraint of all particle approaches is the number of particles that can reasonably be handled with the available hardware. As an example from biology, the number of individual locusts of an actual hoard ravaging some geographic region could number in the hundreds of millions; a computer could not model that many individual locusts due to hardware limitations on memory and storage. This same problem occurs with particle models of magnetotail plasmas since the actual particle density can be very high. In the central plasma sheet where particle densities as high as $0.3 - 0.4$ cm^{-3} have been observed

[*Frank et al.*, 1984; *Baumjohann et al.*, 1989], this would mean about 8×10^{25} particles in a 1 R_E^3 volume. This is an overlap between the physical and computational classes over the attribute of particle number. The amount of memory needed to store the attributes of an individual particle and the superclasses to which it belongs on the target machine determine the limit on how many particles may be followed. This number will be many orders of magnitude less than what occurs naturally.

It was found that an individual group of particles can be adequately characterized by as few as 1000 particles. This was determined by the rather unsophisticated method of tracing groups of particles in ever larger sizes until the plasma characteristics no longer changed significantly. A single 1000 particle group can typically take twenty four hours on a dedicated IBM/RS6000 Model 320, or five hours on a newer Silicon Graphics Indigo[2]. The number of groups that are necessary to complete an example current sheet can be as high as twenty groups. So the total running time with all postprocessing and analyses can be on the order of a month.

3.3 Numerical Experiment Software Framework

The technique of using individual particle orbits traced in a fixed magnetic field model to study the plasma sheet is useful for understanding the contribution of different types of particle orbits to the overall current density. When groups of particles with similar orbital characteristics are combined they have a corresponding current density. These groups can themselves be combined to form an ensemble current density distribution. Since we are assuming a fixed magnetic field $\mathbf{B(x)}$ and neglecting the displacement current, we can use Ampere's law, $\mathbf{j(x)} = (1/\mu_o)\nabla\times\mathbf{B(x)}$, to specify the desired current density of the model current sheet.

Initialization

	Select **E** and **B** field models; Setup spatial grid; Determine particle cutoff conditions; Select particle species and injection method; Select data products to calculate and save;

Main Loop

Do until the number of orbits desired is exhausted

Setup the particle's starting attributes and reset all flags
Generate the orbit using a Lorentz force integrator
Do While(finish=FALSE)

    Integrate **F(r,t)** once with respect to time;
    If (simulation grid line(s) traversed)
        Integrate **F(r,t)** with respect to the coordinate of the
        plane just crossed by backtracking from the current-
        position to the plane;
        Update (**r,v,t**) array with the edge crossing position;
    end if

    Update (**r,v,t**) array with the new position;
    if (The trajectory completion criteria are satisfied)
        finish=TRUE;
    if ((The buffer is full) OR (finish=TRUE))
        Update the distribution function;

end do
Update the initial/final data file;
Update any of the selected data products which rely upon an
    individual particle orbit;

end do

Wrap up

	Calculate plasma parameters from the distribution function f(x,v); Write all data products selected to disk;

Figure 3.2: Main Program Overview

The first step in creating an ensemble of particles capable of forming the goal current density is to trace groups of ions in the specified electromagnetic field and generate the associated distribution functions. These steps are carried out in software by the program *partrj.f*. An overview of this program is given as Figure 3.2. A summary of the different

data files that *partrj* can produce is given in Appendix A. The subroutines that are used as building blocks for this program and other support codes are given in Appendix F.

The effect that the chosen model $\mathbf{B(x)}$ has on particles of different species, energy, injection location, and initial pitch angle must be studied. This process provides the physical understanding necessary to categorize particle orbits into families of like properties. A code capable of moving charged particles in prescribed electric and magnetic fields is needed. The program [*partrj.f*] was developed to trace M groups of particles

$$G_M(\mathbf{x}, v, t) = \{ O_i(x,y,z,v_x,v_y,v_z,t); i = 1...N \} , \tag{3.1}$$

where $O(x,y,z,v_x,v_y,v_z,t)$ represents an entire particle orbit and N is the number of particles. The individual orbits are used to calculate the ion current within each grid box. The following table states the global parameters used by the tracing program for this study.

Particle trajectory cutoff ranges	$-60 < x < 10, R_E$ $-25 < y < 25, R_E$ $-4 < z < 4, R_E$ $1.1 < r < 100, R_E$
Particle trajectory gridding ranges	$-20 < x < -14, R_E$ $-25 < y < 25, R_E$ $-2 < z < 2, R_E$
Number of Boxes	Xboxes = 6; Yboxes= 1 Zboxes = 40
Maximum allowed particle tracing time	15000 seconds
Particle species	protons
Number of particles	1000 per group
Figure 3.3: Global program parameters	

Although the program is capable of following particle species such as e^-, H^+, He^+, He^{++}, and O^+, we follow protons since they are the dominant current carriers in the magnetotail. In addition, for this study, the temperature of injected ions is isotropic, $T_{\parallel} = T_{\perp}$, and the ion pitch and phase angles are isotropic.

3.4 Lorentz force integrator

The equation of motion for a particle of mass m is described by Newton's law as

$$\frac{d\mathbf{p}}{dt} = \mathbf{F} \tag{3.2}$$

where $\mathbf{F}$ is the force which acts on the particle to change its momentum $\mathbf{p}$. The force which a particle of charge q experiences in a given electric field $\mathbf{E}(\mathbf{x}, t)$ and magnetic field $\mathbf{B}(\mathbf{x}, t)$ is described by the Lorentz force

$$\mathbf{F} = q[\mathbf{E}(\mathbf{x}, t) + \mathbf{v} \times \mathbf{B}(\mathbf{x}, t)] . \tag{3.3}$$

Substituting the Lorentz force into Newton's law then gives the equation of motion for a nonrelativistic charged particle in an electromagnetic field

$$\frac{d\mathbf{p}}{dt} = q[\mathbf{E}(\mathbf{x}, t) + \mathbf{v} \times \mathbf{B}(\mathbf{x}, t)] . \tag{3.4}$$

The linear momentum $\mathbf{p}$ can be eliminated from this equation by substituting $\mathbf{p} = m\mathbf{v}$. The resulting pair of coupled first-order ordinary differential equations is

$$\begin{aligned}
\frac{d\mathbf{v}}{dt} &= \frac{q}{m}[\mathbf{E}(\mathbf{x}, t) + \mathbf{v} \times \mathbf{B}(\mathbf{x}, t)] \\
\frac{d\mathbf{x}}{dt} &= \mathbf{v}
\end{aligned} \tag{3.5}$$

This first-order representation can then be numerically integrated both forward and backward in time to get a particle's trajectory for specified initial conditions. The implementation allows for the use of either the fourth-order Runge-Kutta method or the Bulirsch-

51

Stoer method which incorporates rational function extrapolation [*Press et al.,* 1993]. The

general program flow is illustrated in Figure 3.4.Unless otherwise stated, all of the particle

trajectories calculated for this study use the Bulirsch-Stoer method.

Lorentz Force IntegrationCycle

Cut timestep down
to avoid special
conditions

True

Integrate in time
(forward tracing)

Special Conditions
(multivalue function etc.) / False

Integrate with respect
to position
(backtracking)

Yes

Calculate the grid
location of the particle

Has the particle entered
a new grid box ?

No

Save (r,v,t) data
Flush buffer if needed
Check for completion
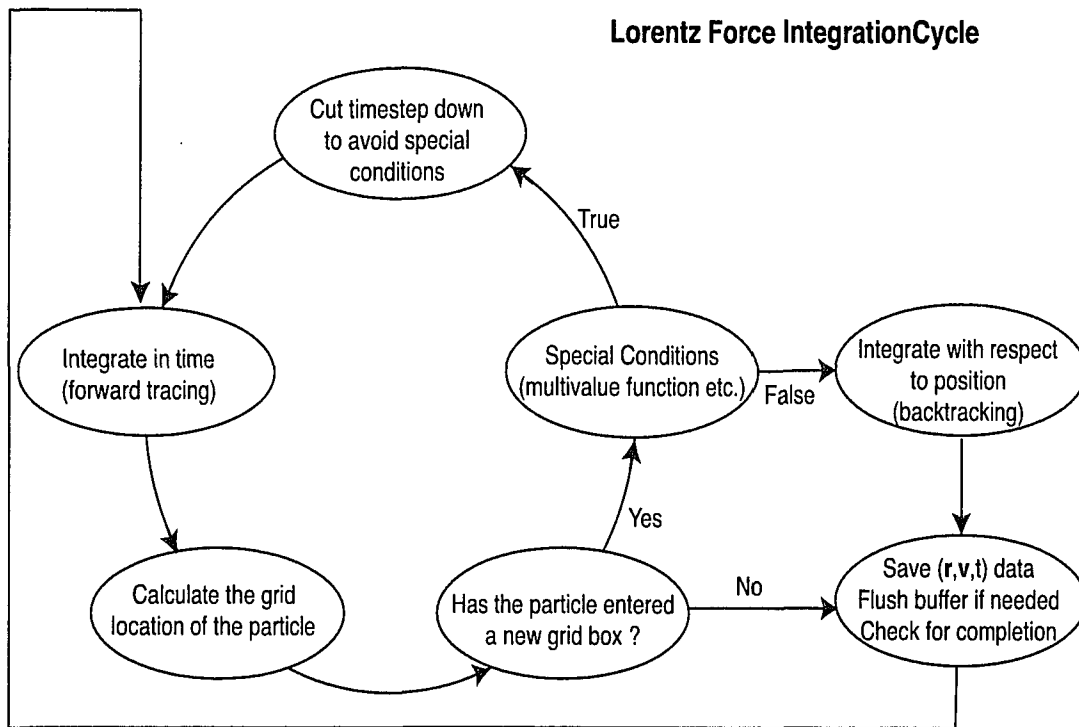
Figure 3.4: Lorentz Force Integration Cycle for a spatially gridded simulation volume.

Concurrent with the integration process, the spatial box numbers are calculated

from the position and saved to an array. These box numbers help determine when a box

edge has been crossed. In addition, the position, velocity, and elapsed time of each step are

saved to a buffer. When the buffer is exhausted, the program suspends integration in order

to process the trajectory segment. This entails computing velocity bin numbers for each in-

tegration step. Then, with the aid of the previously computed box numbers, binning half of

the timestep in the current phase space location of the distribution function $f(\mathbf{x}, \mathbf{v})$ and

the other half in the current position but previous velocity bins. This technique smoothes

gyrovelocity effects. At the completion of the buffer flushing; the last position, velocity, elapsed time, and velocity bin numbers are saved for use by the first point of the next buffer. The pointers into the buffer arrays are then reset and orbit tracing resumes.

Integrating the distribution function $f(\mathbf{x}, \mathbf{v})$ over various velocity moments to get plasma parameters is elegant but consequently requires more elaborate software. If the number and current densities within a box are all that is desired, it is not necessary to calculate the distribution function. By keeping track of the total time spent and the total distance traveled by a particle in the x, y, and z directions within the box, it can be shown that density is proportional to this total time and $\mathbf{j}_i(\mathbf{x})$ is proportional to distance. This method is described by *Eastwood* [1972] and *Kaufmann and Lu* [1993]. The previous study by *Lu* [1993] computed these parameters with

$$\mathbf{j}(\mathbf{x}_k) = \frac{n_o v_o q \Delta \mathbf{x}_k}{\Delta z}$$

$$n(\mathbf{x}_k) = \frac{n_o v_o \Delta t_k}{\Delta z}$$

(3.6)

where Δz is the height of each box, q is the charge, n_o is a density normalization factor based on an assumed number density outside the current sheet, v_o is the size of the distribution function velocity bins, and $\Delta \mathbf{x}_k$ is the distance traveled while located in the k'th box, and Δt_k is the time a particle spent in the k'th box. This method should give the same answers as distribution function integration so it can be used as a simple check.

Both methods depend on knowing precisely the position and time of the entry and exit points of a particle trajectory as it crosses a box edge. One way to find the point where a particle leaves one box and enters an adjacent box is to recast the two first order equations of motion in terms of the independent variable associated with the plane that was traversed.

These equations are subsequently integrated from the current position backward to the plane just crossed. For example, if a particle starts at point $\{x_o, y_o, z_o, t_o\}$ and moves after time step Δt to position $\{x, y, z, t_o + \Delta t\}$ into an adjacent box in the z direction, the time and point at which the box edge located at z_{edge} must be found. Following the method of *Koonin and Meredith* [*Section* 2.5, 1992], a new independent variable s is introduced:

$$\frac{d\mathbf{v}}{dt} = \frac{d\mathbf{v}}{ds}\frac{ds}{dt} = \frac{d\mathbf{v}}{ds}V = \frac{\mathbf{F}}{m}$$

$$\frac{d\mathbf{x}}{dt} = \frac{d\mathbf{x}}{ds}\frac{ds}{dt} = \frac{d\mathbf{x}}{ds}V \tag{3.7}$$

where $V = ds/dt$. Solving for the differential with respect to the independent variable s we get:

$$\frac{d\mathbf{v}}{ds} = \frac{\mathbf{F}}{mV}$$

$$\frac{d\mathbf{x}}{ds} = \frac{\mathbf{v}}{V} \tag{3.8}$$

If the force $\mathbf{F}$ is electromagnetic, then the sign on the charge q and the electric field E must be changed so the particle will spiral in the correct sense when $\mathbf{v}$ is reversed. The particle can then accurately backtrack along its orbit. Conversely one can change the sign of the magnetic field B. This is the form actually implemented by the derivative taking subroutine:

$$\frac{d\mathbf{v}}{ds} = \frac{q}{mV}[E(\mathbf{x}, t) + \mathbf{v} \times (-B(\mathbf{x}, t))] = \frac{q}{mV}[E(\mathbf{x}, t) + B(\mathbf{x}, t) \times \mathbf{v}]$$

$$\frac{d\mathbf{x}}{ds} = \frac{\mathbf{v}}{V} \tag{3.9}$$

The velocity at the starting point of the edge-finding, $\mathbf{v}$, must be passed to the driver subroutine *odeint* as $-\mathbf{v}$ so that the backtracking can occur. The actual independent variable $s = \{x, y,$ or $z\}$ is signaled by an integer flag variable, where a zero value indi-

cates time as the independent variable, one the x coordinate, two the y coordinate, and three the z coordinate.

3.5 Generating the Desired Current Sheet

The fundamental taxonomy of different types of particles was discussed by *Lu* [1993]. Details of single particle orbits for this work will be further discussed in the next chapter. In general, some particle orbits were observed to carry current that strongly peaks near the center of the current sheet. These particles are mirroring. The current carried by groups of particles with figure eight type orbits is negative in the central region and peaks further out. Still other particle orbits exhibit no discernible pattern. The collection of particle families form the library of orbit populations that have predictable plasma properties.

This takes us to the second step where the goal current density

$$\mathbf{j}_{goal}(\mathbf{x}) = (1/\mu_o)\nabla\times\mathbf{B}_{model}(\mathbf{x}),$$ (3.10)

is used to test and reject ion orbit families in the library that can aid in constructing the final ensemble. Ideally,

$$\mathbf{j}_{goal}(\mathbf{x}) = \sum_{g=1}^{k} \omega_g \mathbf{j}_{Tg}(\mathbf{x}),$$ (3.11)

where k is the total number of plasma groups and ω_g is a weight assigned by the fitting procedure to each group. The total electric current for each ion-electron group is the sum of the ion and electron contributions and is given as,

$$\mathbf{j}_{Tg}(\mathbf{x}) = \mathbf{j}_e(\mathbf{x}) + \mathbf{j}_i(\mathbf{x}).$$ (3.12)

This total current is used by the fitting procedure for group selection. The manner in which the electron current contribution is calculated is described in the next section.

Two programs which implement the Levenberg-Marquardt method are available to

perform the fitting procedure, *driver.f* developed using routines from [*Press et al.*, 1993], and an older program with statistics concerning the quality of the fit, *glsws.f* [*Daniels*, 1966]. The families which can best represent the desired current density are then summed to generate full distribution functions. The velocity space is split into $30 \times 30 \times 30$ boxes in the v_x, v_y, and v_z directions. The result is a 27,000-point velocity distribution function for each of the spatial boxes. Depending on the number of 'x-slabs' used, the distribution functions can pose a significant storage problem. These individual distribution functions are combined in a weighted sum, using the previously calculated weights, and the constituent parts are backed up to tape or deleted. At this point the number density, mass density, charge density, bulk velocity, current density, and the pressure and temperature tensors can be calculated from moments of the combined distribution function (see Appendix A).

3.6 Electron Current Contribution

Electrons are introduced by assuming charge neutrality, that they have an isotropic distribution function at the equator, and by using the guiding center approximation. The principal condition that is imposed to generate an approximately self-consistent current sheet is that the ion-plus-electron groups must be combined so that the final collection of particles carries the electric current that is needed to generate the preselected magnetic field in which the orbits were traced. This section describes our method.

Starting from the guiding center approximation [*Parker*, 1957] for a species *s;*

$$\mathbf{j}_s = \frac{\mathbf{B}}{B^2} \times \left[\nabla P_{s\perp} + \left(\frac{P_{s\parallel} - P_{s\perp}}{B^2} \right) (\mathbf{B} \cdot \nabla) \mathbf{B} \right] + n_s q_s \frac{\mathbf{E} \times \mathbf{B}}{B^2}, \tag{3.13}$$

which includes the effects of both guiding center drifts $\mathbf{v}_{gs}$ and the drifts associated with the magnetization currents $\mathbf{j}_{ms} = n_s q_s \mathbf{v}_{ms}$, a calculation of the electron current, $\mathbf{j}_e(\mathbf{x})$,

accompanying each ion group can be made. This requires that not only the magnetization current, the curvature drift current, the gradient drift current, and the $\mathbf{E} \times \mathbf{B}$ drift current, be added together, but also a parallel current in opposition to that produced by the ions is added. These operations are performed by program [$jelectron.f$]. The implemented equations are given as follows. For conditions where a constant zeroth order cross-tail electric field is imposed on the system, it is assumed that the electrons are isotropic $P_{\parallel} - P_{\perp} = 0$ and that $n_i(x, z) = n_e(x, z) = n(x, z)$ so

$$j_e = \frac{\mathbf{B}}{B^2} \times [T_e(x, z)\nabla n(x, z) + n(x, z)\nabla T_e(x, z)] + q_e n(x, z)\left[\frac{\mathbf{E} \times \mathbf{B}}{B^2} + v_{i\parallel}\right] \quad (3.14)$$

where $n(x, z)$ is set equal to a polynomial fit of $n_i(x, z)$ using the fitting program [$glsws.f$]. Additionally, $T_e(x, z)$ is set to one-seventh the polynomial fit of $T_i(x, z)$. The scale factor is set based on observations [*Baumjohann et al.*, 1989].

Calculations made with the constant zeroth order uniform E_y are not charge neutral and give rise to perturbations to the electric field. In practice the electric potential is only about 100 V/R_E for a 5 keV particle. Corrections for perturbed fields assume that the total kinetic energy density for electrons is $\langle W_{\perp} \rangle + \langle W_{\parallel} \rangle = W = \frac{1}{7}W_i$ and that

$\langle W_{\perp} \rangle = 2\langle W_{\parallel} \rangle$ when $\Phi(x, z) \leq 0$. If this were always true there never would be a

$P_{\parallel} - P_{\perp}$ term. However when the electric potential $\Phi(x, z) > 0$ a different expression could be used since $P_{\parallel} - P_{\perp} \neq 0$. The guiding center electron current would then become

$$j_e = \frac{\mathbf{B}}{\mathbf{B}^2} \times \left[T_e(x, z)\nabla n(x, z) + n(x, z)\nabla T_e(x, z) + \left(\frac{P_{\parallel} - P_{\perp}}{\mathbf{B}^2} \right)(\mathbf{B} \cdot \nabla)\mathbf{B} \right] +$$

$$q_e n(x, z)\left[\frac{\mathbf{E} \times \mathbf{B}}{\mathbf{B}^2} + v_{i\parallel} \right] \tag{3.15}$$

$$P_{\perp} = n(x, z)\langle W_{\perp} \rangle$$
$$P_{\parallel} = 2n(x, z)\langle W_{\parallel} \rangle \tag{3.16}$$

One restriction that has been imposed on all ion-electron groups that are run is that a group is discarded if its inclusion does not significantly enhance the self-consistency of the final plasma. The total electric current for each ion-electron group,

$$\mathbf{j}_T(x, z) = \mathbf{j}_e(x, z) + \mathbf{j}_i(x, z), \tag{3.17}$$

is calculated with the program [combine.f]. The resulting $\mathbf{j}_T$ output files are then used by the program [bigfilter.f] to generate input files for the two fitting programs [glsws.f] and [driver.f]. In practice only $j_y(x, z)$ is considered when selecting final groups of particles. This simplifies the fitting procedure and concentrates on those ion-electron groups which are the primary contributors to the cross-tail current. The fitting programs find coefficients, ω_g, that will be used to weight all the other plasma parameters.

When a reasonable combination of plasma groups is found that matches the desired current, the distribution functions associated with each plasma group are combined using the weights ω_g with the program [dfcombine.f]. This final combined distribution function can then be integrated to calculate new combined number density, current density, and bulk velocities:

$$\mathbf{j}_C(x, z) = \sum_{g=1}^{k} \omega_g \mathbf{j}_{Tg}(x, z) \tag{3.18}$$

$$n_C(x, z) = \sum_{g=1}^{k} \omega_g n_g(x, z) \tag{3.19}$$

where k is the total number of plasma groups. The drift velocity of the individual ion and electron groups can be calculated by:

$$v_{s,D}(x, z) = \frac{j_{s,g}(x, z)}{q_s n_{s,g}(x, z)} . \tag{3.20}$$

3.7 Electric Field

Particles are initially followed in a system with a constant cross-tail electric field. This zeroth order field does not guarantee that the final plasma will be neutral everywhere. To be as nearly self-consistent as possible, ion orbits can be retraced using an electric field modified to accomodate certain assumptions. First of which is the assumption of electron isotropy at the equator. Second, the electron number density $n_e(x, z)$ is set equal to the polynomial fit of $n_i(x, z)$ so the resulting plasma is approximately neutral. By establishing these conditions the new electric field will have a component parallel to $\mathbf{B}$. This first order parallel electric field is is added to the zeroth order uniform E_y. The Boltzmann relation is used to calculate the electric potential difference Φ between each (x, z) box and a reference point (x_o, z_o) on the same field line. The electric field is then calculated from $\mathbf{E} = -\nabla\Phi$. The procedure is implemented as follows.

Electrons are decelerated when $n_C < n_o$ so the potential $\Phi(x, z) \leq 0$ can then be calculated using the Boltzmann relation

$$\frac{n_c(x, z)}{n_o} = e^{-\frac{q\Phi(x, z)}{T(x,z)}} . \tag{3.21}$$

where the constant n_o is the density on the field line at the equator. The potential $\Phi(x, z)$ associated with the polynomial fit of $n_C(x, z)$, is calculated using [ntophi2d.f]. Electrons

are accelerated as they move away from the equator when $n_C > n_o$ and the potential

$\Phi(x, z) > 0$. This situation can be handled by the calculation derived by *Lu* [1993],

where equation (3.21) becomes

$$\frac{n_C(x, z)}{n_o} = 2\left[-\frac{q\Phi(x, z)}{\pi T(x,z)}\right]^{1/2} + \left[1 - \text{erf}\sqrt{-\frac{q\Phi(x, z)}{T(x,z)}}\right]e^{-\frac{q\Phi(x, z)}{T(x,z)}}. \tag{3.22}$$

A polynomial fit of the electric potential, $\Phi(x, z)$, using the fitting program

glsws.f, is then calculated. The coefficients are saved to a file for later use by the particle

tracing program. Letting $\bar{x} = x - x_o$, where x_o is the inner edge of the modeling region,

permits the fitting programs to converge faster. The scalar potential is

$$\begin{aligned}
\Phi(x, z) = &[a_{000} + a_{001}z + a_{002}z^2 + a_{003}z^3 + a_{004}z^4 + a_{005}z^5] \\
&+ [a_{100} + a_{101}z + a_{102}z^2 + a_{103}z^3 + a_{104}z^4 + a_{105}z^5]\bar{x} \\
&+ [a_{200} + a_{201}z + a_{202}z^2 + a_{203}z^3 + a_{204}z^4 + a_{205}z^5]\bar{x}^2
\end{aligned} \tag{3.23}$$

The particle groups are then retraced in the same $\mathbf{B(x)}$ with the new $\mathbf{E(x)}$. The

electric field calculation, performed by subroutine [*do_efield.f*], is then a simple gradient

of the scalar potential polynomial, $\mathbf{E} = -\nabla\Phi$. The process of calculating ion ensembles,

determining the electron current contribution and the new electric field is performed until

the new $\mathbf{E(x)}$ has converged to the previous $\mathbf{E(x)}$.

Using the final weighting from [*glsws.f*], the final combined ion distribution func-

tion is generated by adding together the individual distribution functions [*dfcombine.f*]

$$f_C(\mathbf{x},\mathbf{v},t) = \sum_{g = 1}^{k} \omega_g f_g(\mathbf{x},\mathbf{v},t). \tag{3.24}$$

The final plasma parameters can then be calculated by using velocity moments of

the combined ion distribution functions (see Appendix A). The parallel and perpendicular

components of temperature and pressure with respect to the magnetic field $\mathbf{B}$ can then be

calculated by rotating the $P_{ji}(x, z)$ tensor through θ_B and ϕ_B, the polar and azimuthal angles between the z axis and $\mathbf{B}$. For a gyrotropic distribution the off diagonal values are zero and $P_\perp = P_{11} = P_{22}$, and $P_\parallel = P_{33}$. These plasma parameters will be presented for the model current sheets in the next chapter.

3.8 Software Implementation

Aside from the physics behind the project, the software implementation has involved thousands of hours of work to translate the needs of the project into intelligible computer codes. In this section an overview of the software will be given while leaving details of the actual code to appendices. The computer hardware configuration used in the software development process is given in Appendix B. The internet site where the entire software package is available is given in Appendix C. Subsequent appendices provide short descriptions of the primary programs and their subroutines.
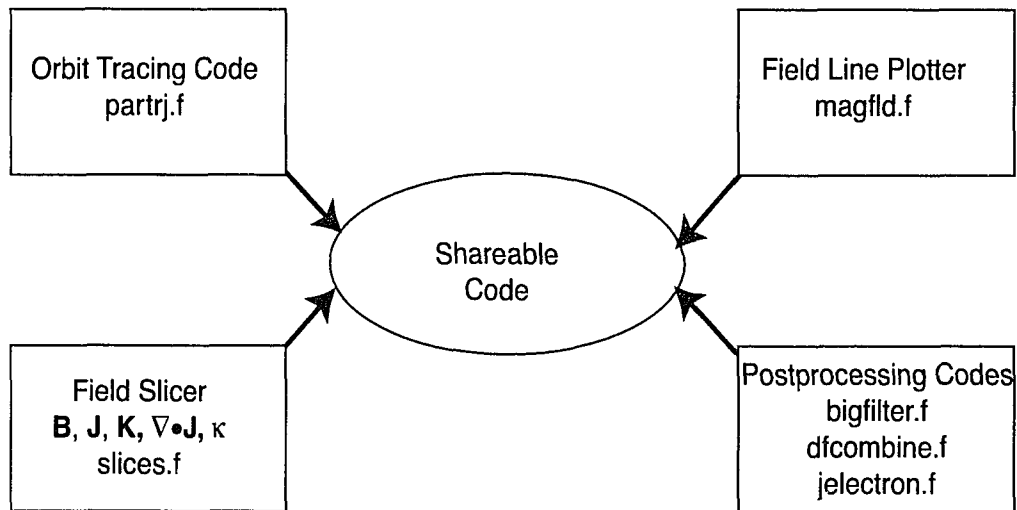
Figure 3.5: Relationship between primary codes

The steps involved in running the particle tracing code and the associated post processing codes have been described from the viewpoint of the physics. Many of these steps

can be automated with shell scripts under the Unix operating system. The advantage being that all interactive inputs can be preset by the shell program so that the user need only change a handful of parameters when highly repetitive operations are performed.

3.9 Sources of Error

Sources of error can be considered as either algorithmic or computational. The algorithmic errors result from the method of discretizing and solving the equation of motion. The computational problems occur due to issues associated with machine word size and roundoff during floating point operations.

As an example of machine errors, consider an ion traced with the same adaptive stepsize driver but with the fourth-order Runge-Kutta and the Bulirsch-Stoer formulas. The Runge-Kutta method generates three orders of magnitude more points for the same trajectory as the Bulirsch-Stoer method. It is considered very stable. This method can be used for discovery of what the appropriate word size for the position, velocity, and time variables should be for any trajectory. This is accomplished by following a particle using the Runge-Kutta method for a time long enough to establish a benchmark. Then, using the endpoint of this particle as a new starting postion, tracing back in the reverse time. Assuming the integrator is working correctly, the new path should return to the benchmark starting position. Given a test particle that is chaotic, it can be seen that roundoff errors resulting from single precision variables will yield different answers from run to run and between different types of computer. These errors are much smaller with double precision variables. The process can then be repeated with the faster Bulirsch-Stoer method.

3.10 Software Limitations

The usefulness of the software is hampered by the tools available to analyze the output. Quality scientific visualization tools that are easy to use and tailor to the output formats

of the particle code would help in discerning meaningful physical effects in the data.

3.11 Future Enhancements

The physics capabilities of the software can always be improved. Looking at the particle injection methods implemented thus far, several new methods could be added. A streaming Maxwellian injection would be a enhancement for beam studies. Another method to add would be to allow particles to be injected over spatial ranges or volumes, this would minimize any effects associated with single point injection. An easier upgrade would be to accommodate the magnetic field model code package distributed by the Goddard Space Flight Center (GSFC) which includes many versions of global magnetospheric models created by Tsyganenko. This would entail changing the *do_bfield* subroutine. A more difficult challenge lies in the proper handling of electrons.

The software, irregardless of the physics, can be improved to take greater advantage of reusable functions and subroutines as well as a more user friendly graphical user interface. The Tool Command Language (Tcl) and the Tk toolkit could provide a rapid development path to a graphical X window interface to some of the programs [*Gladden and Dubois*, 1995]. Conversion to a language such as C could be done but does not provide a new level of functionality. Using an object oriented language like C++ should be done only as a ground up rewrite to better take advantage of the paradigm. All of the software processes involved in this numerical experiment framework should use generic cross process variable names that have the same meaning to facilitate readability.

Chapter IV

CROSS-TAIL CURRENT SHEET RESULTS

4.1 Introduction

This chapter presents results from the SCOT technique using the thin, standard, and thick magnetotail models discussed in chapter two. Monoenergetic ion groups with $1.5, 5,$ and 15 keV starting energies were used. Fixed starting energies rather than Maxwellian distributions are used for these calculations because the identification of the orbital classes that are most important to generating self-consistent current sheets is a main goal. Most ions in a group with a given energy tend to follow a specific type of trajectory. Since the ion energies change as particles drift in the uniform $E_y = 0.3$ mV/m or 1.9 kV/R_E field imposed on the magnetotail models, a spread of energies in the final distribution functions results. However, ions injected at any one location are concentrated in a relatively small energy band, so that a specific orbit type tends to dominate on a given field line.

4.2 Orbit Types

Ion orbits in the magnetotail usually are classified according to the particle's dynamical characteristics, e.g. a chaotic, resonant, or guiding center orbit. Particle dynamics are strongly dependent upon κ. However it was found that the cross-tail current pattern $j_y(x, z)$ depends primarily upon the particle's mirror point location rather than upon the dynamic orbital characteristic. Since the primary goal was to generate a self-consistent current sheet, this work categorizes orbits into 3 groups according to mirror points. These three

groups are labeled as inner, central, and outer mirroring particles. Defining the character-

istic distance a proton that starts at $z = 0$ will move before being deflected by 90° with the

transcendental equation, $z_o = mv/[qB_x(z_o)]$, these labels can be quantified. Particles that

are trapped within a distance $2 z_o$ of $z = 0$ are considered inner mirroring, particles that mag-

netically mirror beyond $2 z_o$ but within the principal current sheet are central mirroring, and

particles that mirror closer to the Earth are outer mirroring. The following section will show

that a contribution from each of the above three orbit categories was needed to create a self-

consistent current sheet that realistically approximated the Earth's magnetotail.

Orbit categories and tracing

Figures 4.1 to 4.3 show sample orbits in the standard tail model. These examples

illustrate most of the important features of non-guiding-center trajectories. All the basic or-

bit types that were previously identified in 1-D tail models [e.g. *Kaufmann et al.*, 1994] are

seen somewhere in the 2-D tail model. Orbits shown in the present section also illustrate

the physical manner in which particles carry cross-tail current, and the importance of mag-

netization currents.

The x-z and x-y projections of the proton trajectory in Figures 4.1a and 4.1b show

several characteristic patterns. This proton began with 5 keV of energy at $(x, y, z) = (-18.5,$

$0, 0.5) R_E$ when tracing started. The ion mirrored once in the northern hemisphere as it drift-

ed Earthward from the starting point, became briefly trapped near $x = -16$ to $-18 R_E$, and

then mirrored three times in the southern hemisphere. The first of these 3 southern hemi-

sphere mirror points was within the principal current sheet. The orbit then was traced back-

wards in time from the starting point, showing that this proton also had been trapped at $|z|$

$< 2 z_o$ between $x = -29$ and $x = -20 R_E$. This alternation between periods of being trapped

near $z = 0$ and periods of magnetically mirroring at various points is typical of chaotic or-

bits. For this ion energy and magnetic field, trapped protons do not get beyond approximately $|z| = 0.5$ R_E before returning to $z = 0$. The approximate dividing line between the central mirroring particles and outer mirroring particles is that the former protons do not move beyond approximately $|z| = 2$ R_E before returning to $z = 0$ for the models used here.

Since the -20 $R_E < x < -14$ R_E, $0 < |z| < 2$ R_E region was being modeled, orbit tracing was stopped on the Earthward side when the ion crossed $z = 0$ at a point at least 2 gyroradii Earthward of $x = -14$ R_E. Similarly, tracing backwards in time was stopped when the ion crossed $x = -20$ R_E at least 2 gyroradii beyond $|z| = 2$ R_E. An equatorial crossing tailward of the field line that connects to $x = -20$ R_E, $z = 2$ R_E plus 2 gyroradii also can be used to stop back tracing. It is evident from Figure 4.1 that no specific particle boundary conditions were imposed at the edges of the region of interest, and that nothing physically important took place at the point at which orbit tracing started. Starting points were selected to get groups of ions that were dominated by a particular trajectory type. For example, starting the ions with an isotropic distribution at $z = 0$ gives a group that has many trapped ions near the starting location, while no ions that start at large $|z|$ are initially trapped.

Cross-tail drift and current

Figure 4.1b illustrates the physical manner by which the total net cross-tail drift becomes relatively independent of the details of a trajectory and of deviations from guiding center motion. This figure also illustrates differences between orbits in 1D and 2D models. Note that for orbit segments with mirror points near the Earth, particles follow almost the same field line as they move down to and back from a mirror point. Protons mirroring near the Earth with energies of about 5 keV in this magnetic field appear to simply bounce off the current sheet when they reach the equator (Figure 4.1a).
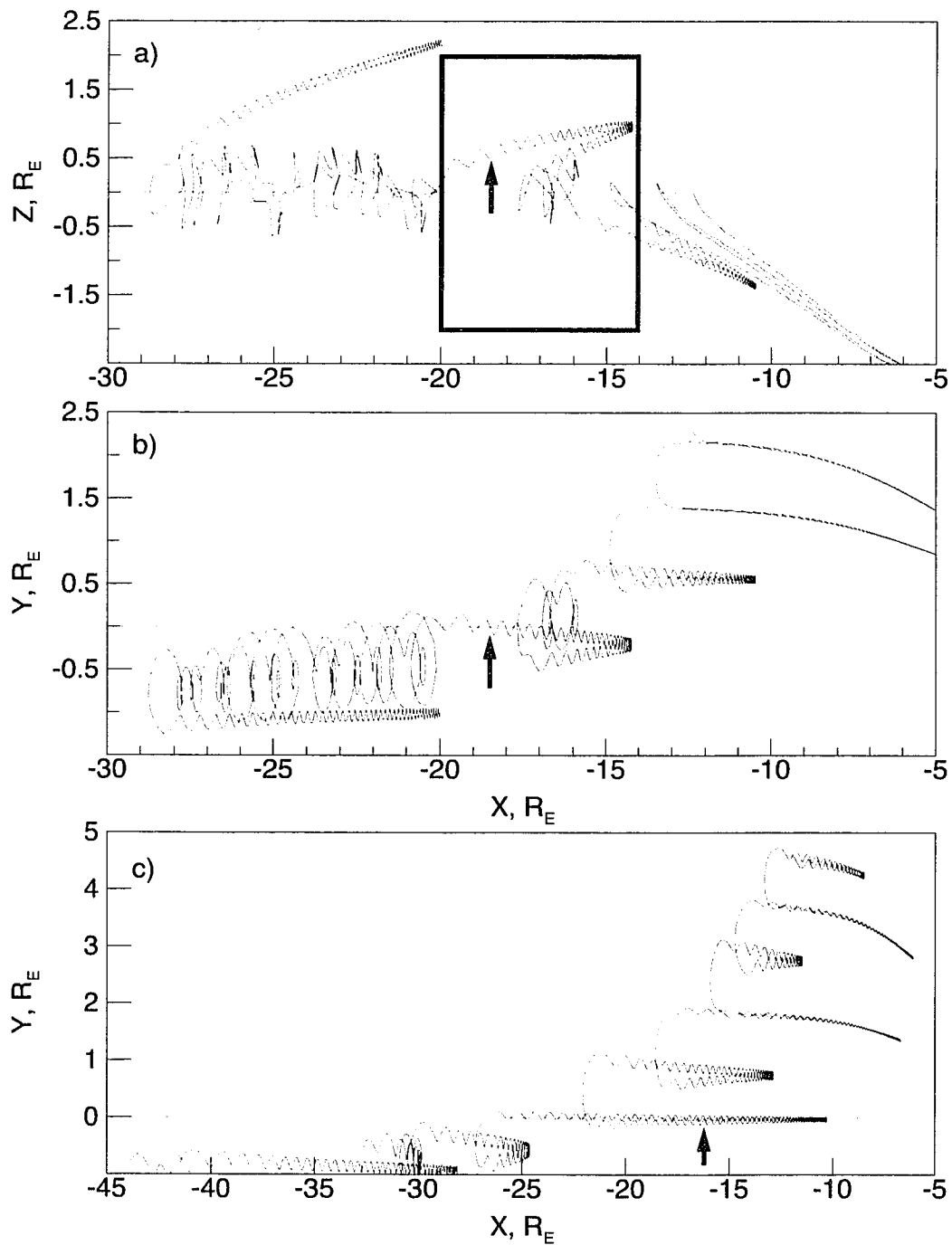
Figure 4.1: Projections of a Standard model/5 keV proton orbit where a) and b) are started at (-18.5,0,0.5) and c) is started at (-16.5,0,1.5). The arrows indicate starting position. The box in plot a) indicates the spatial region studied.
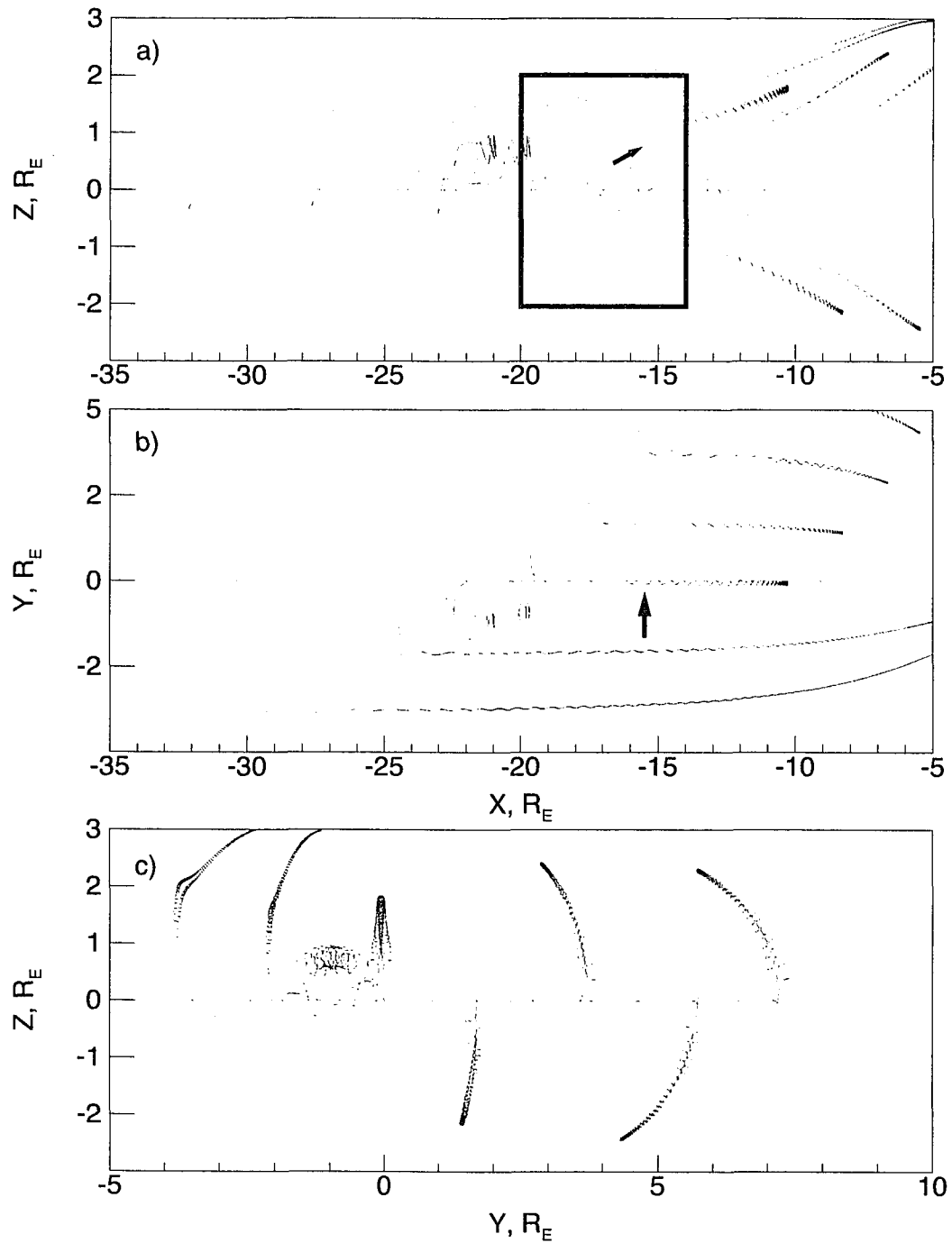
Figure 4.2: Projections of a Standard/15 keV proton orbit . Panels a), b), and c) are different projections of the proton started at (x,y,z)=(-15.5,0,1.0) R_E. This ion passes through both the N=1 and N=2 resonances. The arrows indicate starting position. The box in plot a) indicates the spatial region studied.
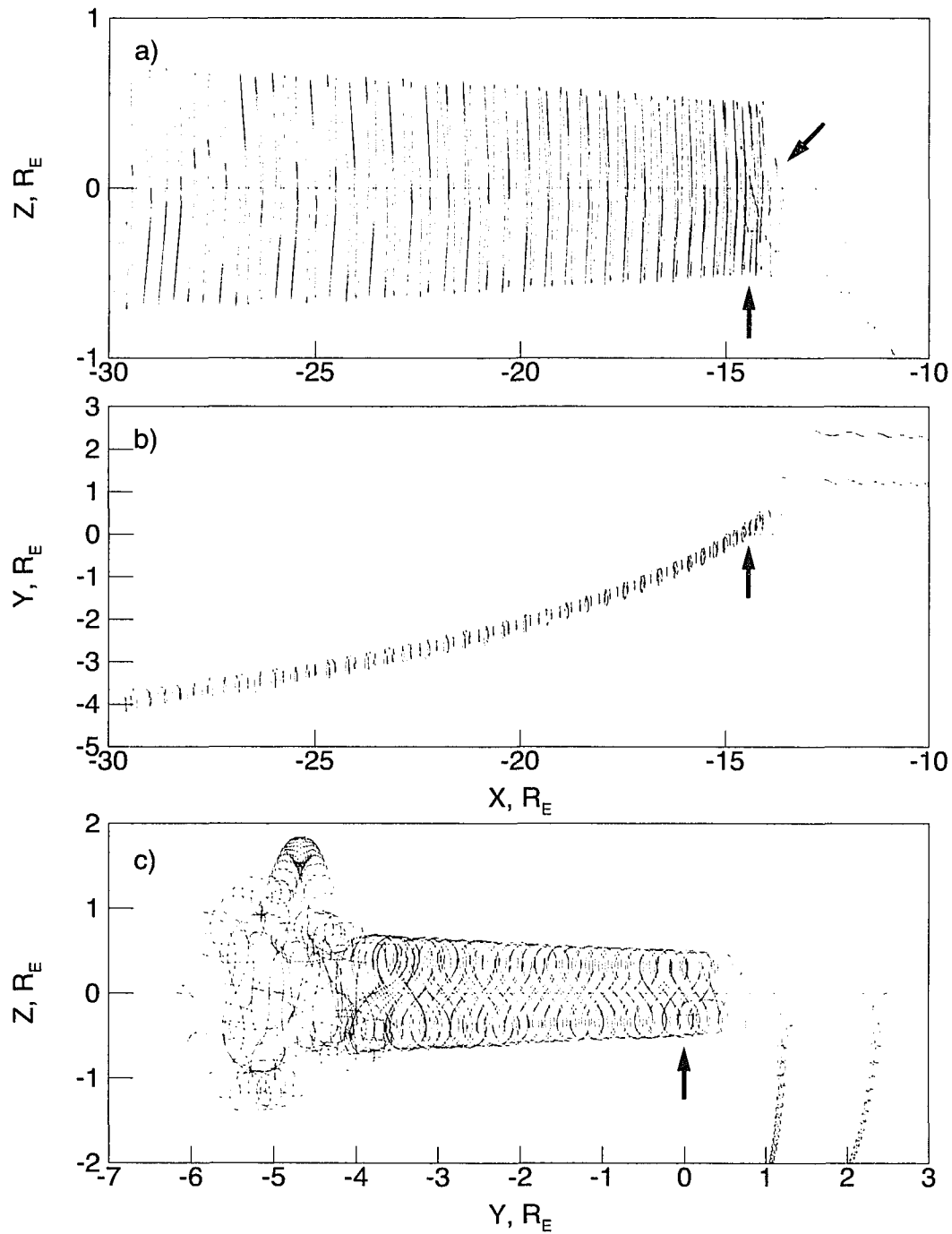
Figure 4.3: Example of a long-lasting simple figure 8 drift pattern. Panels a), b), and c) are different projections of a Standard model/15 keV proton started at (x,y,z)=(-14.5,0,0) R_E. The arrows indicate starting position.

Mirror points on the orbits immediately before and after a given current sheet interaction are nearly the same if the particle's κ parameter is close to a resonant value. The mirror points of chaotic particles generally are different after each current sheet interaction. However, we grouped all resonant and chaotic particles that mirror near the Earth into the same category because $j_y(x, z)$ in our region of interest is almost the same for these two dynamically different trajectory classes. Whenever the mirror point is near Earth, the total cross-tail displacement achieved in one full bounce is approximately equal to 2 gyroradii based on B_{zo}. Note that different scales are used for the x, y, and z axes in Figure 4.1, so that circular motion near $z = 0$ appears to be stretched in the y direction. The motion of particles that mirror at low altitudes in 2D and 3D models is similar to the motion of untrapped particles in a 1D model. In all these cases, $j_y(x, z)$ is concentrated in a sheet near $z = 0$ that is much thinner than that required to self-consistently generate the standard model magnetotail.

Figure 4.1b shows that this ion drifted part way back in the negative y direction when it mirrored within the current sheet, near $z = -1.5\ R_E$, $x = -10\ R_E$ and near $z = 0.7\ R_E$, $x = -15\ R_E$. In both cases, there was a substantial net cross-tail drift during the full period between two adjacent current sheet interactions. This is one of the most important differences between 1D and either 2D or 3D models. Field gradients in the x direction result in a net cross-tail drift for particles that mirror in the current sheet. In the 1D models, all mirroring particles drift equal distances in the $+y$ direction near $z = 0$ and in the $-y$ direction as they mirror. Self-consistent 2D and 3D models can be constructed with lower total plasma densities than 1D models because inner mirroring particles carry a net cross-tail current in x dependent models.

Figure 4.1b also shows that there was some net cross-tail drift per current sheet interaction during the periods when the ion was trapped at $|z| < 0.5\ R_E$, beyond $x = -20\ R_E$. This helps to explain why the bounce-averaged drift velocity is relatively weakly dependent on orbit type. Trapped particles make many current sheet interactions, but have a net cross-tail displacement per interaction that is much less than 2 gyroradii. Particles mirroring near the Earth have few current sheet interactions, but have a net displacement of nearly 2 full gyroradii during each interaction.

Figure 4.1c shows another important characteristic of magnetotail current carriers. This trajectory is characterized by a series of events in which the ion mirrors and then essentially bounces off the current sheet. The cross-tail motion tends to increase modestly for each current sheet interaction as the ion moves into the inner tail because the ion is gaining energy. However, it is more important that the Earthward drift speed is decreasing at low altitudes. The ion moves Earthward by as much as $10\ R_E$ during the time required to mirror when its equatorial crossing point is near $x = -30$ to $-40\ R_E$. Earthward motion is only about $1\ R_E$ per mirror cycle near $x = -10\ R_E$. This decrease in Earthward drift is the primary reason that the displacement between adjacent equatorial crossing points is primarily in the x direction in the distant tail and primarily in the y direction in the near-Earth tail.

Figure 4.2a, b, and c show x-z, x-y, and y-z plots of a proton that started at $(-15.5, 0, 1.0)\ R_E$ with 15 keV of energy. This high energy proton passed through both the $N = 1$ and $N = 2$ resonances. Resonances are characterized by symmetric orbits that involve little net change in magnetic moment. A resonant ion crosses the $z = 0$ plane $N+1$ times during each current sheet interaction [Büchner and Zelenyi, 1989]. The κ parameter of the particle in Figure 4.2 decreased from a little more than 0.5 at the $x = -32\ R_E$ crossing, which lies

near the $N = 1$ resonance, to about 0.3 at $-15\ R_E$, which is near the $N = 2$ resonance. Note that the ion crossed $z = 0$ twice during each of the 2 most distant neutral sheet interactions before it became briefly trapped, and then crossed $z = 0$ three times during each of the 4 most Earthward interactions. The magnetic moment and the mirror magnetic field changed substantially during the crossings at $-25\ R_E < x < -20\ R_E$ when κ was near 0.4. This behavior is typical of chaotic motion. The magnetic moment happened to change relatively little during each of the other crossings, even though not all were very close to a resonant κ.

Figure 4.3a, b, and c show x-z, x-y, and y-z trajectory projections for a proton that started with 15 keV of energy at $(-14.5, 0, 0)$. Although it is unusual to last nearly this long, the orbit shows that it is possible for a proton to remain trapped in a very simple pattern as it drifts Earthward all the way from $x = -30\ R_E$ to $x = -15\ R_E$. The κ parameter changed substantially in this interval. This orbit is referred to as a figure 8 pattern because of its appearance in the y-z projection. Figure 8 ions and other ions that are trapped near $z = 0$ carry current in the positive y direction when they are farthest from $z = 0$ (at $|z| > 0.3\ R_E$ in Figure 4.3c) and in the negative y direction at smaller $|z|$.

4.3 The model 2-D current sheets

All of the cases considered here used 40 z boxes in the range $-2 < z < 2\ R_E$. The model is symmetric about $z = 0$, so orbital information at equal distances above and below $z = 0$ can be combined into 20 boxes that are 0.1-R_E thick. The folding of boxes in the z dimension only applies to models symmetric in z. This software feature is also available for models symmetric in the x and y dimensions but is not utilized in this study. The midtail region $-20 < x < -14\ R_E$, is divided into six 1-R_E wide x boxes yielding a total of 120 spatial boxes.

The velocity space of the distribution functions are split into $30 \times 30 \times 30$ boxes in

the v_x, v_y, and v_z directions. The result is a 27,000-point velocity distribution function for each of the 120 spatial boxes. As discussed in chapter 3, the distribution functions were evaluated by adding the time spent for each step along a trajectory into two of the velocity-spatial boxes, where half of the timestep goes into the initial velocity bin and the latter half into the new velocity bin of the current step.

Integrating the distribution functions for each box gives the current $\mathbf{j}_i(x, z)$ as well as other plasma parameters. Adding electron and ion contributions gives the total $\mathbf{j}(x, z)$ in each box. The resulting $\mathbf{j}$ includes all drift and magnetization currents. In practice, the SCOT method uses $j_y(x, z)$ as the sole parameter in the least squares fit that selects the final groups of particles. The final combination therefore carries a cross-tail current which approximately equals that needed to generate the preselected magnetic field. In a 2-D model with $B_y = 0$ and $\partial/\partial y = 0$, the required $\mathbf{j} = (1/\mu_o)\nabla \times \mathbf{B}$ is all in the y direction. With the imposed E_y, both ions and electrons $\mathbf{E} \times \mathbf{B}$ drift in the x-z plane. Ions and electrons $\mathbf{E} \times \mathbf{B}$ drift at the same speeds in the guiding center approximation, so they are not associated with a net current in regions where the guiding center equations are valid.

Figure 4.4 is an example of the library of orbit populations that are generated for a typical case. The figure is composed of 30 individual plots. The number of plots is based on there being 6 x and 5 z starting points for the particle groups. The 6 x starting points for the particle groups were $x = -14.5, -15.5, -16.5, -17.5, -18.5,$ and -19.5 R$_E$. The 5 z starting points used for the different groups were $z = 0, 0.5, 1.0,$ and 1.5 R$_E$ at the center of each of the six x-boxes, plus at $z = 2.0$ R$_E$ on field lines that cross the equator at the centers of each x box. Each particle group has 1000 ion orbits with the same (x, z) starting position. The 30 panels in the figure portray the velocity moment of the $j_y(x, z)$ current at

all the spatial box locations. Since there are 6 x boxes and 20 z boxes, there are 120 points in each panel. The format of the individual plots will also be used in other plots. The abcissa is subdivided by 6 tickmarks associated with the 6 x boxes where the leftmost x box is the $-20 < x < -19$ R$_E$ range and the rightmost x box is the $-15 < x < -14$ R$_E$. Within each x box are the 20 points corresponding to the 20 z boxes, $0 < |z| < 2$ R$_E$. Why was a contour plot not employed? The answer is twofold; one, a contour plot would smooth away features associated with the orbit types; and two, the plots show what features the fitting regime selects and rejects. Subsequent uses of the format will not be as compressed and so will be easier to visualize. As a further example of this scheme, the third column of Figure 4.5f is similar in style to the panels of Figure 4.4 and is itself rescaled to a much larger size in the last row of Figure 4.9.
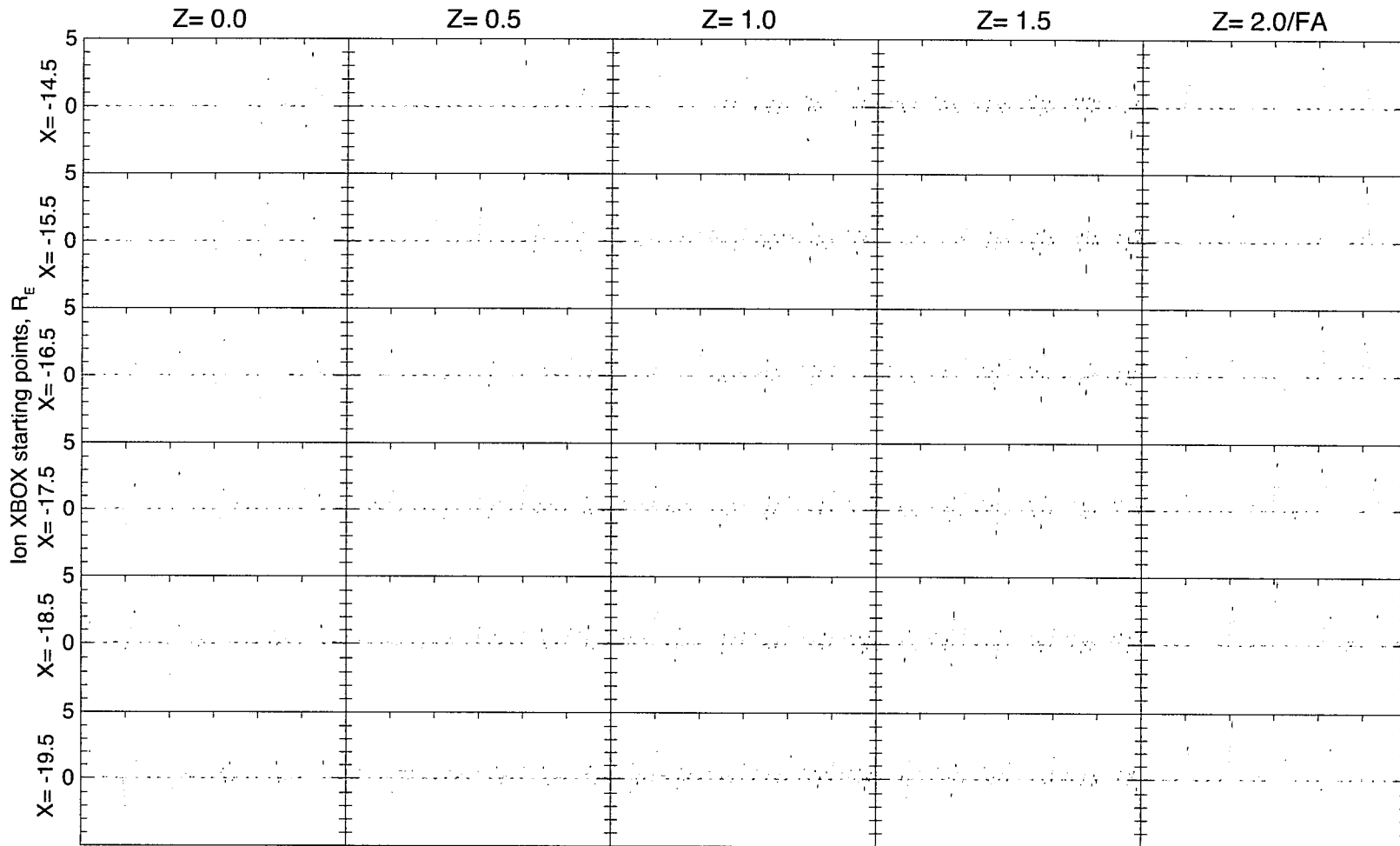
Figure 4.4: Current density j_y[nA/m^2] of thirty ion groups for the Thick current sheet with starting energy of 5 keV. The abcissa of each plot is subdivided by 6 tickmarks associated with the 6 x boxes where the leftmost x box is the -20<x<-19 R$_E$ range and the rightmost x box is the -15<x<-14. Within each x box are the 20 points corresponding to the 20 z boxes, 0<|z|<2 R$_E$.
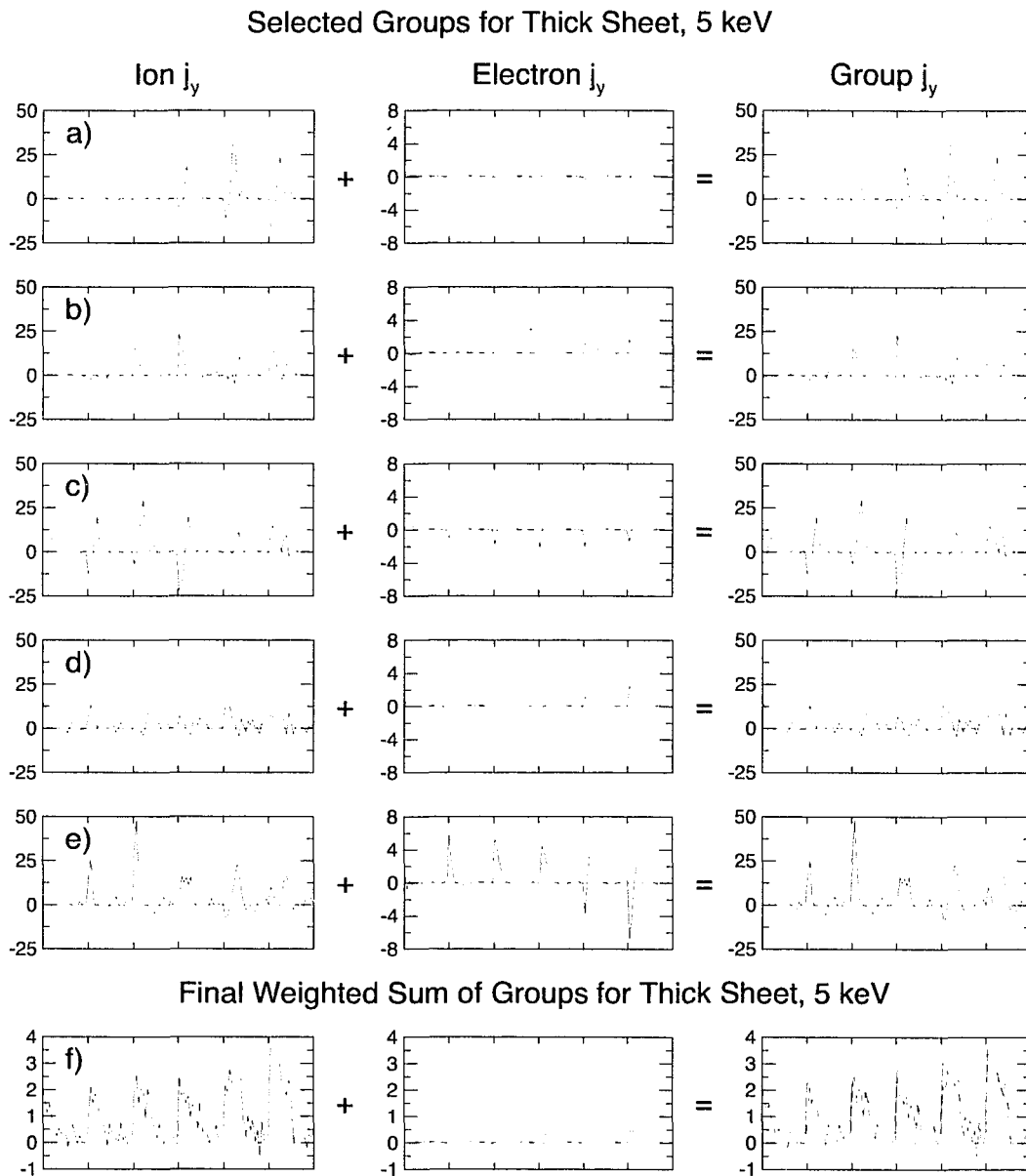
Figure 4.5: Fitting procedure example where plots a-e are the individual ion and electron current groups which are combined in a weighted sum to generate the goal current sheet shown in plot (f). All scales are in [nA/m^2]. The injection locations are a) $x = -15.5$, $z = 0$; b) $x = -15.5$, $z = 0.5$; c) $x = -17.5$, $z = 0$; d) $x = -17.5$, $z = 0.5$; e) field aligned particles started at x=-8.837402, $z = 2.0$ pass through $x = -19.5$, $z = 0$; f) The final weighted combination of the individual ion plus electron groups where the third column has the goal in solid black and the fit is the jagged line.

An example of the fitting procedure

As an example of the fitting procedure, the five groups used to generate the thick model/5 keV current sheet are presented in Figure 4.5. The first column of plots in Figure 4.5 show the current carried by the protons that were initially started at 5 keV. The second column, Figures 4.5a-4.5e, are the associated electrons for the ion groups.

The third column, Figures 4.5a-4.5e, is the combination of the ion and electron groups that were used to generate the best fit. Figure 4.5f is the final weighted sum of these groups that comprise the final current sheet. Current distributions produced by the individual ion groups in the ion j_y column of Figure 4.5 show the patterns described qualitatively in the discussion of individual orbits (Figures 4.1 to 4.3). For example, many figure 8 and other trapped orbits appear in the group of particles shown in Figure 4.5a, which started at $z = 0$ at $x = -15.5\ R_E$. This is the second of the six x-blocks from the right. The resulting ion current shows the characteristic negative j_y at $z = 0$ and positive j_y beyond z_o, which is near or below $0.3\ R_E$ for 5 keV protons in the region of interest. The above current pattern is dominant in the starting and adjacent x boxes (three rightmost blocks in the panel) because many particles remain trapped for only a few current sheet interactions. Similarly, the ion j_y panel in Figure 4.5c shows currents carried by ions that started at $z = 0, x = -17.5\ R_E$. The characteristic trapped particle $j_y(x, z)$ pattern here appears in the more distant x-boxes (blocks on the left side).

There is a net drift of all trapped ions in the positive y direction, as shown previously in Figures 4.1 to 4.3. The net positive current appears in Figures 4.5a and 4.5c because the area under the positive j_y spikes is a little larger than the area under the negative spikes. However, the structure of $j_y(x, z)$ clearly is dominated by the sharp positive and negative peaks, which are associated with magnetization currents, rather than by a small relatively

uniform positive j_y at $|z| < 0.5 \ R_E$ as would be predicted by the simple guiding center drift equation. Figures 5a to 5e are typical of the groups studied. For example, essentially any group of ions that is randomly selected from a generally isotropic distribution at $z = 0$ has a j_y structure that is qualitatively similar to those shown if Figures 4.5a and 4.5c.

Ions in Figure 4.5e were started at $z = 2 \ R_E$ on a field line that crosses the equator at $x = -19.5 \ R_E$. These ions with low mirror points carry cross-tail current that is strongly confined near $z = 0$ when they first bounce off the current sheet, in x boxes near the left side of the ion j_y panel in Figure 4.5e. The current is less well confined during succeeding bounces at lower altitudes because some ions mirror closer to $z = 0$ or became trapped during these later interactions. Again, this $j_y(x, z)$ structure is typical of any group of particles that is selected to be generally isotropic far from $z = 0$, regardless of the particle's κ or dynamical characteristics. The principal difference between particles on chaotic and resonant orbits is that resonant particles would maintain low mirror points for several bounces, so the pattern of narrow regions with strong positive j_y would be maintained for a larger region in the x direction. Chaotic particles become more nearly isotropic each time $z = 0$ is reached, so the group would not continue to be dominated by particles with low mirror points after one or two current sheet interactions.

Rows b and d in Figure 4.5 show currents carried by ions that started with an isotropic distribution at $z = 0.5 \ R_E$, with $x = -15.5$ and $-17.5 \ R_E$ respectively. These groups are dominated by outer mirroring ions beyond $z = 0.5 \ R_E$. The associated j_y patterns tend to be complex, but reproducible in all details. Trapped ions with mirror points throughout the current sheet are needed to broaden the current carried by 5 keV protons so they can produce a sheet with a characteristic scale length of $0.5 \ R_E$ or larger.

None of the individual ion groups has a j_y structure that is similar to the goal, which is needed in a self-consistent model, as shown by the solid curve in the group j_y panel of Figure 4.5f and in the 5 keV row of Figure 4.9. The low mirror point group (Figure 4.5e) produces much too thin a current sheet. However, if some of the trapped particle group current (Figures 4.5a and 4.5c) is added, it will decrease the positive current very close to $z = 0$ and add some positive current at larger $|z|$. This is the least square fitting procedure used in the SCOT technique, and described previously [*Kaufmann and Lu*, 1993]

A linear combination using all 30 particle groups that were traced for each of the 9 cases studied would yield the best least squares fit to the $j_y(x, z)$ that is needed to generate the tail magnetic field. However, a principal goal of this study was to see which orbit types were essential for the production of a self-consistent current sheet. For this reason, only those groups that improved the fit at a 95% confidence level were retained. Of the 30 starting groups, only 5 to 9 were kept after imposing this requirement. The thick-5 keV case shown in 4.5 is used to illustrate that matching the goal current density can be done with a minimal number of groups.

The quality of this fit is typical of the set of 9 cases studied. Figure 4.4 shows $j_y(x, z)$ carried by each of the 30 groups of 1000 ions that were traced for this thick model/ 5 keV case. All ions were started so they would yield an isotropic distribution if they had been injected in a uniform **B**. The actual distribution functions are not isotropic even in the starting box because ions can return to this box with different pitch angles after passing through $z = 0$. Each small panel in Figure 4.4 uses the same format as Figure 4.5. It is evident that no single group of particles carries a current distribution that is similar to the current needed for self-consistency, as shown by the dashed line in Figure 4.5f and the
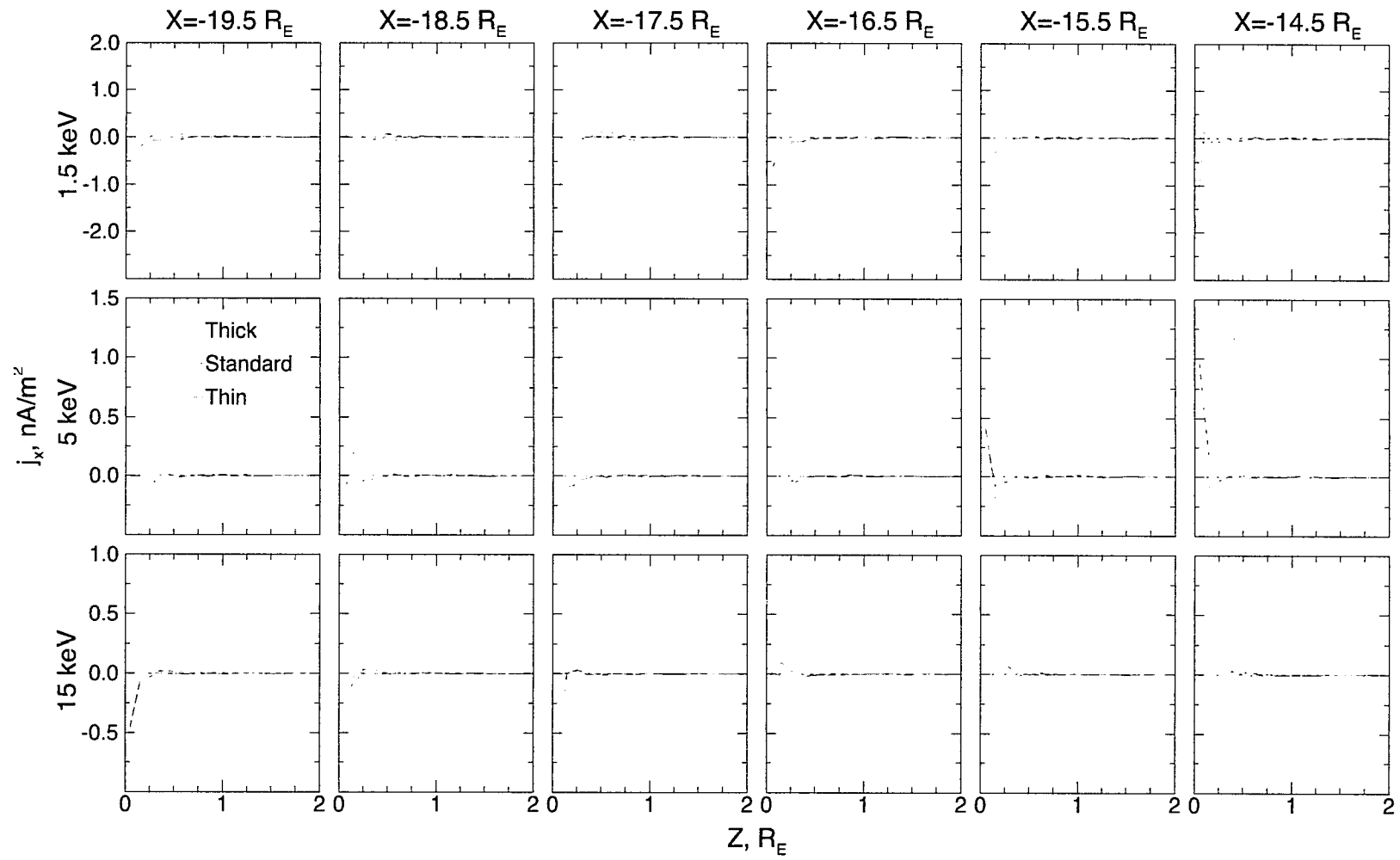
Figure 4.6: Current density j_x [nA/m^2] for all cases.
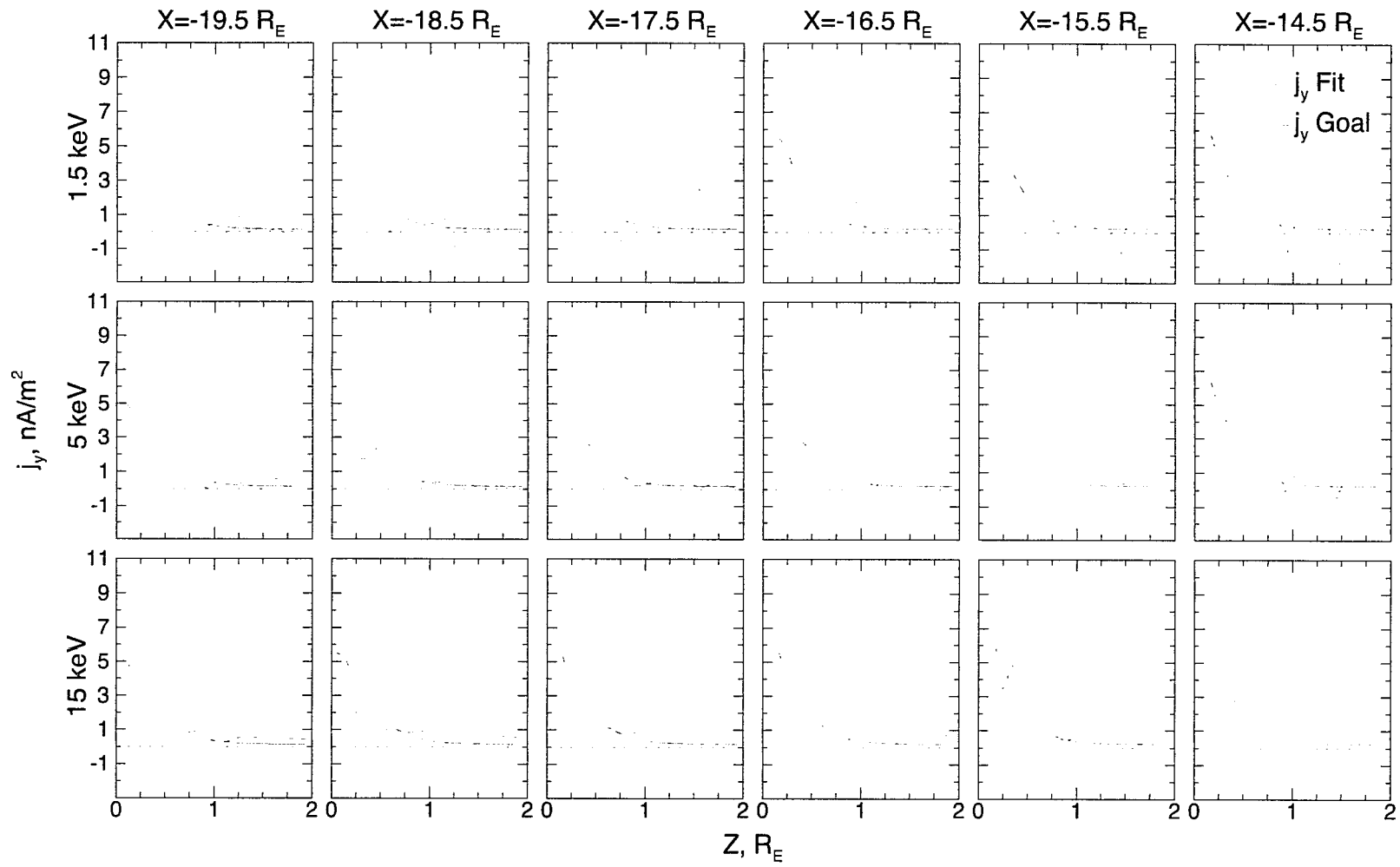
Figure 4.7: Thin model current sheet, fit and goal.
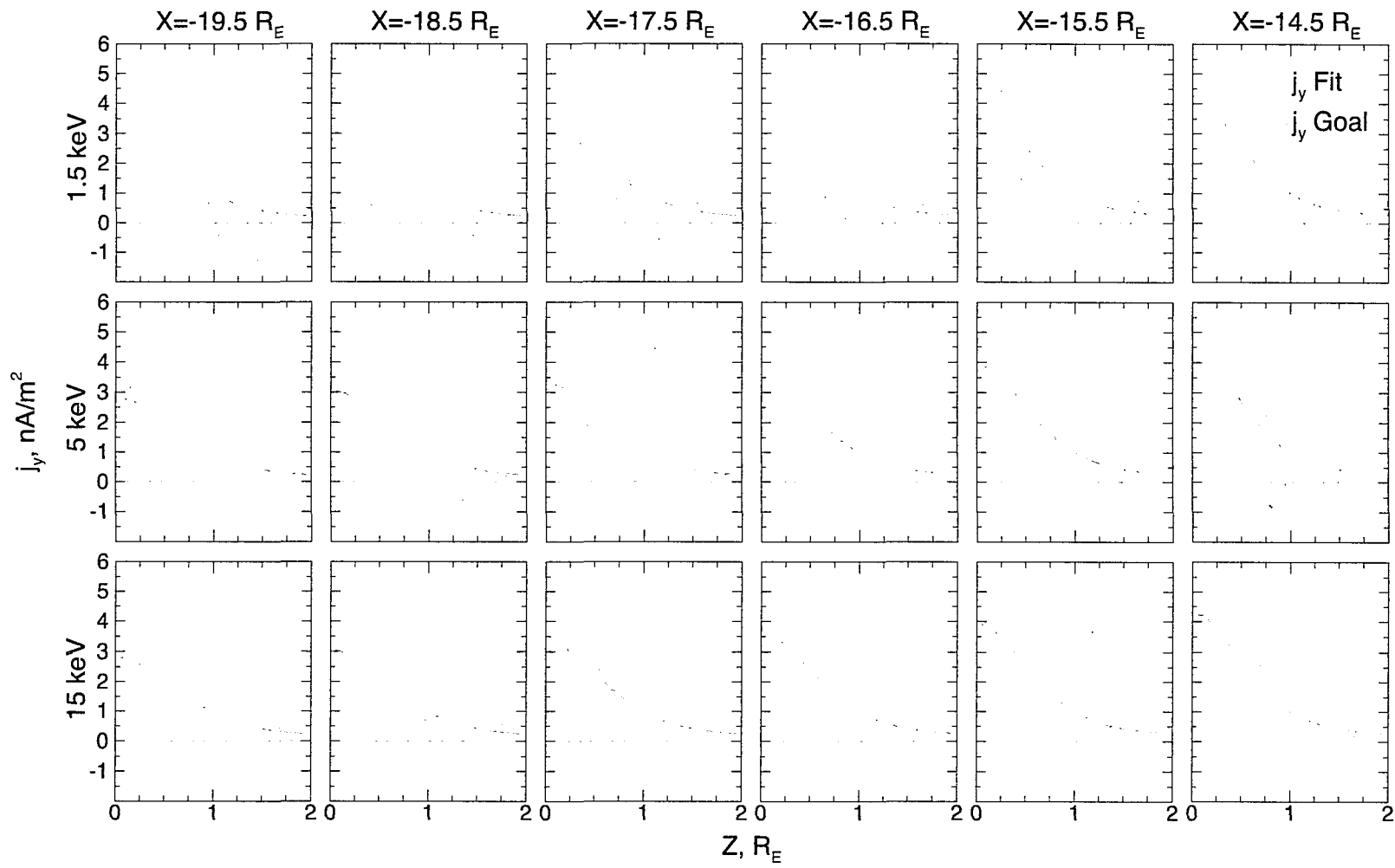
Figure 4.8: Standard model current sheet, fit and goal

| X=-19.5 R$_E$ | X=-18.5 R$_E$ | X=-17.5 R$_E$ | X=-16.5 R$_E$ | X=-15.5 R$_E$ | X=-14.5 R$_E$ |

j$_y$ Fit

j$_y$ Goal

1.5 keV

5 keV

15 keV

j$_y$, nA/m^2

Z, R$_E$
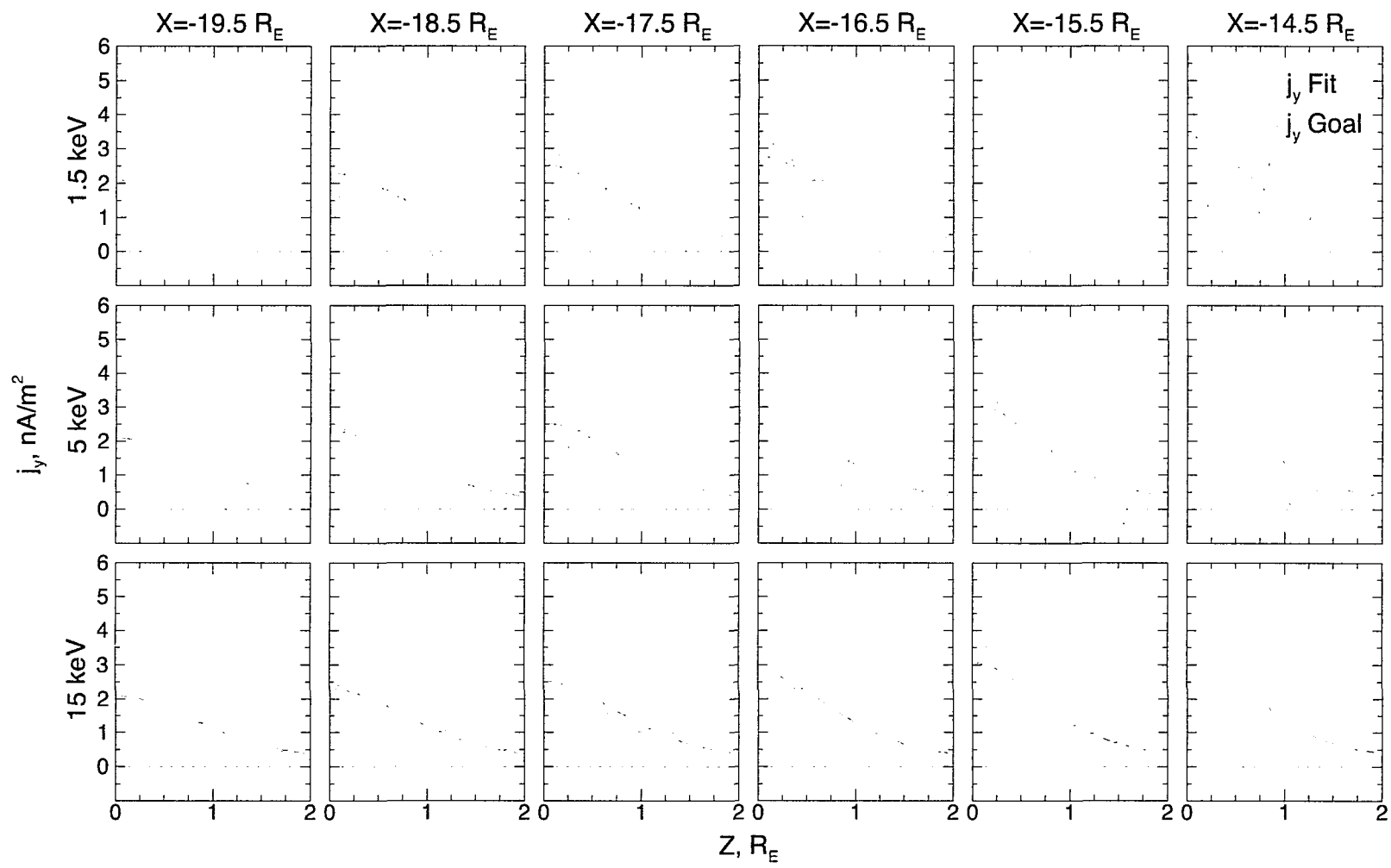
Figure 4.9: Thick model current sheet, fit and goal
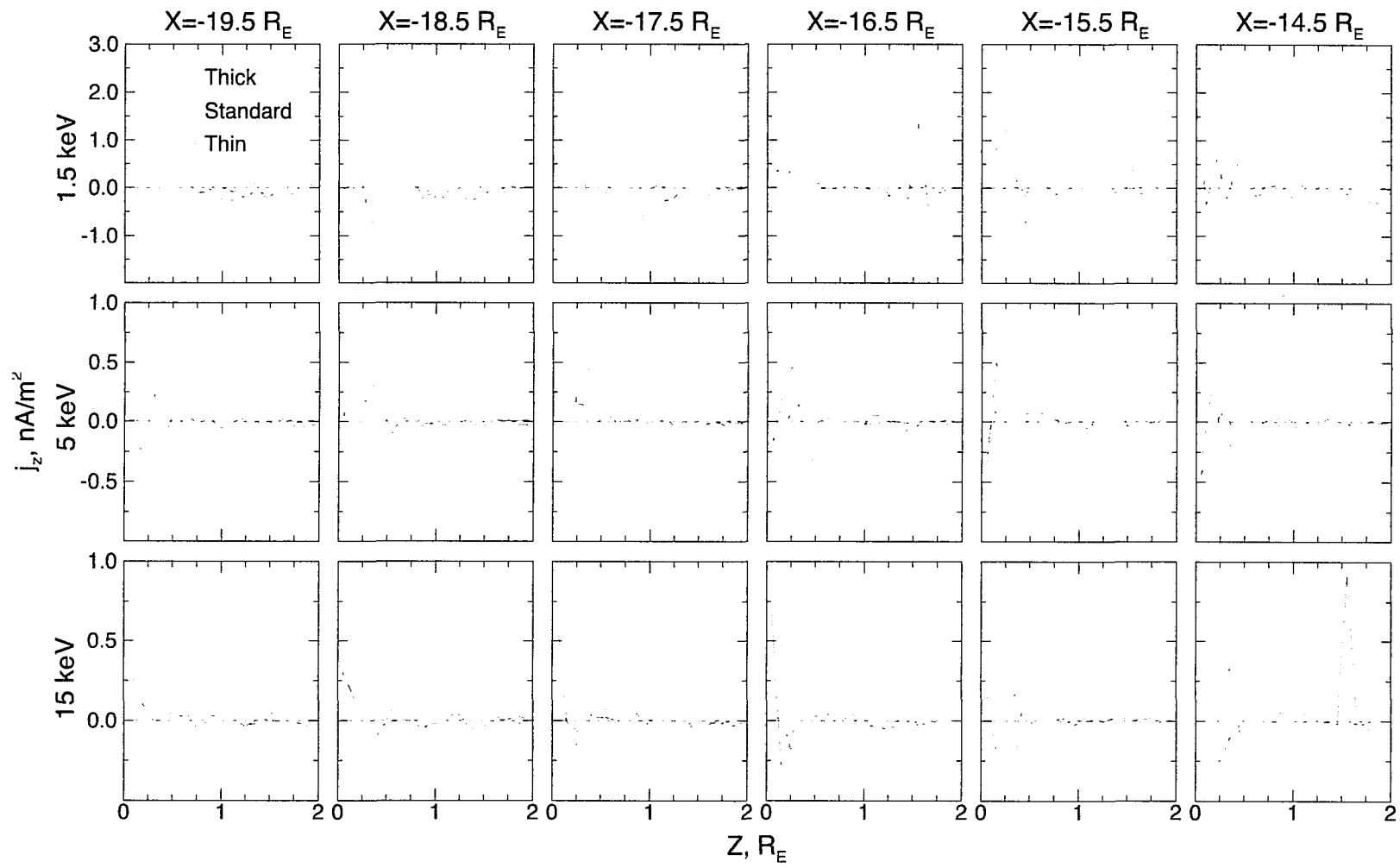
Figure 4.10: Current density j_z [nA/m^2] for all cases.

Table 4.1: Groups selected to make final goal j_y, W=1.5 keV

	X=-19.5	X=-18.5	X=-17.5	X=-16.5	X=-15.5	X=-14.5
Z=2/FA	NSK				K	K
Z=1.5	S		N	N	N	N
Z=1.0					N	NSK
Z=0.5		SK			SK	SK
Z=0.0		SK		N	SK	NS

Key: Thin (N), Standard (S), and Thick (K), Field Aligned (FA)

Table 4.2: Groups selected to make final goal j_y, W= 5.0 keV

	X=-19.5	X=-18.5	X=-17.5	X=-16.5	X=-15.5	X=-14.5
Z=2/FA	SK		N		N	
Z=1.5			S		NS	NS
Z=1.0	N		N		NS	NS
Z=0.5			K		K	
Z=0.0			NK		SK	

Table 4.3: Groups selected to make final goal j_y, W= 15.0 keV

	X=-19.5	X=-18.5	X=-17.5	X=-16.5	X=-15.5	X=-14.5
Z=2/FA	N	S			NSK	
Z=1.5			S	N		NK
Z=1.0			K	N		K
Z=0.5	K	K	SK			
Z=0.0	S	K			N	S

larger version of Figure 4.9. The final current density obtained by combining the groups, as shown by the solid line in Figure 4.5f, is much closer to the required self-consistent current distribution than is $j_y(x, z)$ for any individual group. Only these five groups were retained in the final fit. The thick/5keV groups selected are also indicated in Table 4.3. The fit is significantly poorer, at a 95% confidence level, if any one of these five groups is omitted.

<u>Sample cases</u>

The final $j_y(x, z)$ fits for the thin, standard, and thick models at 1.5, 5, and 15 keV starting energies are the dashed lines in Figures 4.7, 4.8, and 4.9 respectively. The solid lines are $\mathbf{j} = (1/\mu_o)\nabla\times\mathbf{B}_{model}$. These plots show that the $j_y(x, z)$ which is needed to generate $\mathbf{B}$ is largest at $z = 0$ in each x-box, and drops monotonically as z increases to $2 R_E$. Larger currents also are needed in x-boxes closer to Earth. All of the generated current sheets exhibit shortfalls in total current in the further x-boxes and for $|z| > 1$ R_E. The groups that were selected to make the final goal current sheets are given in tables 4.1, 4.2, and 4.3. Groups that were selected are indicated by a letter in the table cell corresponding to the injection location where (N) indicates the thin model, (S) the standard model, and (K) the thick model. The (FA) designation indicates that ions were started $z = 2 R_E$ at an x location along a field line that would intersect the x box location at $z = 0 R_E$. These tables show that each of the 9 cases required at least one trapped ($z = 0 R_E$), one central mirroring ($z = 0.5, 1.0, $ or $1.5 R_E$) group, and one outer mirroring ($z = 2 R_E$) group.

Figures 4.6 and 4.10 are the j_x and j_z current densities for all the cases studied. Although they are not used in the fitting procedure, the results are important for any discussion of force balance and continuity. These topics are left to the next chapter. It can be noted now though that these current density components all give results that track in magnitude
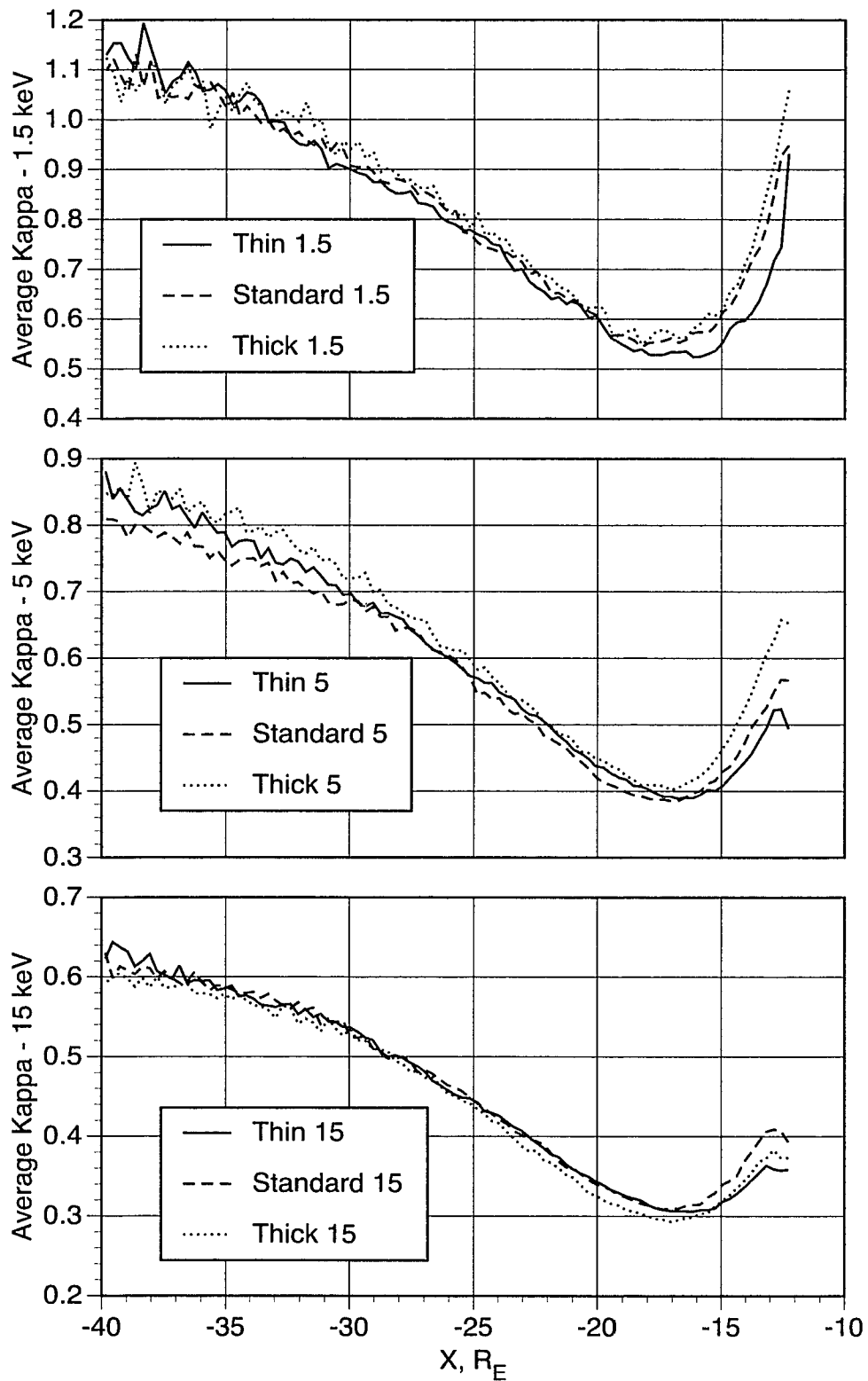
Figure 4.11: Average kappa for each of the model current sheets.

and general shape within their respective starting energy groups. This is not unexpected since the kappa values, which are proportional to the energy, are close within each group.

An individual particle in the tail is accelerated as it drifts Earthward. Acceleration tends to increase ρ_{zo} and reduce κ for the particle. As a particle reaches the more dipolar field lines of the inner tail the radius of curvature of the magnetic field increases which in turn increases κ. These two competing effects, when combined with other variations in B_{zo} and R_c, lead to a minimum κ somewhere in the midtail region. As inferred by the T89 model, the minimum κ of the principal current-carrying ions usually appears to be located near geocentric solar magnetospheric $x = -20$ R_E in the quiet time current sheet. This middle tail region thins during substorm growth phase and often becomes thinner shortly after substorm onset. Under extreme circumstances, the κ of even thermal electrons may occasionally decrease to unity.

Figure 4.11 shows the average κ as a function of x for each of the nine cases run. All cases have a minimum around $x = -17$ R_E which was seen in Figure 2.8 where the model κ was calculated. These minima are all close to or lower than the $\kappa = 0.52$ resonance ranging from 0.3 for the 15 keV starting energy cases to about 0.4 for the 5 keV starting energy particles and up to the resonance region for the 1.5 keV cases. All three energy groups have the same 50% drop off in kappa from the outer tail to the minimum. This is slightly more rapid than the 40% drop of Figure 2.8 where constant 1keV energy ions were assumed.

Since the ion energies change as particles drift in the uniform $E_y = 0.3$ mV/m or 1.9 kV/R_E field imposed on the magnetotail models, the more rapid drop in κ can be attributed more to the ions increasing in energy as they drift in the y direction. At $x = -40$ R_E the

low energy starting cases are around 0.72 keV and increase to an average of 1.6 keV at the minimum. The 5 keV starting energy cases are about 2.1 keV at $x = -40$ R_E and increase to 6.5 keV at the minimum. The 15 keV starting energy cases are about 7 keV at $x = -40$ R_E and increase to 17.5 keV at the minimum. This means that the ions do not travel more than a few Earth radii in the y direction in the midtail region.

Current Distributions

The dominant j_y current distributions seen in Figures 4.7-4.9 can be understood by referring to the orbit types shown in Figures 4.1-4.3. For example, an ion following the figure 8 pattern in Figure 4.3c moves in the negative y direction each time it crosses $z = 0$ and in the positive y direction at the tops and bottoms of the figure 8 pattern. The dividing point at which v_y and j_y are zero is near $z_o = mv/[qB_x(z_o)]$ [*Kaufmann and Lu*, 1993]. Many figure 8 orbits appear in a group of particles that starts with an isotropic distribution at $z = 0$. Most particles remain trapped for only a few current sheet interactions, so the figure 8 orbit pattern is dominant only near the starting field line. Groups in the left hand column of Figure 4.4 show the characteristic negative j_y at $z = 0$ and positive j_y beyond z_o, which is near or below 1/2 R_E for the 5 keV protons in this $-20 < x < -14$ R_E region of interest. The above current pattern is dominant in the starting and adjacent x boxes.

The right hand column of plots in Figure 4.4 is labeled differently from the other columns. These ions started at $z = 2$ R_E on field lines that reached the equator at the indicated $x = -14.5$ to -19.5 R_E. It is clear that no ions that start this far from $z = 0$ can initially be trapped inside the principal current sheet. Owing to the mirror effect, all these ions have relatively small pitch angles when they first approach the neutral sheet. Such ions with energies of 5 keV in the region of interest usually were reflected somewhat like the ions at $x = -13$ and -15 R_E in Figures 4.1a and b, and at -29 and -32 R_E in Figure 4.2. These ions

carry strong positive j_y in a thin sheet at $|z| < z_o$. The right column in Figure 4.4 shows the most intense thin current distribution peaked near $z = 0$ near the starting field line. If the ions continue to follow such orbits, they tend to drift substantially between current sheet interactions, so the current pattern is often not seen in an x box several earth radii away.

Trapped ions that mirror at $z = 1.5\ R_E$, for example, tend to carry positive current near $z = 1.5\ R_E$ and negative current one or two gyroradii closer to the neutral sheet, near $z = 1.0\ R_E$. A substantial number of such trapped ions are found in a group that is started isotropically at $z = 1.5\ R_E$. A number of the panels in the central 3 columns in Figure 4.4 exhibit positive j_y near the starting $|z|$ and negative j_y closer to $z = 0$. The j_y patterns tend to be complex, but very reproducible in all details, for groups of particles that start with isotropic distributions at $z = 0.5, 1.0$, and $1.5\ R_E$. Trapped ions with mirror points inside the current sheet are needed to broaden the current carried by 5 keV protons so they can produce a sheet with a thickness of $1\ R_E$ or larger, as is often observed. The first and last columns in Figure 4.4 show that it would not be possible to broaden the current sheet beyond approximately $z = \pm 0.5\ R_E$ with just reflected and figure 8 type 5 keV ions. We therefore conclude that ions that mirror well away from the neutral sheet, ions that mirror in the current sheet, and figure 8 ions all are needed to self-consistently generate our standard model tail using 5 keV protons.

Uniqueness

One feature that the SCOT solutions have in common with electrostatic BGK solutions is that neither method generates a unique distribution function. Several properties of the electron and ion distributions can be picked arbitrarily when generating a self-consistent current sheet. For example, the original Harris model and most of its later modifications assume a uniform ion cross-tail drift velocity v_{iy} and a uniform electron cross-tail drift

velocity v_{ey} throughout the current sheet. There is much less freedom in the more complex 2D current sheet because the same ions and electrons must carry the preselected current distribution as they drift and are accelerated throughout the region of interest. Nevertheless, the SCOT technique does not provide a unique plasma sheet.

As noted earlier, the SCOT procedure was constrained by introducing satellite data. Both the 1-D and 2-D models used a preselected magnetic field. This choice is based on the assumption that the magnetic field has been globally modeled more accurately than any other magnetotail property. Electron and ion starting energies and the cross-tail electric field also are preselected based on observations. Solutions have been generated for a range of energies and electric fields that spans the range observed in the middle magnetotail. Although current sheets can be generated using energies above and below the average energies observed, such unrealistic choices require particle densities that disagree with observations.

Once the above basic selections have been made the overall structure of the final distribution functions is reasonably well defined. There is, naturally, no need to select the specific 30 starting positions that are shown in Figure 4.4. However, it is necessary to include some groups of particles that mirror far from $z = 0$ and some groups that are trapped within the current sheet if we are to generate a sheet with a characteristic thickness of 1 R_E. Groups with starting points at $z = 2$ R_E are dominated by particles that mirror far from the current sheet, and carry their principal j_y in a very narrow sheet near $z = 0$. Much poorer least squares fits are obtained if either of these orbit types is not included. All groups that are retained in the final model must improve the fit with a 95% confidence level. This is to be sure that a group with similar properties is essential. Better fits can be obtained by just

adding more and more monoenergetically starting groups or to use particles started with maxwellian distributions. However, the goal here is to understand the basic requirements that are necessary to generate a realistic magnetotail current sheet rather than to produce the smoothest possible model.

Chapter V

FLUID PARAMETERS AND FORCES

5.1 Introduction

This chapter presents the parameters that are most easily compared with published satellite measurements for the $-20 < x < -14$ R_E region as well as an examination of whether the SCOT method can achieve force balance and energy conservation in the model region. Sample results from nine runs of the SCOT technique using the thin, standard, and thick magnetotail models and 1.5, 5, and 15 keV starting energies are shown. The standard 5 keV set is used as a general representative case throughout this chapter to provide more detail of some parameters and forces.

5.2 Fluid Parameters

The plasma number density

The solid lines in Figure 5.1 are contours of constant $n_i(x, z)$ obtained by integrating the distribution functions of the final combination of particle groups. The dashed gray lines are magnetic field lines of the standard model. As discussed in Chapter 3, the density is fit to a polynomial for subsequent use in electron current calculations, an example of which is given by Figure 5.2. The density is for the most part constant along field lines near the neutral sheet within $|z| < 0.75$ R_E so the resulting polynomial readily achieves the same curvature as the more jagged actual data. Any problems near the neutral sheet attributable to a poor fit of $n_i(x, z)$ directly affect the electron current. However, since the electron current contributes a fraction to the final current sheet groups, little impact is seen.
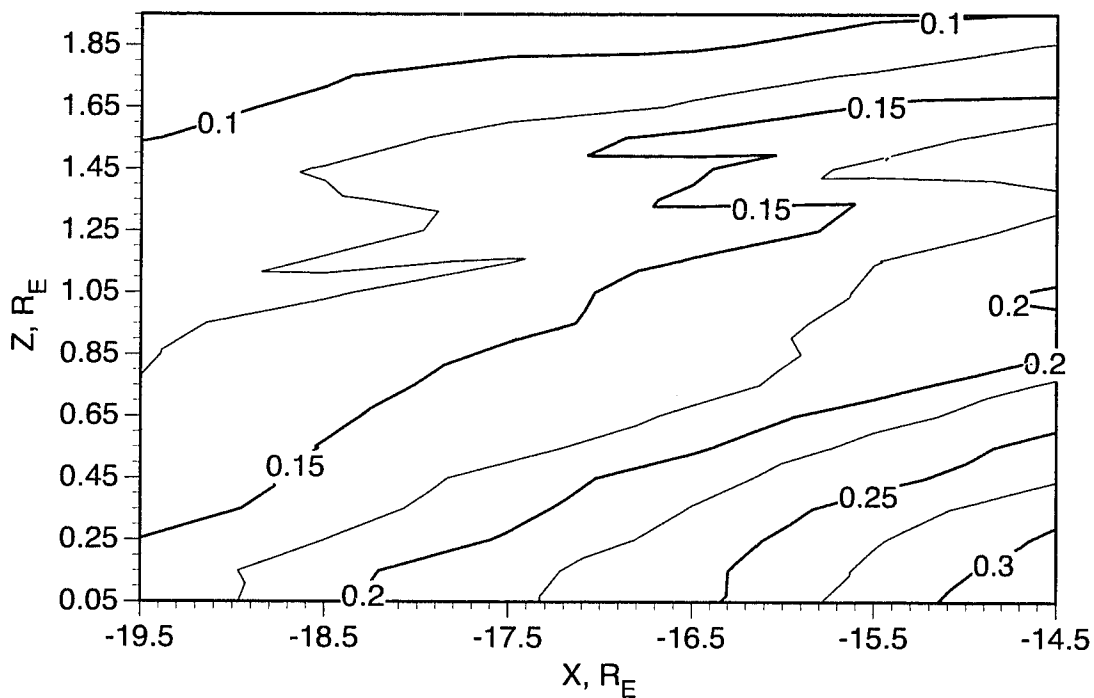
Figure 5.1: Number density n(x,z) [cm⁻³] of the standard model/5 keV current sheet with the field lines overlaid (in gray).
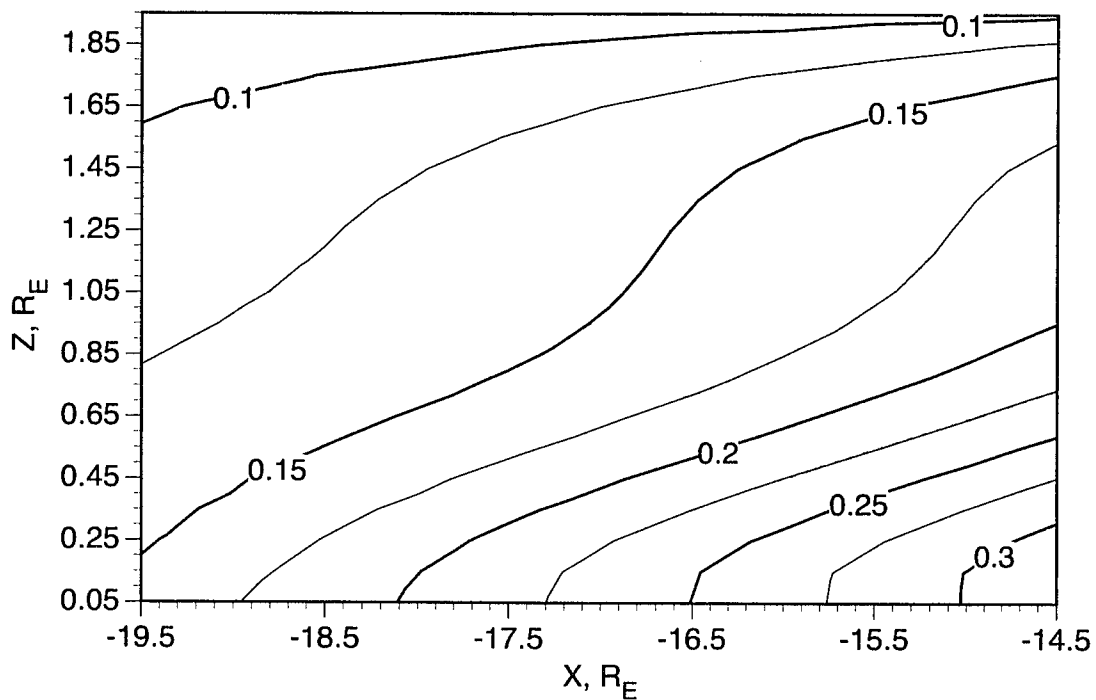
Figure 5.2: Polynomial fit of the number density n(x,z) [cm⁻³] of the standard model/5 keV current sheet with the field lines overlaid (in gray).

Baumjohann et al. [1989] binned AMPTE/IRM data according to satellite location and the AE index. The two spatial bins that are most relevant to our model of the current sheet were together referred to as the inner CPS. The region closest to the neutral sheet was defined by $B_{xy} < 7.5$ nT, where $B_{xy}^2 = B_x^2 + B_y^2$, and will be referred to as the inner current sheet. The portion of the inner CPS farther from $z = 0$ is defined by $7.5 < B_{xy} < 15$ nT, and will be referred to as the outer current sheet. The AMPTE/IRM satellite did not make measurements at the statistically averaged location of the neutral sheet [*Fairfield*, 1980] in our region of interest during the 1986 magnetotail data collection periods. However, many neutral sheet crossings were observed when the neutral sheet was displaced from this average location. The entire plasma sheet is known to undergo substantial motion in the z direction. No obvious dependence of plasma parameters on the neutral sheet displacement from its average location was noted in a brief comparison with 1985 data, which had better orbital coverage. The inner CPS data show an average density of about 0.3 cm^{-3} with little z dependence.

Kistler et al. [1993] sorted AMPTE/IRM data taken at radial distances beyond 15 R_E according to substorm phase and to distance from the neutral sheet. This study used a more complex method to estimate distance from the neutral sheet. The plasma beta, or ratio of particle to magnetic field pressures was determined for each data point. The highest β is expected near $z = 0$, and the lowest β in the lobes. Points were binned into 3 equal groups, labeled inner, middle, and outer plasma sheet. With respect to sorting by substorm phase, it is most reasonable to compare our quiet time model to data taken before substorm onset. Densities were about 0.4 cm^{-3} in the inner and middle third, and about 0.2 cm^{-3} in the outer third of the plasma sheet [*Kistler*, private communication].
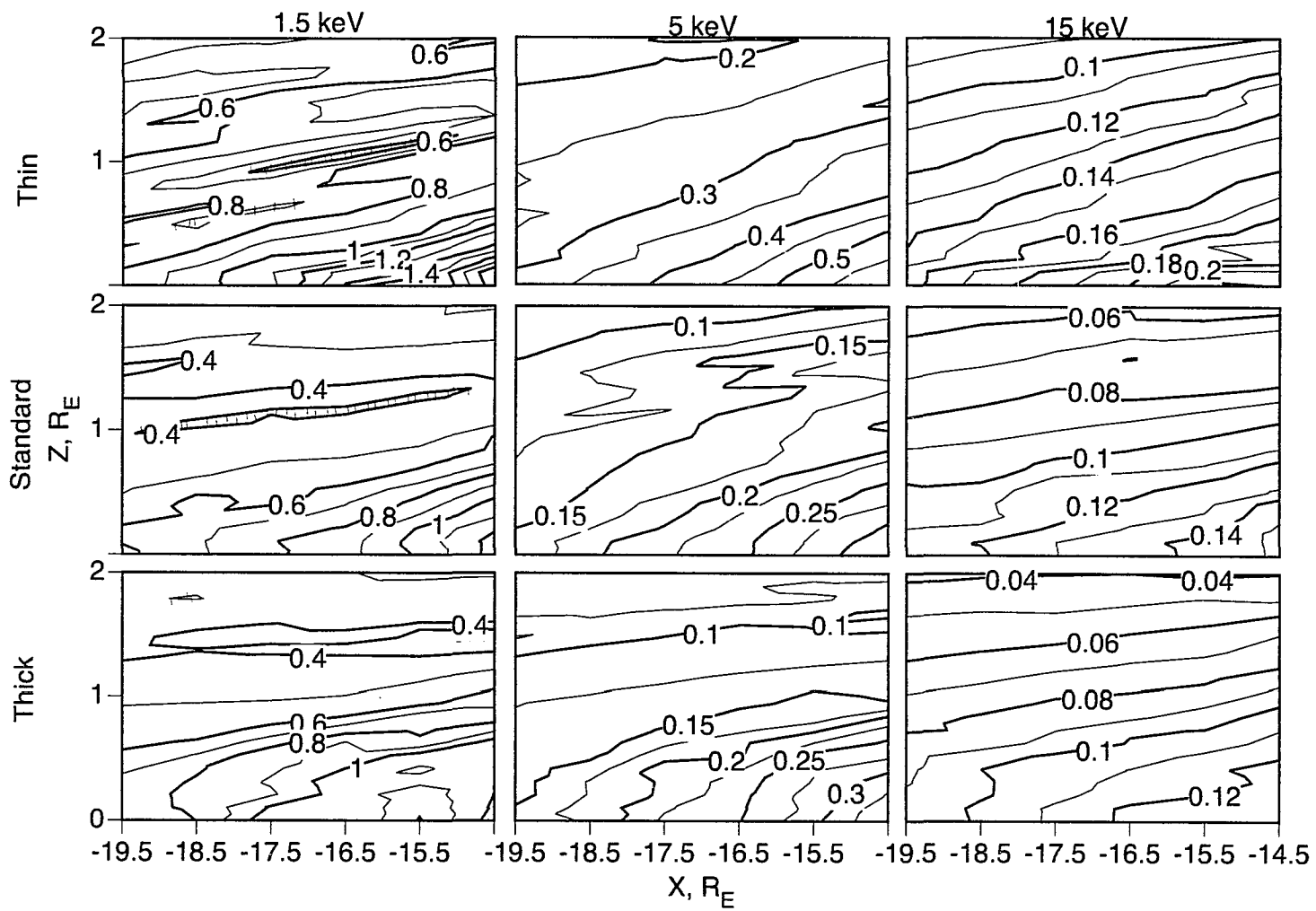
Figure 5.3: Final number density n(x,z) [cm^{-3}] for all current sheets.

Huang and Frank [1994] sorted ISEE 1 data according to distance from the *Gosling et al.* [1986] average neutral sheet location. The satellite orbit provided good coverage of this average location. The average observed density was approximately 0.25 cm^{-3} during both quiet and disturbed times, with little consistent z dependence.

The above measurements involved statistical averages over a number of orbits. An absolute distance scale was not determined in these statistical treatments. For example, it usually was not known when the satellite was 0.5 R_E, 1 R_E, 1.5 R_E, or any other specific distance from the center of the neutral sheet. Only a few analyses have been carried out which determined the instantaneous structure of the current sheet during quiet conditions in our region of interest. These studies measured the current sheet structure using both ISEE 1 and 2 spacecraft. Of these, we could find only two that also described plasma density and temperature variations within the current sheet. *McComas et al.* [1986] studied 3 crossings that were associated with the passage of a strong interplanetary shock front. It was concluded that the plasma density, temperature, and pressure changes were consistent with approximate plasma plus magnetic field pressure balance. However, temporal changes in the current sheet structure and orientation were so large during this orbit that it was not possible to determine a consistent density or temperature profile. *Zhou et al.* [1995] found two periods during which a number of current sheet crossings took place with the spacecraft well positioned to measure density and temperature gradients. They concluded that both density and temperature decrease by a factor of two as the spacecraft moved 1.5 current sheet thickness scale lengths from $z = 0$. The average half thicknesses on this orbit were 2 R_E when the IMF pointed northward and 0.5 R_E when the IMF pointed southward.

The SCOT model number densities nearest the neutral sheet (Figure 5.3) are close

to or slightly below the observed values. The dropoff of $n(x, z)$ with increasing z is similar to that measured by *Zhou et al.* [1995] but more rapid than the dropoff suggested by the statistical studies. The model density depends on the starting ion energies used. Densities for the standard model were 3 to 4 times larger when 1.5 keV protons were used instead of 5 keV protons (column 1 of Figure 5.3), and about half as large when 15 keV protons were used (column 3 of Figure 5.3). Since low energy particles carry little current for a given density, filling in the low energy portion of the model distribution function to make it more realistic will only slightly increase the plasma density that is needed to carry the necessary j_y. The density in the thick model with 5 keV protons was similar to that of the standard 5 keV model, while densities near $z = 0$ were about 50% larger in the thin-5 keV model. The earlier self-consistent 1D model with 3 keV protons [*Kaufmann and Lu*, 1993] required particle densities as high as the 2D model with 1.5 keV protons.

Figure 5.1 shows that the model density is nearly constant along magnetic field lines near $z = 0$. However, field lines cross several contours of constant density in the $1 < z < 1.5$ R_E region. As described previously, a variation of density along a field line required the introduction of a parallel electric field if isotropic guiding center electrons were to maintain charge neutrality with the non-guiding-center ions. The density changes seen along field lines at $z < 1$ R_E and at $z > 1.5$ R_E in Figure 5.1 were typical of the changes seen throughout the region of interest for the other 8 cases studied. No other case showed as large a field-aligned density drop as that seen at $1 < z < 1.5$ R_E in Figure 5.1.

Density variations are important because non-guiding-center ions and guiding center electrons generally are not distributed in the same manner along a magnetic field line. The electron density is constant along a field line if the equatorial pitch angle distribution is isotropic. This tendency for different variations of ion and electron densities along a field

line results in the generation of a parallel electric field to maintain charge neutrality. Note that the largest ion density variations along field lines in the SCOT results are found at $|z| > 1$ R_E, and are caused by density variations in the x direction. Both AMPTE/IRM and ISEE 1 data showed density increasing closer to the Earth.

Electron considerations

A number of assumptions were made to calculate the current carried by Maxwellian electrons. Most of these assumptions have already been described because they were used in the 1D calculations [*Kaufmann and Lu*, 1993]. A polynomial fit was made to both $n_i(x, z)$ and the ion temperature $T_i(x, z)$ for each group traced. The electron number density $n_e(x, z)$ was set equal to the polynomial fit to $n_i(x, z)$ so the resulting plasma would be approximately neutral. Since n_e would be constant along field lines if electrons were isotropic at the equator, a first order parallel electric field was added to the zeroth order uniform E_y. The Boltzmann relation

$$n_e(x, z) = n_e(x_o, z_o)\exp[-q_e\phi/T_e] \qquad (5.1)$$

was used to calculate the electric potential difference ϕ between each (x, z) box and a reference point (x_o, z_o) on the same field line. The electron temperature T_e in keV was taken to be 1/7 of a polynomial fit to the group ion temperature [*Baumjohann et al.*, 1989]. Since electrons are much less energetic than ions, electrons were influenced much more strongly by the parallel electric field than were ions. Equation (1) only gives the distribution of ϕ along a field line, so only determines the parallel electric field. Since $E_{||}$ is distributed differently along adjacent field lines, some $E_\perp$ in the x-z plane must also be present. We used a variational approach to determine this $E_\perp$. It was assumed that $E_\perp$ will develop so that the energy density $\varepsilon_o E^2$ is minimized. This assumption completes the definition of **E**. The total potential drop between $z = 0$ and $z = 2$ R_E was only about 200 V or less. This potential difference is similar to the values obtained in our previous 1D model. To be self-consistent

ion orbits must be traced again in the magnetic field with this added $E_\parallel$. As was found in the 1D case, a 200 V potential drop had little effect on 5 keV protons.

The κ for such a group of electrons is 11 times the κ for the associated proton group, so all electron motion is well approximated by the guiding center assumptions in the models studied here. The electron cross-field drift was calculated from

$$\mathbf{j}_{e\perp} = \frac{\mathbf{B}}{B^2} \times \left[\nabla P_{e\perp} + \frac{P_{e\parallel} - P_{e\perp}}{B^2}(\mathbf{B} \cdot \nabla)\mathbf{B} \right] + n_e q_e \frac{\mathbf{E} \times \mathbf{B}}{B^2} \tag{5.2}$$

based on the polynomial fits to $n_e(x, z)$ and the isotropic $P_e = n_e T_e(x, z)$. This procedure yielded the electron $j_y(x, z)$ for each group, as shown in the middle column of Figure 4.5. The addition of electron and ion currents gave the total $j_y(x, z)$ for each group, as shown in the right column of Figure 4.5.

The above procedure, which assumes isotropy and the presence of $E_\parallel$, is not the only one that could be used to include electrons. Instead, it is possible to produce charge neutrality along field lines with $E_\parallel = 0$ by adjusting the angular distribution of electrons at the equator. Substantial electron anisotropies involving $T_\parallel > T_\perp$ have been observed in the central plasma sheet [*Hada, et al.*, 1981; *Paterson et al.*, 1995], though most observations have reported approximate isotropy at $z = 0$. As an example, a biMaxwellian distribution at the equator yields a density variation along a field line of

$$n(B) = \frac{n_o T_\parallel}{T_\perp + (T_\parallel - T_\perp)(B_o/B)} \exp[-q\phi/T_\parallel] \tag{5.3}$$

where n_o and B_o are the particle density and |B| at the equator. When $E_\parallel = 0$ or $\phi = 0$ everywhere, the density varies by a factor of $T_\parallel/T_\perp$ as one moves from the equator to the ionosphere. Therefore, $T_\parallel/T_\perp = 2$ would produce a density at the edge of the current sheet that is nearly twice the density at the equator.
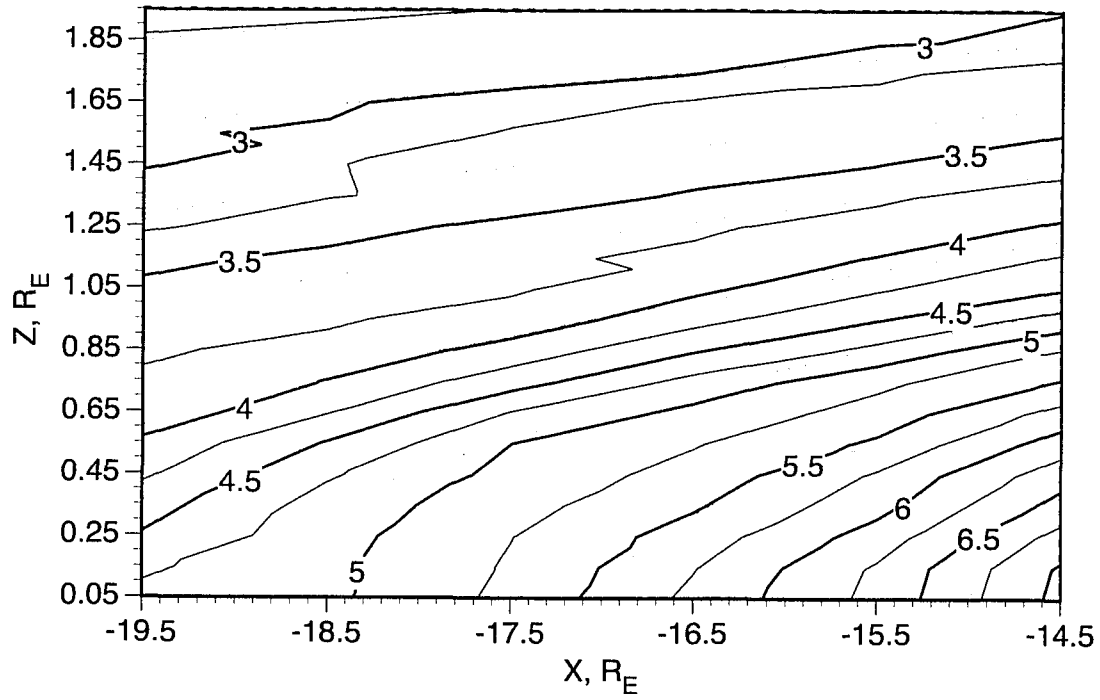
Figure 5.4: Temperature [keV] of the standard/5 keV model with fieldlines (gray lines).
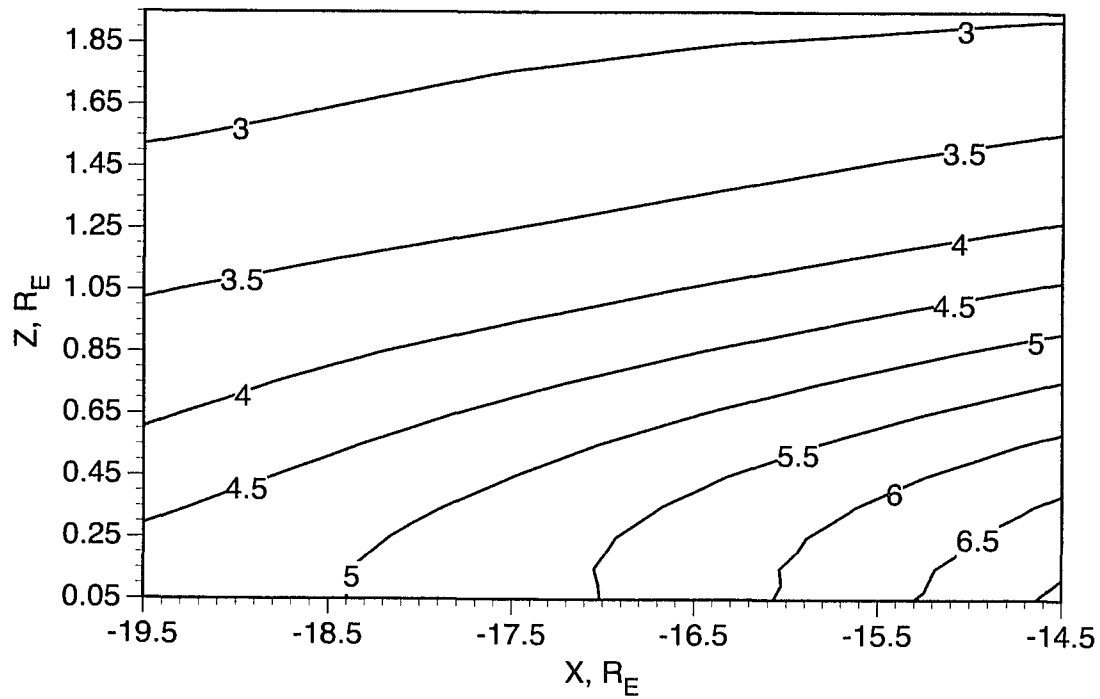
Figure 5.5: Polynomial fit of the standard/5 keV model temperature [keV] with fieldlines overlaid (dashed gray lines).
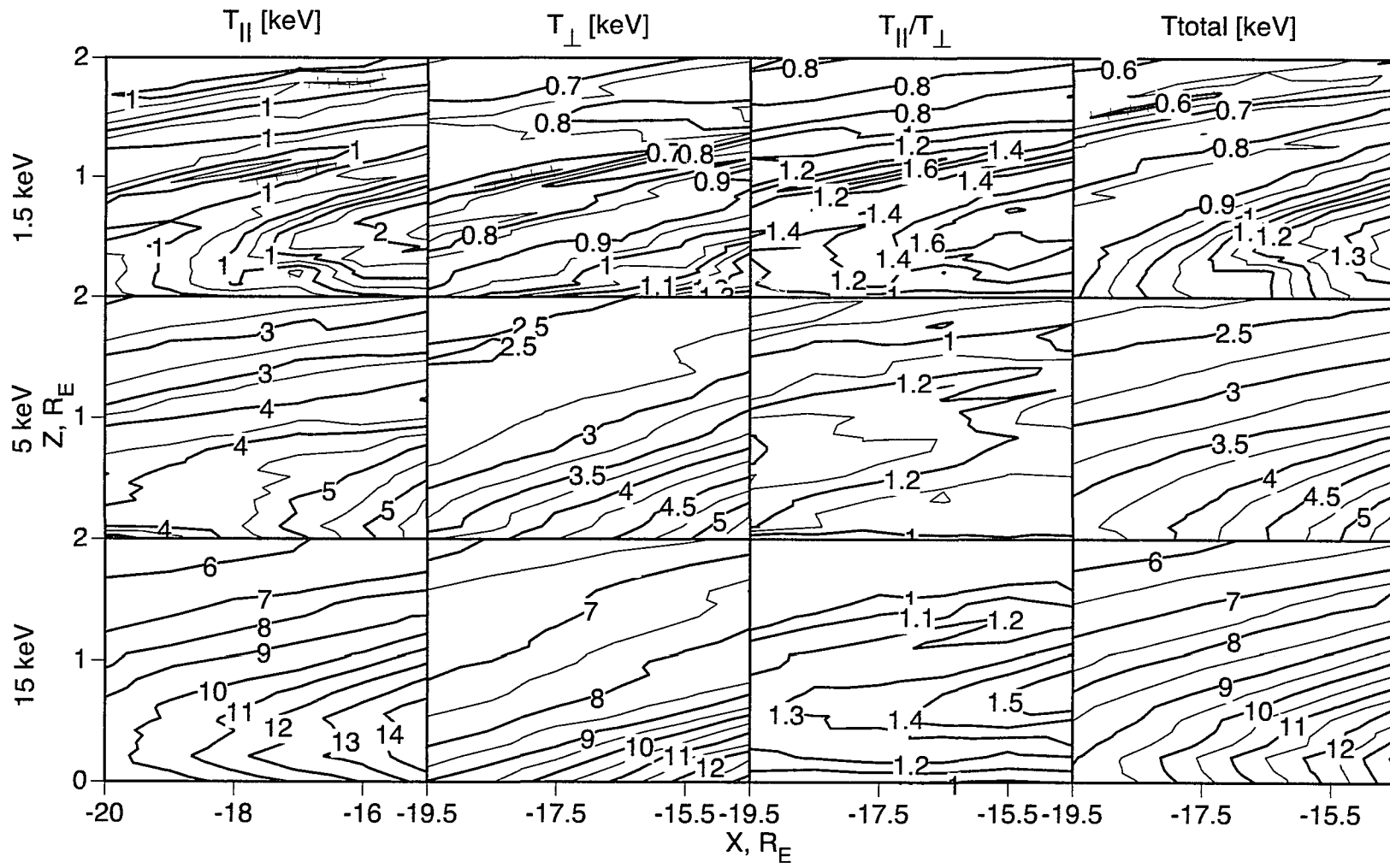
Figure 5.6: Thin Model temperature [keV].
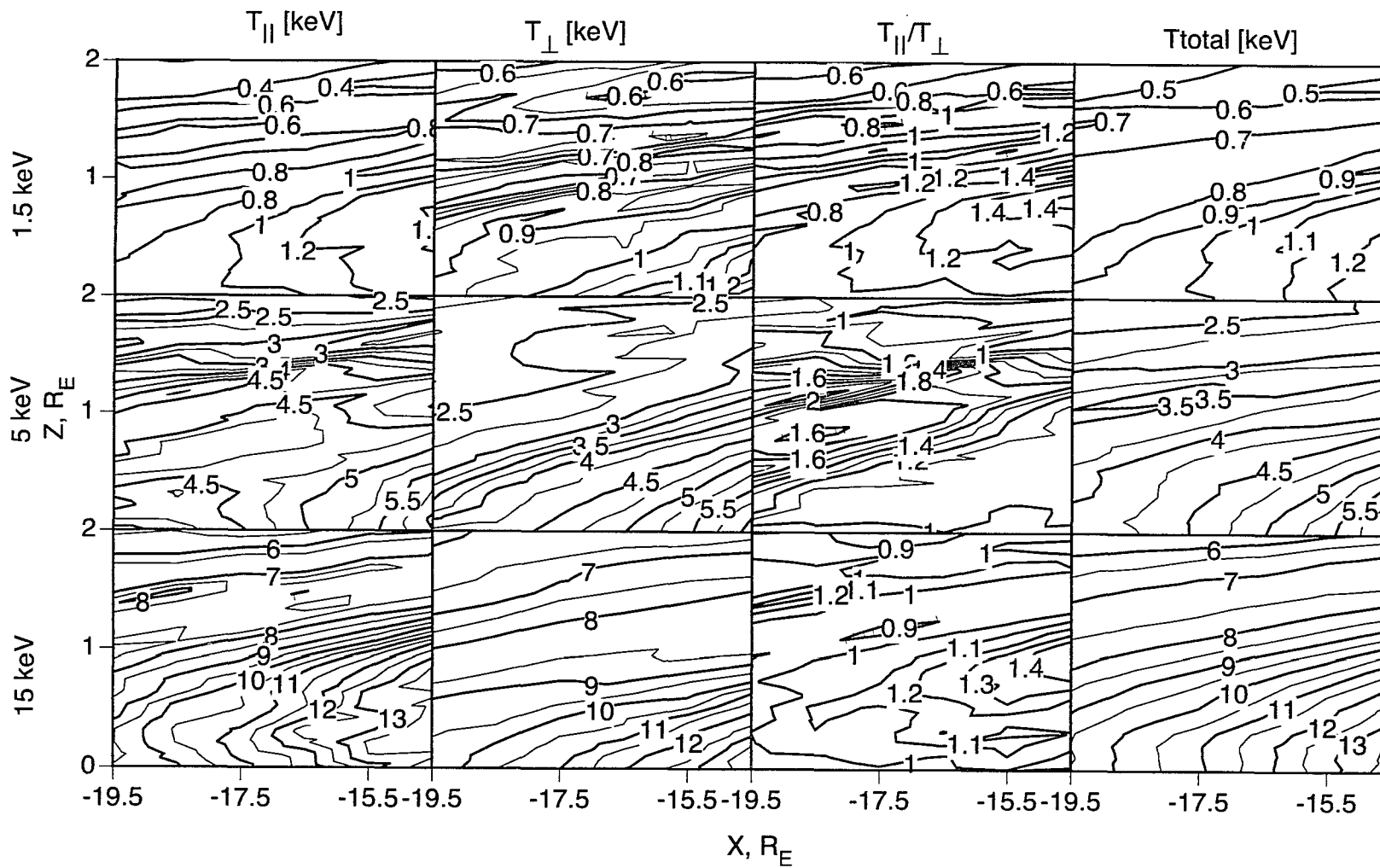
Figure 5.7: Standard model temperature [keV].
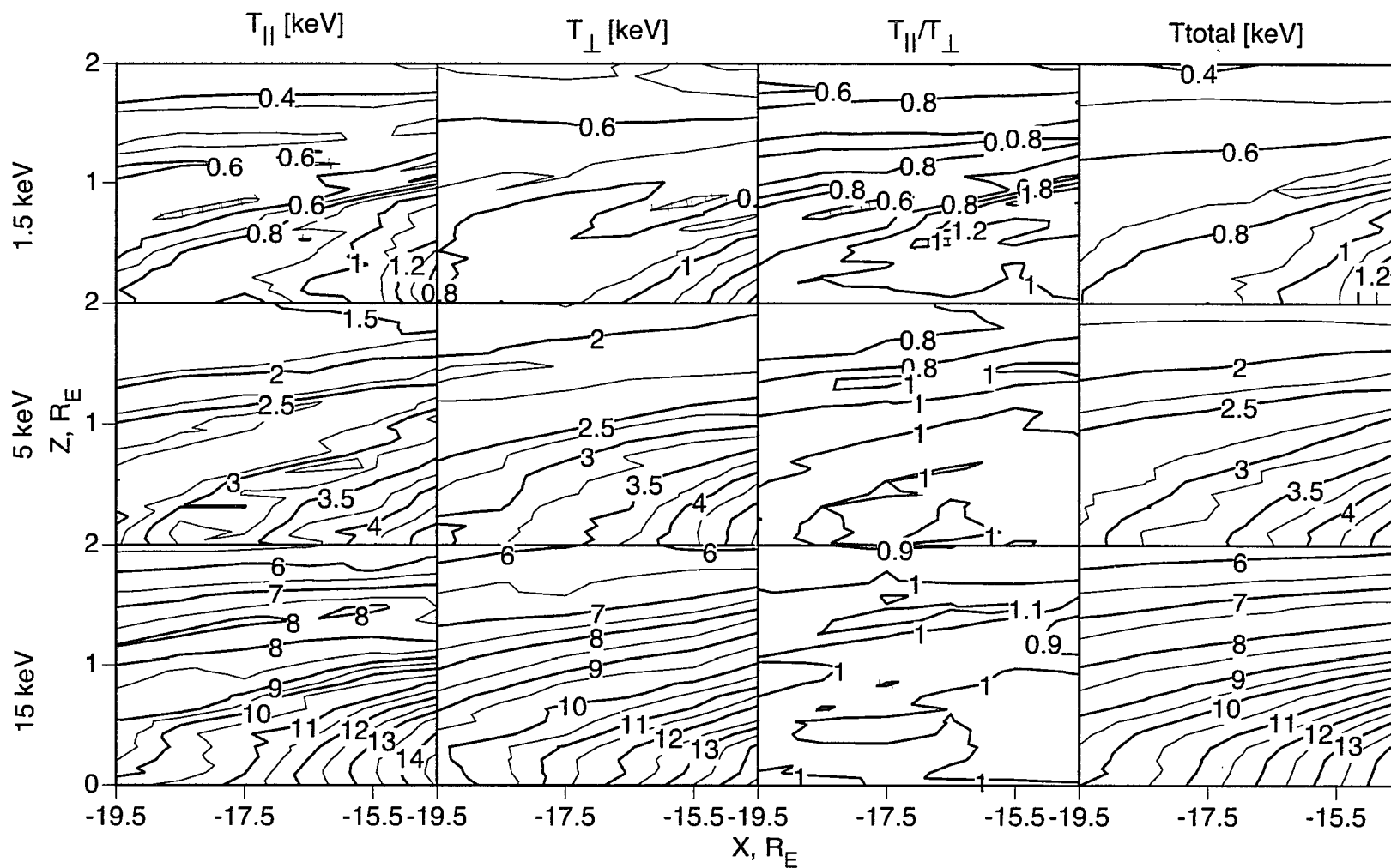
Figure 5.8: Thick model temperature [keV].
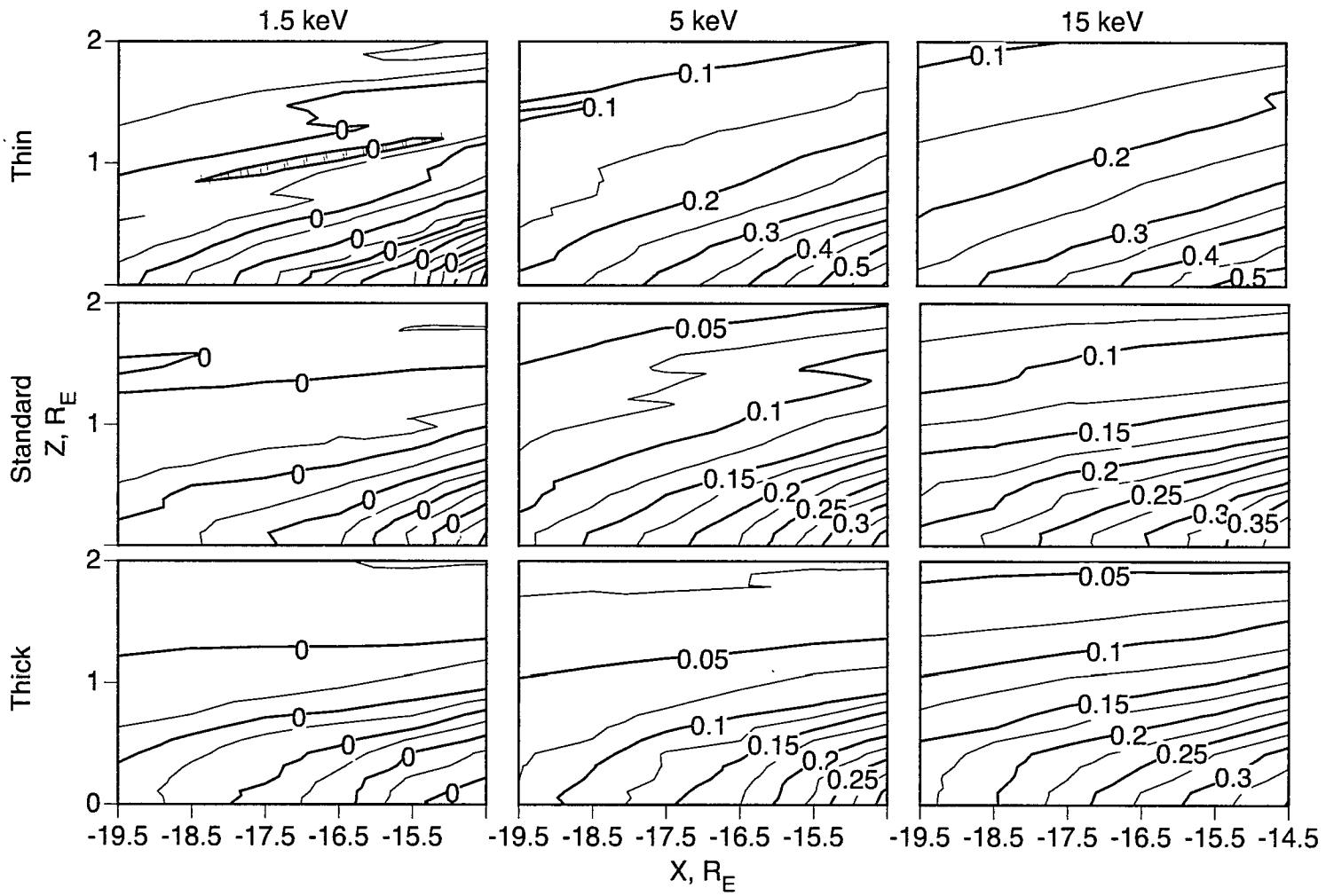
Figure 5.9: Pressure of the derived current sheets, [nPa]
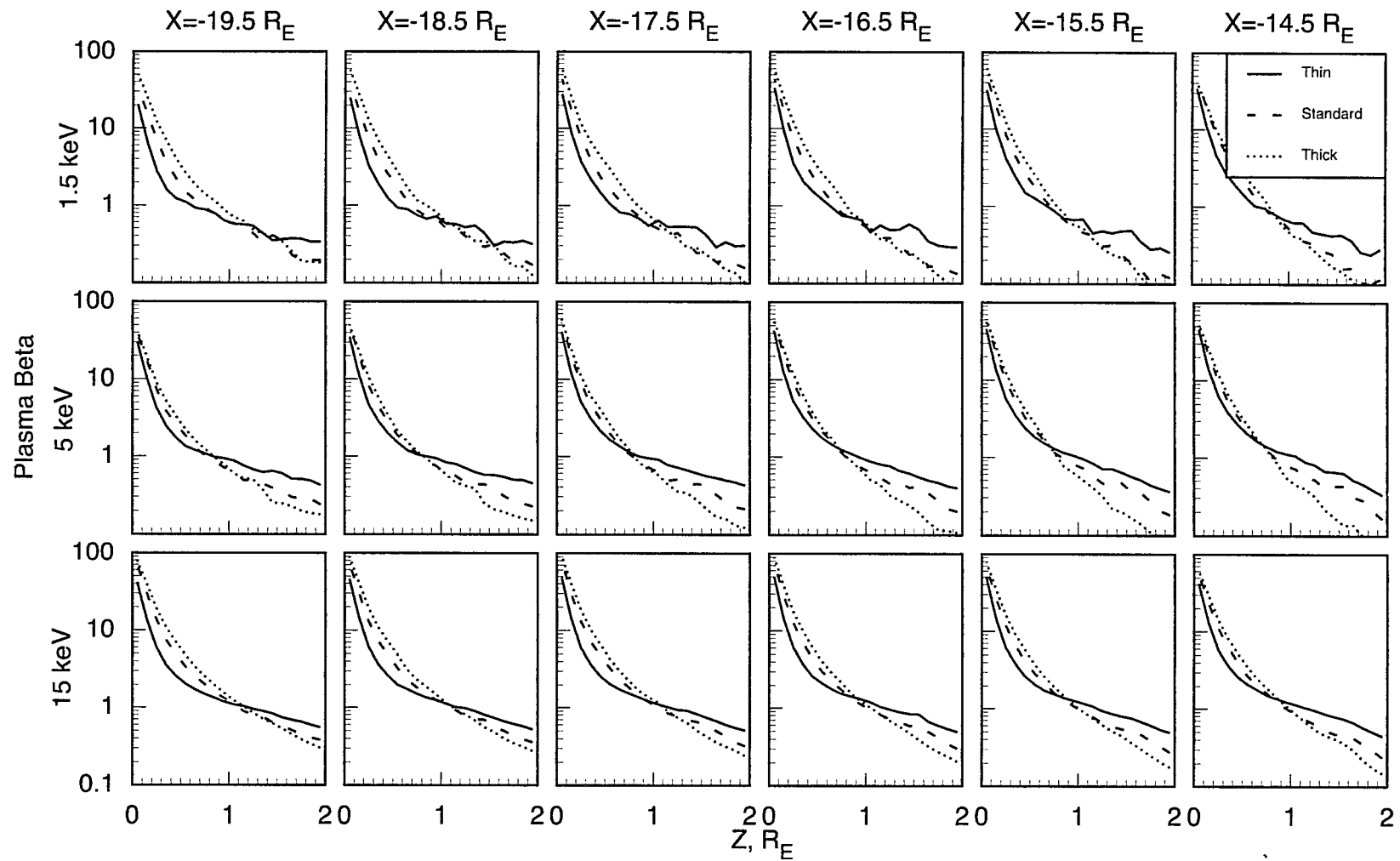
Figure 5.10: Plasma Beta of the derived current sheets.

An electron distribution with very abrupt pitch angle variations would be needed to

However, it is difficult to find the necessary equatorial angular distribution that is needed to

produce charge neutrality everywhere along a field line when an arbitrary ion density variation $n(B)$ is specified. maintain charge neutrality in this case if $E_{\parallel} = 0$. The method used

in the present analysis is much easier to implement and results in reasonable distribution

functions for all cases studied. Since electron cross-tail currents are small in sheets of the

thicknesses used here, this simple method should be adequate.

Temperatures

The first and second columns of Figures 5.6-5.8 show the average parallel and perpendicular temperatures. Column three shows the $T_{\parallel}/T_{\perp}$ ratio and column four the total

temperature. Unlike the earlier 1D application of the SCOT method [Lu, 1993] which had

a large anisotropy at the edge of the current sheet, the new 2D models are much more isotropic with a range of $1.0 < T_{\parallel}/T_{\perp} < 1.4$. Since strong ion streaming or large anisotropies

at the edge of the current sheet are not an observed feature, the 2D models more closely

resemble the actual magnetotail.

The standard 5 keV model most closely resembles the published observations for

the pre-substorm onset time period. However this says more about the actual thickness of

the midtail during the observation time rather than anything about the validity of the other

models and starting energies. These other models may be applicable at different phases of

a substorm. Specifically, *Baumjohann et al.* [1989] observed an average inner plasma sheet

temperature of 4 keV in our region of interest, with slightly lower values during quiet times.

Kistler [private communication, 1995] found temperatures dropping from 4 keV in the inner plasma sheet to 2 keV in the outer plasma sheet before substorms. *Zhou et al.* [1995]

found approximately a factor of two drop in temperature when moving 1.5 thickness scale

lengths from $z = 0$. The calculated $T = (T_{\perp 1} + T_{\perp 2} + T_{\parallel})/3$ averaged over the region of

interest drops from about 5.0 keV to about 2.75 keV, which is close to the observed tem-

perature decreases. Since the starting ion energy is one of the preselected parameters, the

absolute ion temperature in the model can easily be changed. As noted above, lower tem-

peratures will increase the required density, so a small reduction in starting energy would

slightly improve the agreement with both the calculated $n(x, z)$ and $T(x, z)$. Thus it

could be possible to select a set of particle groups to fit a specific observation.

Figure 5.9 is the model pressure, which is given by $p = nkT$. Both the standard and

thick cases exhibit similar magnitudes in their pressure profiles, in contrast the thin cases

are all higher than the other two sets of cases. Consequently the plasma β of the thin cases

is seen to drop more rapidly. Figure 5.10 shows the plasma beta or particle/field energy

density ratio. The observed β [*Baumjohann et al.*, 1989] dropped from approximately 20 in

the neutral sheet region to 3 in the outer current sheet, and 0.3 in the outer plasma sheet.

Results from all 9 of the cases studied here showed similar decreases with $\beta = 20$ to 100

at $z = 0$ and $\beta = 0.1$ to 0.5 at $z = 2 \, R_E$.

Bulk flow

The model ion bulk flow velocity is shown in Figure 5.11 and is given by

$$\mathbf{u}_i = (1/n) \int \mathbf{v} f_i(\mathbf{v}) d^3 v \quad . \tag{5.4}$$

Both the model and quiet time observations showed that the ion distribution functions are

nearly spherically symmetric. The $\mathbf{u}_i$ is produced by a small shift of several-keV ions. The

contours of constant $f_i(\mathbf{v})$ remain nearly spherical. However, these contours are displaced

slightly, relative to the thermal speed, in the bulk flow direction. Electrons drift slowly in

the negative y direction, so they make a small addition to the ion current.

Detailed examination of $f_i(\mathbf{r}, \mathbf{v})$ shows two features that result in a bulk flow. The principal cause of ion V_y is an asymmetry in the nearly monoenergetic spherical shell of ions in our model. Ions going east and west have the same energies, but there are more going east. This behavior is associated with the large eastward displacement of ions, especially near $z = 0$, that is evident in Figures 4.2 and 4.3. This net positive ion V_y produces most of the cross-tail current, with eastward electron drift causing the rest.

The nature of V_x shown in Figure 5.11a is substantially different. This component is primarily field aligned except very near $z = 0$, where $\mathbf{E} \times \mathbf{B}$ drift dominates. The model distribution function away from $z = 0$ shows that the entire spherical shell experiences a net shift in the positive V_x direction, so that ions moving Earthward are slightly more energetic than are those moving tailward. A less important angular asymmetry also is sometimes seen in the opposite direction, with a larger number of ions moving tailward than Earthward. This small angular asymmetry reduces the net Earthward V_x, particularly near $z = 1$ R_E in Figure 5.11a. A positive ion V_x is commonly seen in our region of interest in both AMPTE/ IRM [*Baumjohann et al.*, 1989] and ISEE 1 [*Huang and Frank*, 1994b] data.

In a 1D model, E_y is transformed to zero in the deHoffman Teller reference frame which moves Earthward at a speed E_y/B_{zo} based on B_z at $z = 0$. There is no reference frame in which E_y is zero everywhere in a 2D model. However, as seen in Figure 5.12, the nine cases examined trend like the deHoffman-Teller velocity but with lower magnitudes. The low energy particles do well with the thin model, differing from the E_y/B_{zo} speed by an average of 20 percent, but deviate by more than 30 percent in the thick model case. In contrast the 15 keV particles do better with the thick model with an average 15 percent devia-

tion and worse with the thin model with an average 30 percent deviation. The particles of the 5 keV models have the least difference in tracking the Earthward drift for all three models, although at about a 15 percent deficit from the E_y/B_{zo} speed. In all nine cases the correlation improves Earthward of x=-17 R_E. It can be concluded that E_y/B_{zo} produces a rough estimate of V_x dependent upon the dominant particle population of the specific 2D or 3D current sheet model.

Figure 5.14 shows that the average v_z is similar for all nine cases. The effect of the gradient and curvature drifts can be seen in Figure 5.13 which shows that the average v_y correlates with the starting energy.

The single particle orbits show the physical origin of the strong field-aligned drift. The effect is produced by ions that mirror within the current sheet. For example, the ion in Figure 4.1a moved approximately 5 R_E Earthward, primarily along **B** as it went from $x = -19\ R_E$, $z = 0.5\ R_E$ to a mirror point at $x = -14\ R_E$. The ion then moved only about 2.5 R_E tailward from the mirror point, primarily along **B**, until it returned to $z = 0.5\ R_E$. The net 2.5 R_E Earthward motion at $z > 0.5\ R_E$ contributes to a generally field-aligned bulk flow.

A small net drift toward $z = 0$ averaging about 20 km/s also is seen in the model V_z. This is primarily **E** × **B** drift. The model $E_y = 0.3$ mV/m electric field produces a 20 km/s drift toward $z = 0$ in a region with $B_x = 15$ nT. Electrons and ions **E** × **B** drift in the same direction, so these contributions to the current tend to cancel in the outer current sheet, where the guiding center approximations are valid.

Although it does not affect the SCOT analysis, which is based only on j_y, electrons were assumed to drift along field lines at the same speed as ions. This assumption was required to make $\nabla \cdot \mathbf{j} = 0$ for electrons, and also so there would be no Birkeland current.
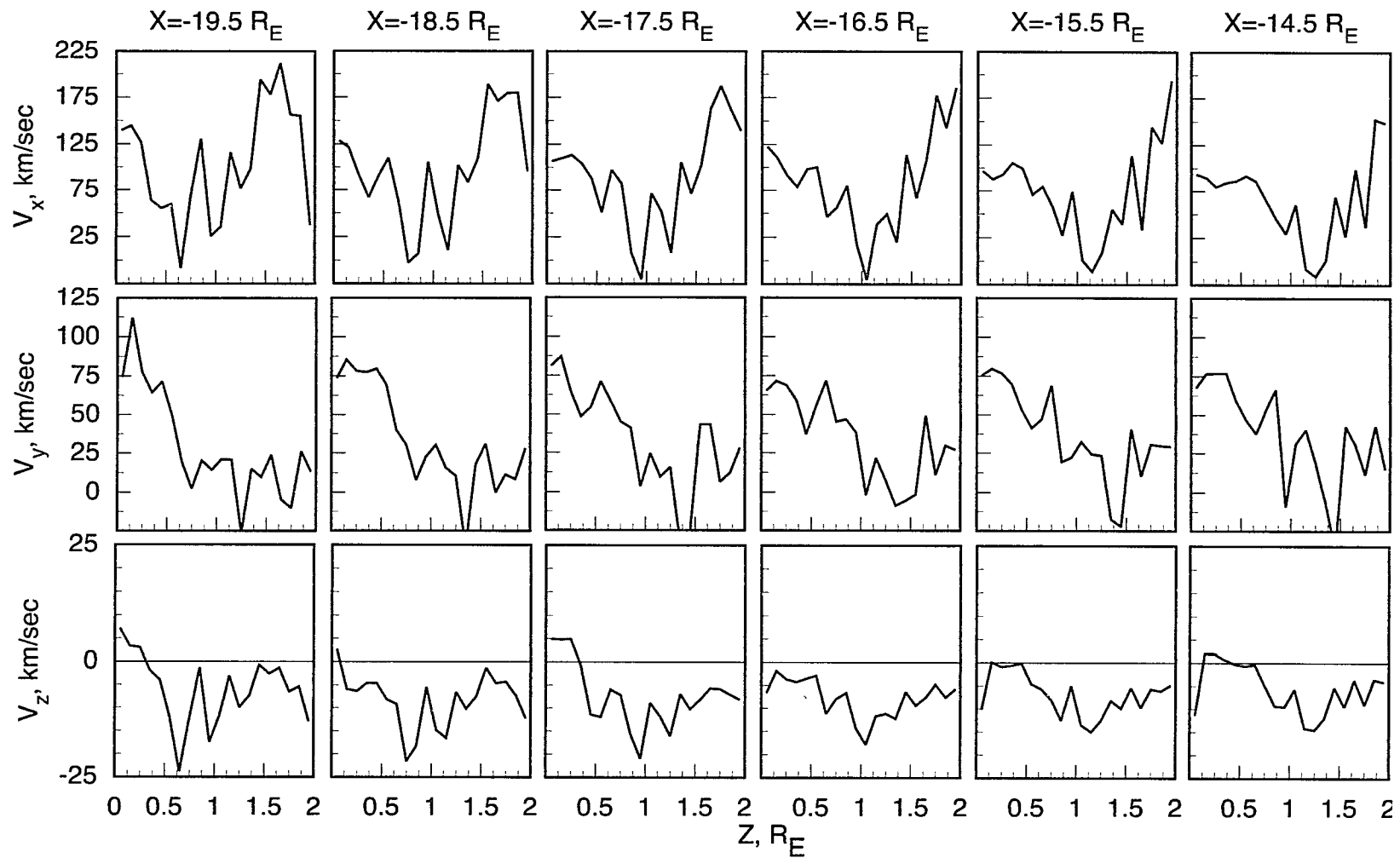
Figure 5.11: Bulk velocity profiles of the standard/5 keV case.
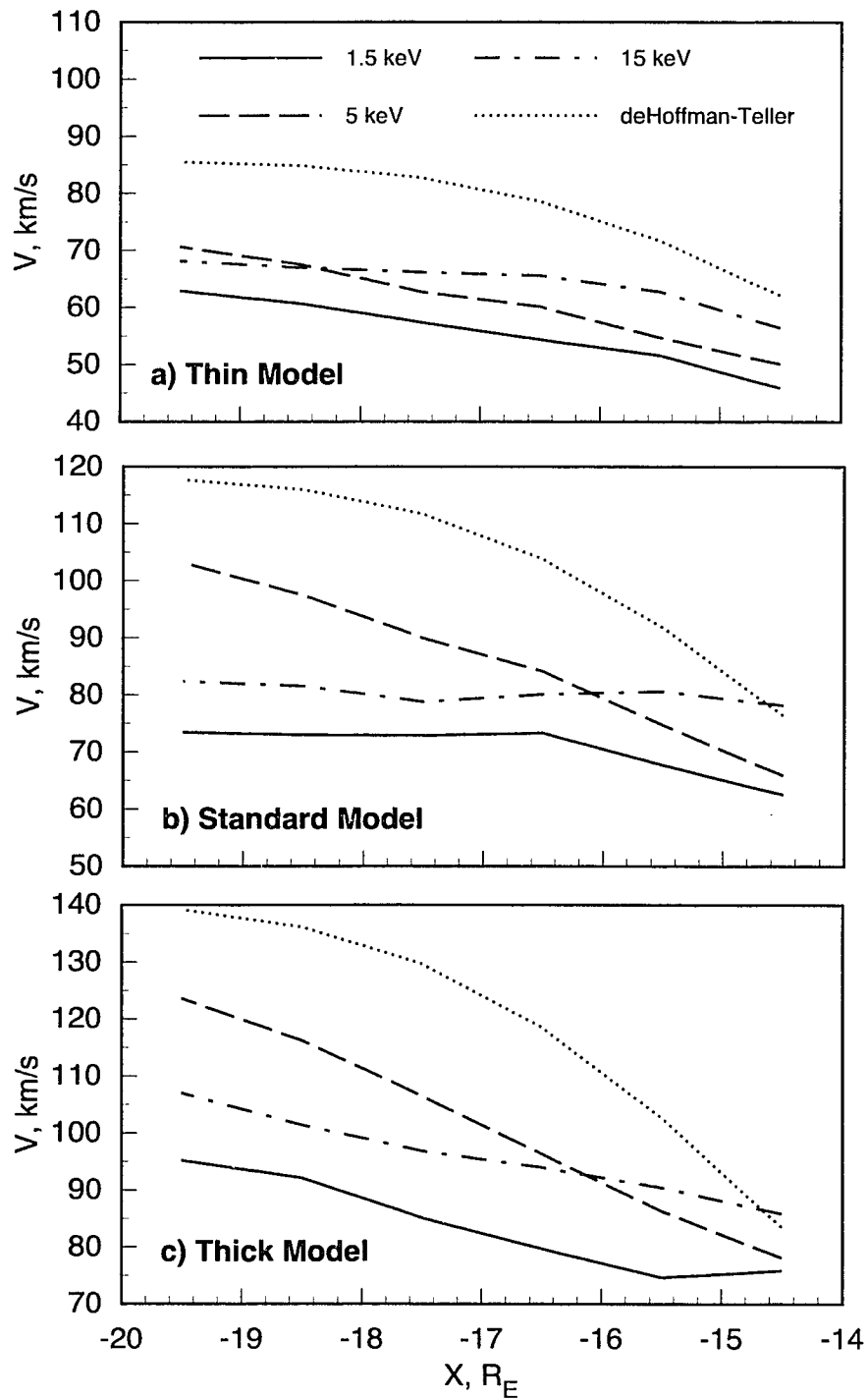
Figure 5.12: Plot of E_y/B_{zo} and $<V_x>$ a) Thin model, b) Standard model, c) Thick model.
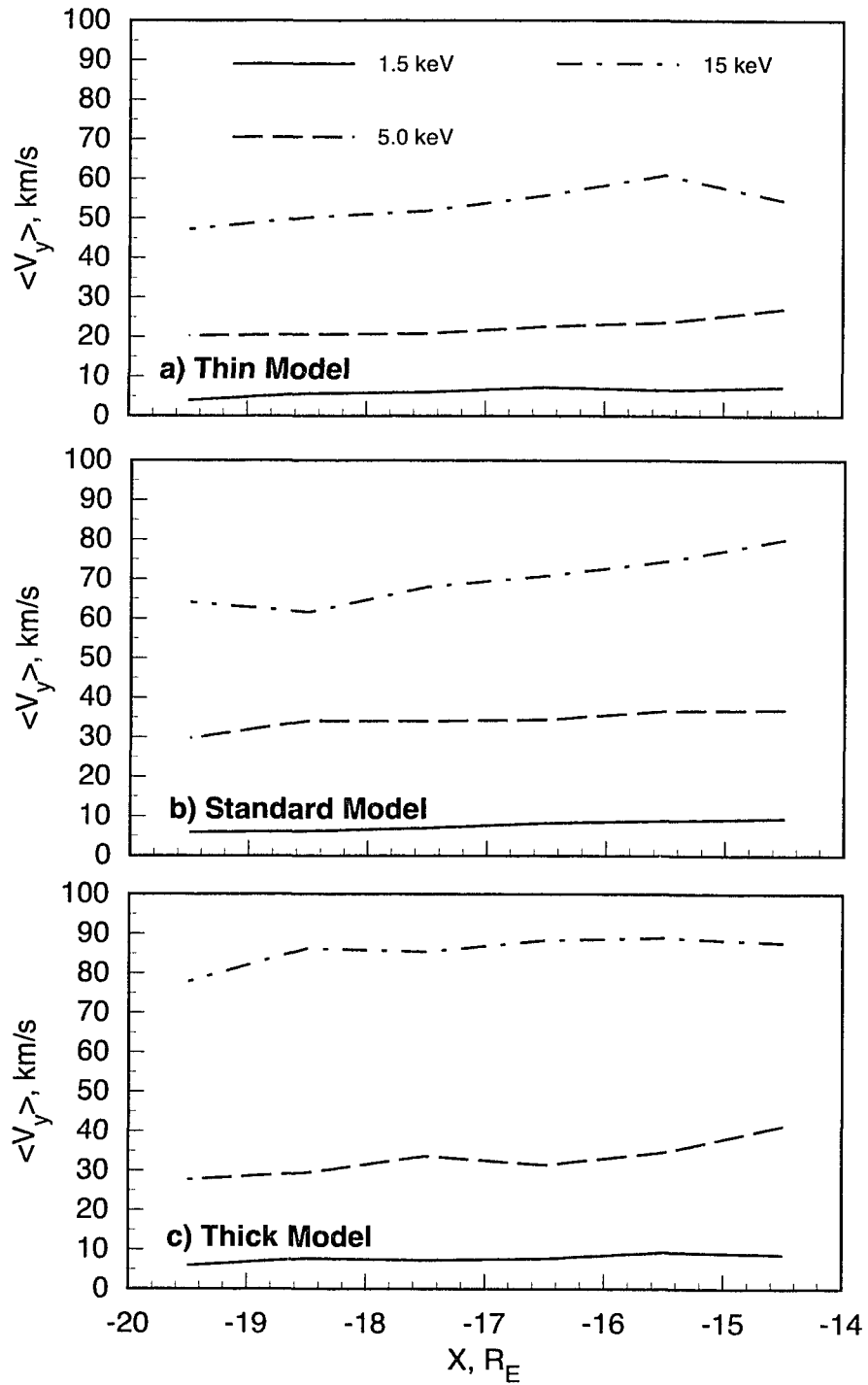
Figure 5.13: Plot of <V$_y$> for the a) Thin; b) Standard; and c) Thick models
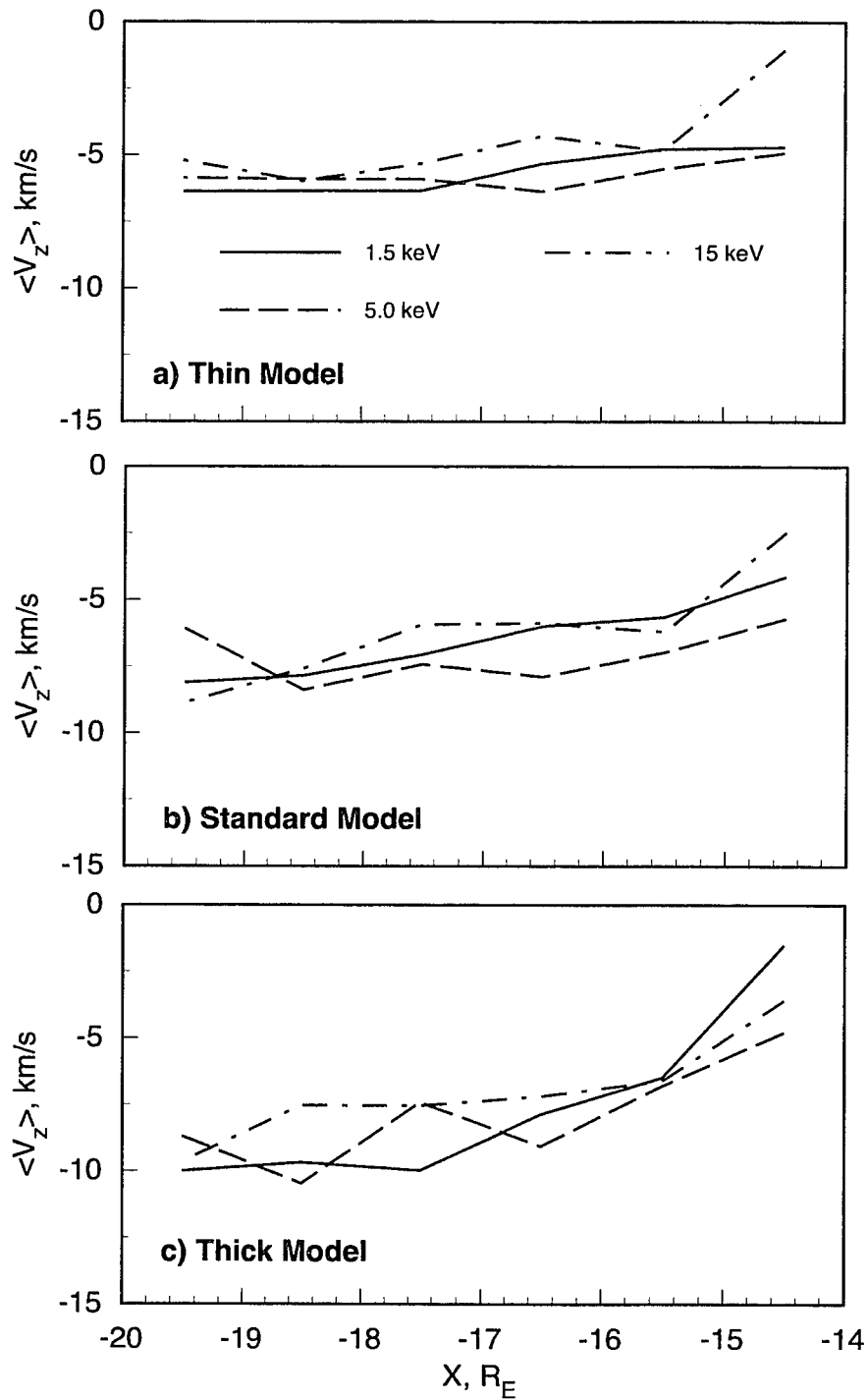
Figure 5.14: Plot of $<V_z>$ for the a) Thin; b) Standard; and c) Thick models

No field aligned current is expected in the present steady state model with essentially no y dependence in the region of interest.

5.3 Force Balance

Stress and pressure tensors

This section presents the tensors that were calculated and the conclusions that were drawn for the standard / 5 keV model. These tensors are needed to determine how nearly pressure balance was attained by the SCOT calculations. The ion stress tensor or kinetic pressure tensor is

$$T_{i,\alpha\beta} = m_i \int v_\alpha v_\beta \, f_i(\mathbf{v}) d^3 v = P_{i,\alpha\beta} + \rho_i u_{i,\alpha} u_{i,\beta} \qquad (5.5)$$

where

$$u_{i,\alpha} = \frac{1}{n} \int v_\alpha \, f_i(\mathbf{v}) d^3 v \qquad (5.6)$$

$$P_{i,\alpha\beta} = m_i \int [v_\alpha - u_{i,\alpha}][v_\beta - u_{i,\beta}] \, f_i(\mathbf{v}) d^3 v \qquad (5.7)$$

In the above, v_α is a Cartesian component of the particle velocity, $u_{i,\alpha}$ is a component of the ion bulk or convection velocity, m_i is the ion mass, $n_i = n_e = n$ is the density of ions and of electrons, and $\rho_i = m_i n$ is the ion mass density. The stress tensor $T_{s,\alpha\beta}$ for particle species s is separated into portions associated with bulk flow $\rho_s u_{s,\alpha} u_{s,\beta}$ and with pressure as seen when moving with the bulk velocity $P_{s,\alpha\beta}$ so the importance of these physically distinct terms can be compared. The ion stress tensor depends only upon the calculated distribution function $f_i(\mathbf{v})$.
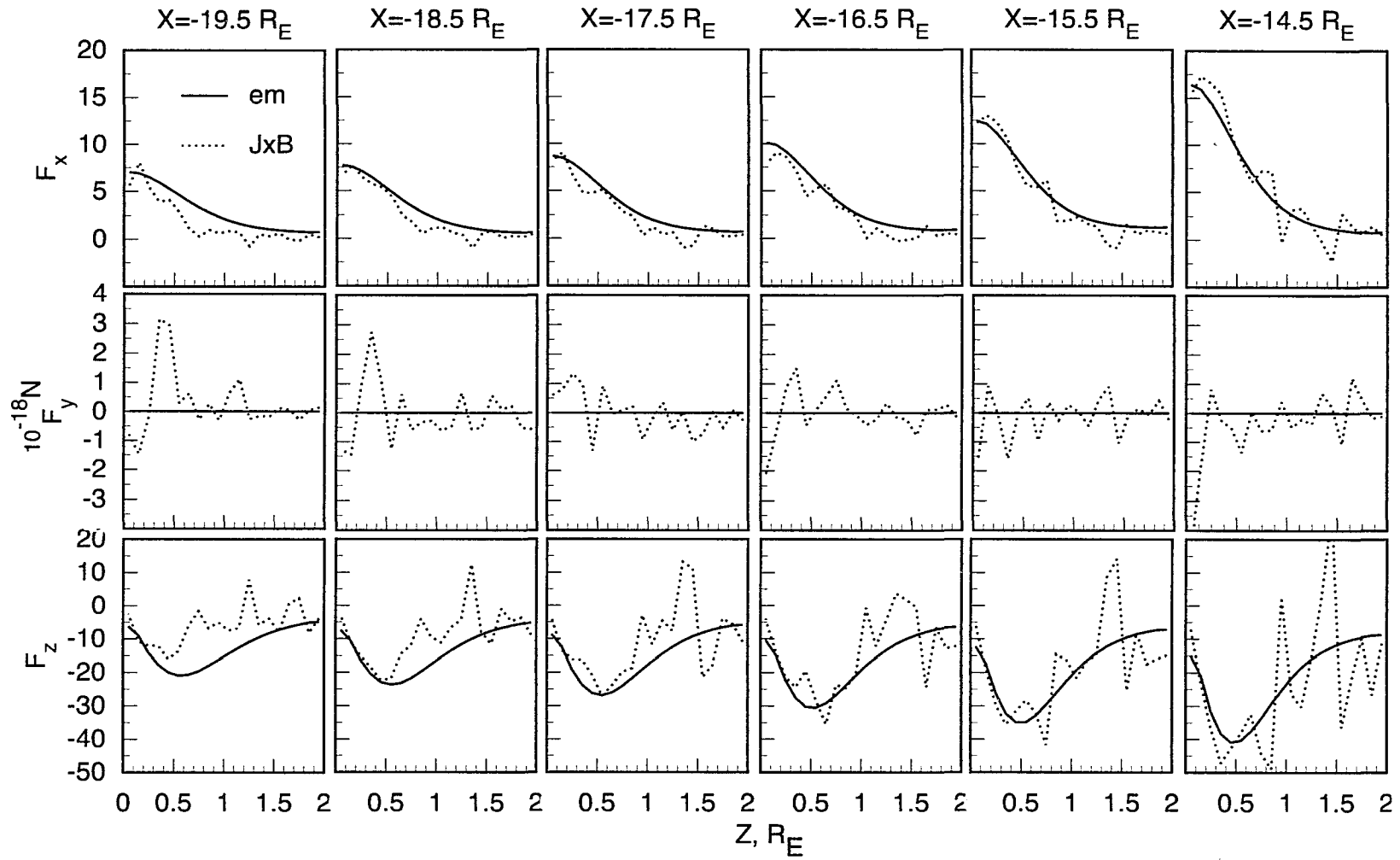
Figure 5.15: Electromagnetic forces versus the JxB forces, standard/5 keV case.
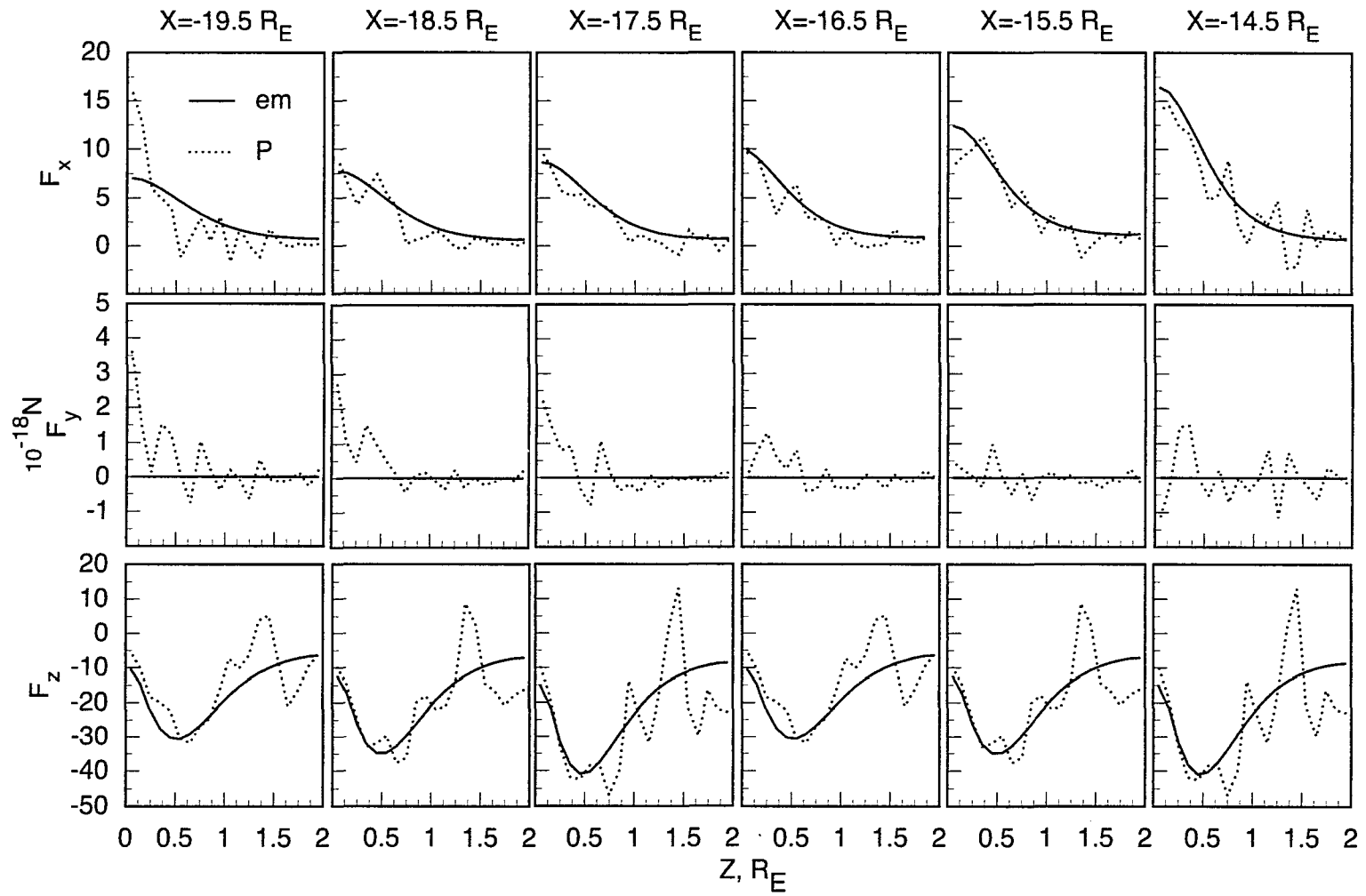
Figure 5.16: Electromagnetic forces versus the total pressure forces, standard 5 keV case.
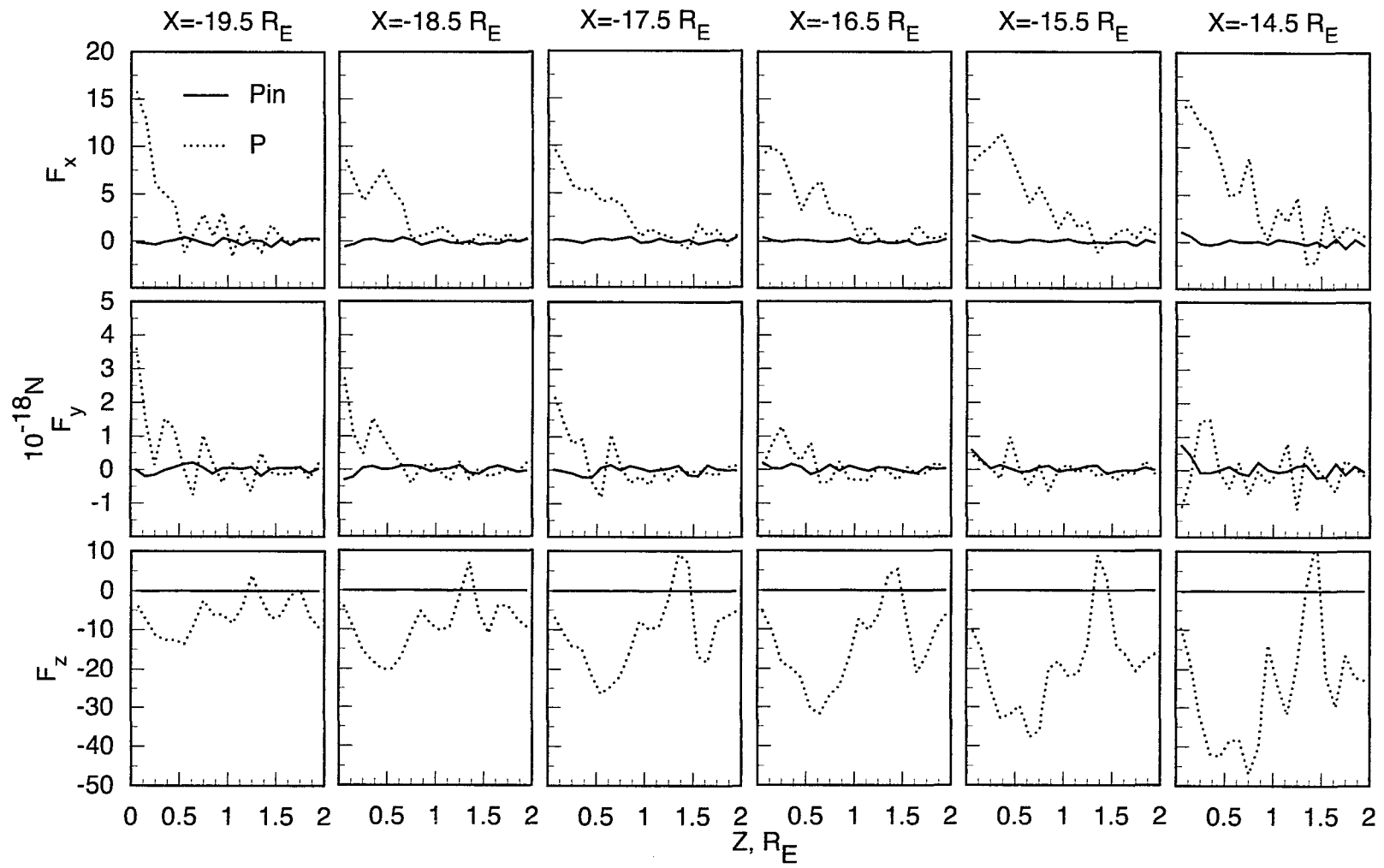
Figure 5.17: Inertial versus total pressure, standard/5 keV case.
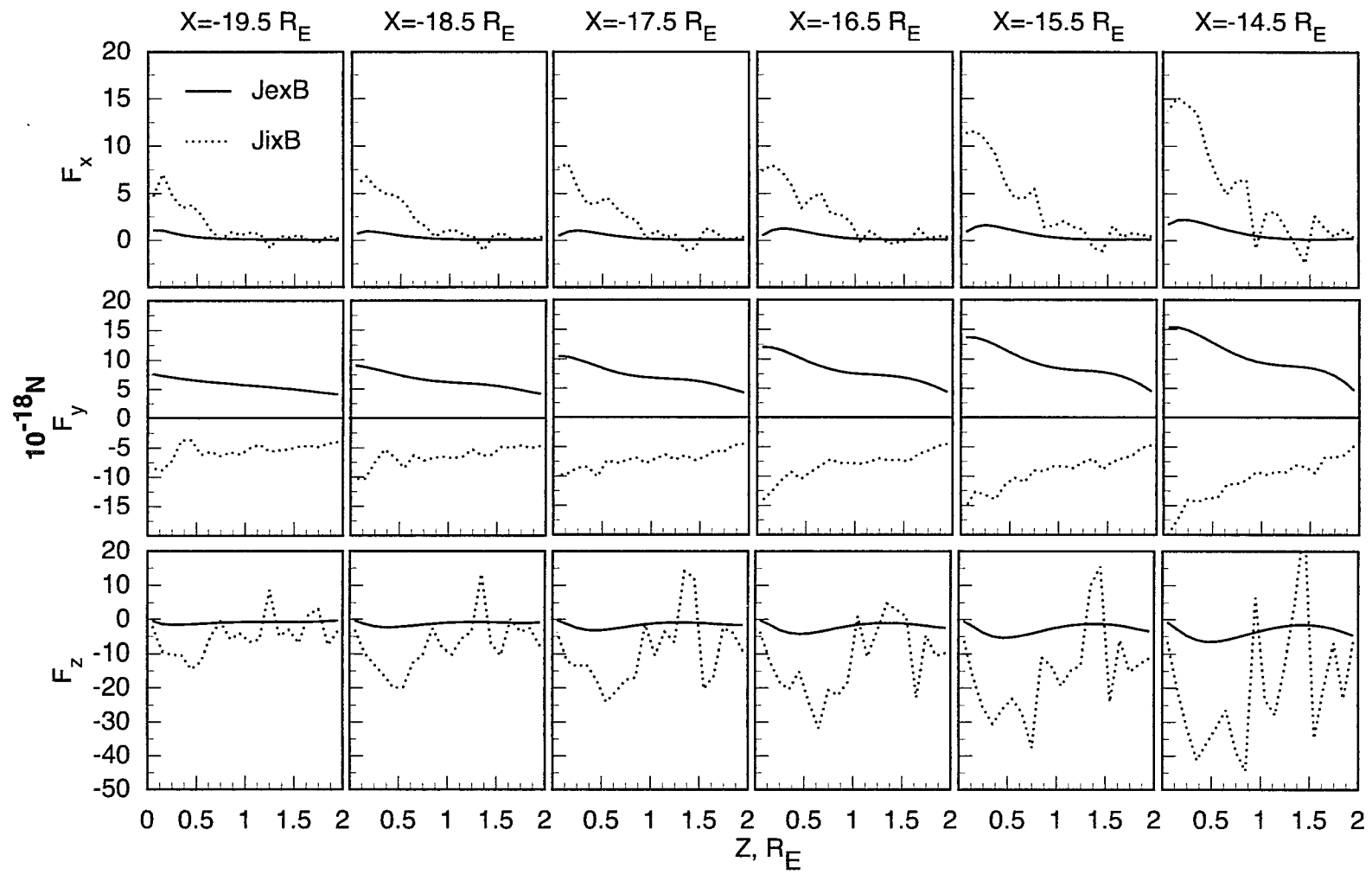
Figure 5.18: Contribution of the electrons and ions to the JxB force
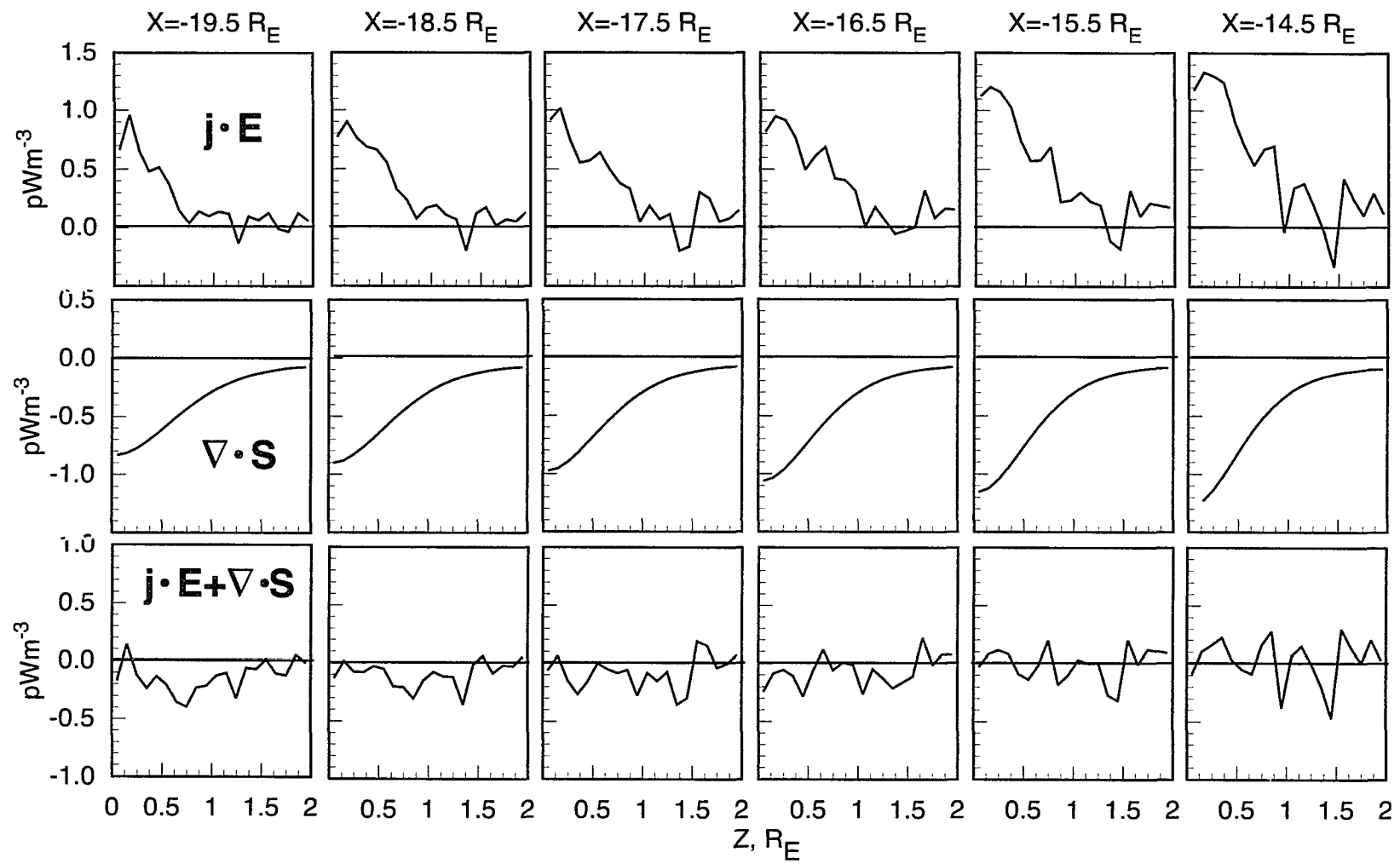
Figure 5.19: Calculated versus expected energy transfer

The electromagnetic stress tensor depends only upon the model electric and magnetic fields [*Jackson*, 1975, p 239]

$$T_{\alpha\beta}^{EM} = \varepsilon_o E_\alpha E_\beta + \frac{1}{\mu_o} B_\alpha B_\beta - \frac{1}{2}\Big[\varepsilon_o \mathbf{E} \cdot \mathbf{E} + \frac{1}{\mu_o}\mathbf{B} \cdot \mathbf{B}\Big]\delta_{\alpha\beta} \qquad (5.8)$$

A comparison of forces associated with the electromagnetic and particle stress tensors provides a check on the self-consistency of the model calculations.

Ideal steady-state self-consistent current sheet and the Vlasov equation

We first show that a model current sheet which is generated by the SCOT technique will ideally result in force balance, i.e., the forces associated with the ion plus electron stress tensor $T_{\alpha\beta}$ should equal the forces associated with $T_{\alpha\beta}^{EM}$ if self-consistency has been attained.

The Vlasov equation is based on the assumption that each particle follows an unperturbed orbit in the average field produced by all other ions and electrons. The SCOT technique explicitly follows the unperturbed orbits. This method therefore provides a way to solve the Vlasov equation provided the final plasma sheet is self-consistent in the sense described previously. The MHD force balance or momentum equation has been shown to be consistent with the Vlasov equation by taking its first velocity moment [e.g. *Spitzer*, 1962 p 155]. For particles with charge q_s this gives

$$n_s m_s \frac{\partial u_{s,\alpha}}{\partial t} + \sum_{\beta=1}^{3} \frac{\partial T_{s,\beta\alpha}}{\partial x_\beta} = n_s m_s \frac{\partial u_{s,\alpha}}{\partial t} + n_s m_s (\mathbf{u}_s \cdot \nabla) u_{s,\alpha} + \sum_{\beta=1}^{3} \frac{\partial P_{s,\beta\alpha}}{\partial x_\beta}$$
$$= n_s q_s E_\alpha + (\mathbf{j}_s \times \mathbf{B})_\alpha \qquad (5.9)$$

Ion and electron equations are added to get the total plasma momentum equation. When adding ion and electron terms it is assumed that the magnetotail is charge neutral and that terms of order m_e/m_i can be neglected relative to unity, e.g. the mass density is

$\rho = m_i n_i + m_e n_e \cong m_i n$. Electrons in the tail have only about $1/7$ the energy of ions, so that the bulk drift velocities satisfy $\mathbf{u}_e \leq \mathbf{u}_i$ in a quiet time $1\ R_E$ thick tail even though the total particle velocities satisfy $\mathbf{v}_e \gg \mathbf{v}_i$. Electron drift currents can become more important in much thinner tails, but such models will not be considered here. As a result, electron effects are retained only in the $P_{\alpha\beta}$ and $\mathbf{j}$ terms of (5.9) yielding

$$\frac{\partial}{\partial t}(\rho u_\alpha) + \sum_{\beta=1}^{3} \frac{\partial T_{\beta\alpha}}{\partial x_\beta} = \rho \frac{\partial u_\alpha}{\partial t} + \rho(\mathbf{u}\cdot\nabla)u_\alpha + \sum_{\beta=1}^{3} \frac{\partial P_{\beta\alpha}}{\partial x_\beta} = (\mathbf{j}\times\mathbf{B})_\alpha \qquad (5.10)$$

where $\rho\mathbf{u} = m_i n_i \mathbf{u}_i + m_e n_e \mathbf{u}_e \cong \rho\mathbf{u}_i$; $\mathbf{j} = \mathbf{j}_e + \mathbf{j}_i$; and $P_{\alpha\beta} = P_{e,\alpha\beta} + P_{i,\alpha\beta}$. The electric field forces cancel if the plasma is exactly neutral, and the continuity equation has been used to derive (5.10). If a truly self-consistent model was obtained, then $(1/\mu_o)\nabla\times\mathbf{B} - \varepsilon_o \partial\mathbf{E}/\partial t$ can be substituted for $\mathbf{j}$ and the magnetic field cross product can be expanded yielding the usual magnetic field pressure and tension forces. The present work involves only steady state current sheets, so from here on it is assumed that $\partial/\partial t = 0$. Therefore, in the ideal steady state case the SCOT method results in balance between the calculated particle terms on the left side of (5.10)

$$\rho(\mathbf{u}\cdot\nabla)u_\alpha + \sum_{\beta=1}^{3} \frac{\partial P_{\beta\alpha}}{\partial x_\beta} = \left[\frac{1}{2\mu_o}\nabla B^2 - \frac{1}{\mu_o}(\mathbf{B}\cdot\nabla)\mathbf{B}\right]_\alpha \qquad (5.11)$$

and the preselected magnetic field forces on the right side.

It sometimes is preferable to consider each species separately because we treat ions through orbit tracing and electrons through the guiding center approximation. It was noted above that the electron and ion $nq\mathbf{E}$ forces cancel through charge neutrality and that ion and electron guiding center $\mathbf{E}\times\mathbf{B}$ drift currents also cancel. To examine ions and electrons separately, it is useful to note that these statements are equivalent to the observation that

the portion of the $\mathbf{j} \times \mathbf{B}$ force attributable to $\mathbf{E} \times \mathbf{B}$ drift for either species exactly cancels the $nq\mathbf{E}$ force for that species, provided $\mathbf{E} \cdot \mathbf{B} = 0$. The above comments suggest a series of comparisons that can be used to check how well force balance is achieved in our approximately self-consistent model.

Overall force balance. All quantities on the left sides of (5.10) and (5.11) are directly calculated for ions, including the magnetization current effects of complex non-guiding-center orbits. Electrons are assumed to be isotropic. The average ion pressure

$$P_i(x, z) = \frac{1}{3}[P_{i,xx} + P_{i,yy} + P_{i,zz}] \tag{5.12}$$

is evaluated for each box, and a polynomial fit is made to the resulting array. The polynomial fit is used in $P_e(x, z) = (1/7)P_i(x, z)$ to calculate the electron pressure [*Baumjohann et al.*, 1989]. The usual guiding center drift equation [e.g. equation (7) of *Kaufmann and Lu*, 1993], with $\mathbf{E} \times \mathbf{B}$ drift included, is used to evaluate $\mathbf{j}_e(x, z)$ and therefore the convection speed $\mathbf{u}_e = \mathbf{j}_e/nq_e$. This provides all the electron parameters needed to evaluate the left sides of (5.10) and (5.11).

The electromagnetic force can be written either as

$$\mathbf{F}_\alpha^{EM} = \sum_{\beta=1}^{3} \frac{\partial T_{\beta\alpha}^{EM}}{\partial x_\beta} \tag{5.13}$$

or, for the 2-D model, as the right side of (5.11). By Ampere's law, this force should equal $\mathbf{j} \times \mathbf{B}$ if electrons and ions in the model have been selected so they self-consistently generate the preselected field. However, we use only $j_y(x, z)$ to select the ion and electron groups that compose the final distribution, and the fits are only approximate. The model also has no y dependence. Several potentially important terms such as $\partial T_{s,\alpha\beta}/\partial y$ therefore are not present in the analysis. For example, it is not possible to study the diversion of cross

tail current to the ionosphere in this model. By symmetry, it is most likely that there is little

y dependence in the magnetotail near midnight, suggesting comparisons with observations

in this region. However, even at midnight it is possible to have some y dependence, in the

average ion and electron energies for example. The above considerations suggest a number

of tests that should be made to determine whether the model is realistic.

The first test is to compare all components of (5.12) or the right side of (5.10) with

the right side of (5.11). This comparison will test whether it is adequate to ignore the sub-

stantial x and z components of ion and electron currents because they are primarily associ-

ated with $\mathbf{E} \times \mathbf{B}$ drifts, and therefore should nearly cancel. The solid lines in Figure 5.15

show the three components of the required $\mathbf{F}^{EM}$ calculated using (5.8). The dashed lines

are components of $\mathbf{j} \times \mathbf{B}$ calculated using currents carried by the ions and electrons. Results

are shown as a function of z for the six x-boxes. Derivatives calculated using finite differ-

ences do not tend to be smooth, as is evident near $z = 0$ for all the force plots.

The y component of $\mathbf{j}(x, z)$ contributes to the x and z components in Figure 5.15.

The electron current has large x and z components primarily as a result of $\mathbf{E} \times \mathbf{B}$ drift, and

a general Earthward drift also is evident in the complex ion trajectories. These currents pro-

duce most of the y component of $\mathbf{F}^{EM}$. The y component represents the difference between

a positive contribution from electron drift current, which is based on the smooth polynomi-

al fit to pressures, and an unsmoothed negative contribution from ion currents. Since the

magnitude of the y component is much smaller than the other two components it is plotted

at a different scale giving it the appearance of being more jagged. Figure 5.18 explicitly

shows electron and ion contributions to the $\mathbf{j} \times \mathbf{B}$ force. In general, it is encouraging to find

that the goodness of fits to all components of $\mathbf{F}^{EM}$ are comparable to the accuracy with

which the model $j_y(x, z)$ agrees with the desired j_y in the original fitting procedure.

Another test involves comparing $\mathbf{F}^{EM}$ with the left side of (5.11). This provides a direct comparison between electromagnetic forces and particle forces. The solid lines in Figure 5.16 again are $\mathbf{F}^{EM}$, and the dashed lines are the ion plus electron components of all particle stress tensor forces. The agreement of each component again is comparable to the quality of the fit in our original selection of $j_y(x, z)$.

Finally, Figure 5.17 separately shows the convection and pressure tensor components of the ion stress tensor force. The electron convection term is negligible and the electron pressure term is approximately 1/7 of the ion term. It is evident that the modest steady-state bulk flow associated with an 0.3 mV/m cross tail electric field is unimportant to a study of force balance. Much more rapid flow is observed during bursty bulk flow events [*Angelopoulos et al.*, 1994], so the convection term is likely to be important at times.

5.4 Energy Flow

Energy transfer

The total energy density of the fields U , is given by equation (5.14). The Poynting vector, denoted by $\mathbf{S}$ in equation (5.15), represents the rate of electromagnetic energy flow

$$U = \varepsilon_o E^2 + \frac{1}{\mu_o} B^2 \qquad (5.14)$$

$$\mathbf{S} = \frac{1}{\mu_o} \mathbf{E} \times \mathbf{B} \qquad (5.15)$$

Poynting's theorem is

$$\frac{\partial U}{\partial t} + \nabla \cdot \mathbf{S} = -\mathbf{J} \cdot \mathbf{E} \qquad (5.16)$$

The net electromagnetic energy flux flowing into a unit volume, $-\nabla \cdot \mathbf{S}$, is calcu-

lated using the preselected fields. At steady state, this should equal $-\mathbf{J} \cdot \mathbf{E}$, the rate at which all particles in the unit volume gain energy. This latter quantity depends on currents carried by ions and electrons in the model magnetotail. Figure 5.19 is representative of the results found for all nine cases and it shows that the comparison is comparable to the accuracy found in the force balance tests.

Energy distribution

The kinetic energy gained by ions and electrons is distributed between flow and internal energies. In order to make a clear distinction between the flow and internal energies, it is common to separate the particle stress tensor into the ideal or "dry fluid" component $T^d_{s,\alpha\beta} = m_s n u_{s,\alpha} u_{s,\beta} + P_s \delta_{\alpha\beta}$ and the remaining anisotropic and off diagonal or viscous component $T^v_{s,\alpha\beta} = P_{s,\alpha\beta} - P_s \delta_{\alpha\beta}$. This separation of ideal and viscous pressure elements also is useful because the tail magnetic field model used is one of a class that is referred to as "equilibrium models". This term means that it should be possible to create approximate force balance using isotropic distribution functions.

Energy balance in the magnetotail for each species is given by considering the flow and thermal energy densities [Fetter and Walecka, 1980]

$$
\frac{\partial}{\partial t}\left[\frac{1}{2}\rho_s u_s^2 + \rho_s e_s\right] = -\nabla \cdot \left[\mathbf{u}_s\left(\frac{1}{2}\rho_s u_s^2\right)\right] - \nabla \cdot [\rho_s e_s \mathbf{u}_s]
$$
$$
-\nabla \cdot [P_s \mathbf{u}_s] - \sum_{\alpha,\beta=1}^{3} \frac{\partial}{\partial x_\alpha}[T^v_{s,\alpha\beta} u_{s,\beta}] - \nabla \cdot \mathbf{Q}_s + \mathbf{j}_s \cdot \mathbf{E}
$$

(5.17)

where

$$
\rho_s e_s = \int \left[\frac{1}{2}m_s(\mathbf{v} - \mathbf{u}_s)^2\right]f_s(\mathbf{v})d^3 v
$$

(5.18)

is the internal or thermal energy. Thermal diffusivity has been omitted for the collisionless

model used here. The rate of change of the total energy density, given by the left side of (5.17), is zero in the steady state model. The six terms on the right side of (5.17) are, respectively, the net flux of bulk flow energy associated with plasma flow into and out of a fixed unit volume, the similar flux of internal energy, the rate at which work is done by isotropic pressure forces on plasma flowing into and out of the volume, the total work done by off diagonal or viscous forces on plasma flowing into and out of the volume, heat conduction, and the transfer of electromagnetic energy to particles. The off diagonal or viscous electron terms are all zero in our model.
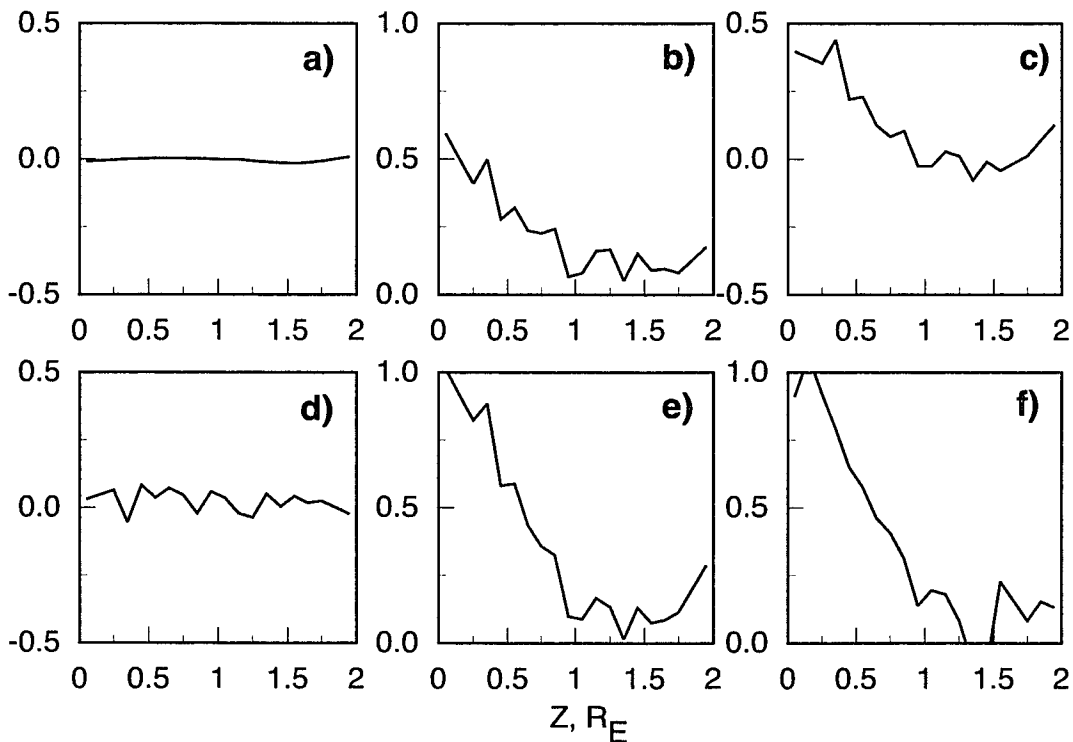
Figure 5.20: Contributions by term to the energy balance equation where; a) is the net flux of the bulk flow energy; b) flux of the internal energy; c) work done by pressure forces; d) heat flux; e) sum of the contributions of a)-d); and f) the transfer of electromagnetic energy to the particles. This data is from the standard/5 keV case.

Flow energy and internal energy in a fixed box must separately be constant in the steady state model. This separation permits a study of the importance of non-guiding-center aspects of energy dissipation. In a guiding center model, all terms on the right side of (5.17) except the second add to the flow energy density. Two additional terms

$$P_s(\nabla \cdot \mathbf{u}_s) + \sum_{\alpha, \beta = 1}^{3} T^\nu_{s, \alpha\beta} \frac{\partial u_{s, \beta}}{\partial x_\alpha} \tag{5.19}$$

are needed to separately study flow and internal energy conservation. These two terms involve the conversion between thermal and flow energy within the unit volume, but involve no net work done on all particles in the volume taken as a whole.

The first term in equation (5.19) is the work associated with compression. The second term in (5.19) is the energy dissipated or converted from flow to thermal energies within the volume by viscous forces. The second term on the right of (5.17) minus the two terms in (5.19) equal the rate of change of internal energy density, so must add to zero in the steady state model. Similarly, the remaining 5 terms on the right of (5.17) plus the two terms in (5.19) must add to zero to produce steady bulk flow. This can be seen in Figure 5.20.

Figure 5.20 shows all the terms of equation (5.17) that can be calculated directly. Given the coarseness of the 6 xbox grid and the effects of finite differencing, the results for each x box were smoothed once and then averaged together to create one representation of the terms of the energy balance equation. The curves in Figures 5.20a-5.20c show the first three terms on the right of (5.17); a) is the net flux of the bulk flow energy; b) flux of the internal energy; and c) the work done by pressure forces. The flow of energy associated with plasma flow into and out of a fixed unit volume is negligible in relation to all the other

terms. Figure 5.20d shows the heat flux term on the right of equation (5.17). Figure 5.20e

is the sum of the first four terms. The fifth term was zero as previously stated and so is not

plotted. Energy balance requires that Figure 5.20f, the $\mathbf{j} \cdot \mathbf{E}$ term of equation (5.17), should

be the same as Figure 5.20e. Despite the noisy nature of the calculations, energy balance is

seen to be satisfied.

5.5 Thermodynamic Considerations of the Model Current Sheets

Convecting plasma obeys the equation of state

$$pV^{\gamma} = \alpha \qquad (5.20)$$

where p is the plasma pressure, γ is the ratio of specific heats C_p/C_v, V is the volume of

the flux tube, and α is a constant. The volume of a flux tube of unit magnetic flux is defined

to be

$$V \equiv \int \frac{ds}{B} \qquad (5.21)$$

where the integral is taken along the full length of a closed magnetic field line and B is the

magnitude of the field. Taking the logarithm of equation (5.20) gives

$$\log p = -\gamma \log V + \log \alpha \qquad (5.22)$$

The value of γ is determined by doing a linear regression [*Press et al.*, 1993] of the

logarithmic values of the pressure and the flux tube volume. The regression coefficients for

the nine cases are summarized in Table 5.1.

No coherent trend in γ over the entire set of nine cases presented in Table 5.1 can

really be seen. The two cases which had the worst current sheet fits, thin and thick 1.5 keV,

also have the worst error in the γ fits. The standard/1.5 keV was also not a very good cur-

rent sheet fit yet it and the thin/1.5 keV case have γ values closer to the adiabatic ideal of

$\gamma = 5/3$. The current sheet fits for all three 15 keV cases were quite good yet no apparent

pattern can be seen in γ other than that they are lower than the other cases. Results of cases

with particles started at 5 keV exhibit γ values close to the adiabatic ideal of $\gamma = 5/3$.

Although this is encouraging we can cannot make any definitive conclusions about the ef-

ficacy of using the SCOT method to overcome the pressure balance inconsistency (PBI).

Table 5.1: Ratio of specific heats γ for the nine cases

Current Sheet Type	1.5 keV	5.0 keV	15.0 keV
Thin	1.7889±0.1135	1.6996±0.0580	1.2494±0.0763
Standard	1.5886±0.0340	1.6493±0.0937	0.9865±0.0273
Thick	1.1773±0.1413	1.6888±0.0753	1.1576±0.0868

Table 5.2: Polytropic Index n for the nine cases

Current Sheet Type	1.5 keV	5.0 keV	15.0 keV
Thin	1.4475±0.0794	1.6710±0.0312	2.0295±0.1537
Standard	1.4887±0.0535	1.5251±0.0797	2.3580±0.1099
Thick	1.4165±0.5236	1.6294±0.0696	1.9926±0.1852

Baumjohann and Paschmann [1989] calculate the polytropic index in the plasma

sheet for ions using IRM data using the equation of state

$$p\rho^{n} = \alpha, \qquad (5.23)$$

where p is the plasma pressure, n is the polytropic index, ρ is the number density, and α

is a constant. The polytropic index is calculated in a similar fashion to that of γ by doing a

linear regression analysis of the $\log p$ and $\log \rho$ values. As can be seen when comparing

Table 5.1 with the results of Table 5.2, the polytropic index is generally not equal to the

ratio of specific heats γ. The exception is the 5 keV cases which tend to agree with

$n = \gamma = 5/3$, implying an isentropic process. The cases that started with low energy ions

consistently give polytropic indices less than 5/3 of around 1.45. The cases with ions started

at 15 keV have polytropic indices of around 2, regardless of the magnetotail model used.

The results presented here agree with that of *Baumjohann and Paschmann* [1989].

They observed that the plasma sheet ion population, on average, behaves adiabatically in

both the central plasma sheet (CPS) and the plasma sheet boundary layer (PSBL). We show

that regardless of the model magnetotail thickness, the low ion energy particle current sheet

is non-adiabatic with an average polytropic index of 1.45. Thus if any of these systems were

used as the initial state of a time dependent simulation heat would be lost at the outset un-

less a supply of higher energy particles were provided to the system. Current sheets formed

with higher starting energies appear to be adiabatic in their behavior. An average polytropic

index of 1.4 was observed by *Baumjohann and Paschmann* [1989] for quiet time plasma

sheets. Although this study assumes protons as we do here, they only state their results for

the total energy range of their instrument (20 eV/e to 40 keV/e). This prohibits comparisons

based on energy ranges with our results. So we are left with the possibility that a steady

state, $\partial/\partial t = 0$, plasma sheet may be constructed from appropriate particle populations.

Chapter VI

CONCLUSIONS

The two-dimensional approximation of an inherently three-dimensional electro-magnetic structure like the Earth's magnetotail runs the risk of disregarding important three dimensional effects. However if the model is developed to mimic a specific cross section of the tail and carefully applied to specific magnetotail problems, useful physics can still be learned. This has been the case in this study.

A simple equilibrium type magnetotail model that approximates the noon-midnight cross section of the much more complicated Tsyganenko 1989 model was presented in chapter two. The model magnetotail developed for this work is a superposition of three fields; an Earth centered dipole, the magnetic field generated by a ring current, and an equi-librium tail field plus a uniform B_{zo}. The entire model is divergence free owing to the use of three-dimensional dipole and ring current terms. The complete model is self consistent. Selection of three sets of parameters allowed the generation of current sheets that varied in thickness where the total cross-field currents and κ were adjusted to approximate the T89 model in the midtail $-20 < x < -14$ R_E region. The lack of B_y in the model does affect force balance results. This should not be taken as a failure of the model since by eliminating strong B_y from the midtail region we can see the importance of the cross-tail field for maintaining force balance. One feature of the new model that should not be overlooked is the fact that it is both simple and fast to implement on a computer as compared to the full

T89 model. The order of magnitude speed improvement over a T89 model with $y = 0$ that is commonly employed by other workers and run on multimillion dollar supercomputers means that more economical desktop workstations can be used to extract the same results. Furthermore, the limitations of the one-dimensional Harris model can also be overcome with a relatively simple implementation.

The procedures followed during an Self Consistent Orbit Tracing were described. The principal steps were: select a number of proton groups; trace orbits of the protons in each group; evaluate the cross-tail current carried by each group of ions plus their associated electrons; combine these groups so that they generate a nearly self-consistent current sheet model. In a self-consistent current sheet, the ions and electrons carry the current needed to generate the magnetic field in which the orbits were traced.

A set of 9 SCOT analyses were carried out using 3 proton energies (1.5, 5, and 15 keV) for each of 3 magnetic field models. Characteristic current sheet thickness scale lengths varied from 0.3 R_E to 1 R_E in the models used. Selection of these thicknesses was guided by the few available observations of the instantaneous structure of a steady magnetotail current sheet. A uniform zeroth order cross-tail electric field was present in all calculations. A first order parallel electric field was added to maintain charge neutrality.

A previous study using a 1D or modified Harris magnetic field model was unable to generate a current sheet that agreed with observations in the $-20 R_E < x < -14 R_E$ region of interest. The introduction of the set of 2D models, which have both x and z dependence, removed the inconsistencies found in the earlier 1D analysis. It was possible to generate nearly self-consistent current sheets for 6 of the 9 magnetic field model and particle energy combinations. Adequate solutions were not found when attempting to combine the thicker

model current sheets with the lower energy particles.

One of the goals was to investigate individual particle orbits in order to gain a better physical understanding of current sheet structure. All ions in each group were started with the same energy so that the group would be dominated by a particular type of orbit. Particle orbits previously have been classified according to the dynamical properties of the particles. Guiding center, chaotic, and resonant orbits are examples. Instead, orbits in this work were classified according to the characteristic spatial distribution of cross-tail current carried by the particles in the region of interest. This resulted in the 3 orbit categories described in chapter four; inner mirroring, central mirroring, and outer mirroring. As supported by Tables 4.1 to 4.3, self-consistent current sheets could not be created in any of the 9 cases studied without using all 3 orbit categories.

An investigation of single ion orbits showed the orbital features that resulted in the characteristic $j_y(x, z)$ pattern carried by particles in each orbit category. It was primarily magnetization currents that produced the structure and characteristic scale of the magnetotail current sheet, though separating drift from magnetization currents may not be meaningful near $z = 0$. A number of assumptions were introduced in order to include electrons. Some of these assumptions were needed to satisfy basic requirements of the steady state model, such as charge neutrality and conservation. Other assumptions, such as the ratio of electron to ion energy, were based on observations. Electrons with the energies used here obeyed the guiding center approximations throughout the region of interest in the 3 magnetic field models.

Cross-tail electron currents were relatively small in the model current sheets studied here. However, electron current can be much more important in a thinner current sheet. Ex-

tremely thin current sheets have been observed just before and more commonly just after substorm onsets. The present work did not attempt to model such situations.

The SCOT analysis produced an ion distribution function for each of the 120 spatial boxes used in this study. The distribution functions were integrated to evaluate fluid parameters. Three of the simplest parameters: the ion density, temperature, and bulk flow velocity, were in good agreement with observations.

The results of this analysis support the postulate that the current in sheet-like structures usually is carried by particles with κ a little less than one. The magnetic field in a current sheet must be carried by charged particles within the sheet. In contrast, particles trapped in the ring current or other belt-like structures carry little of the current that is needed to create the local magnetic field. In the present work we found it difficult to create a current sheet with particles with $\kappa > 1$. The previous 1D analysis showed that it is difficult to create a self-consistent current sheet using particles with $\kappa < 0.1$. Particles with such small κ values bounce many times back and forth across $z = 0$ during each current sheet interaction [*Speiser*, 1965]. The problem is that most such particles have $z_o > L$, where L is the characteristic current sheet thickness. Such particles bounce, and therefore carry strong currents well beyond the current sheet. Self-consistent models require all current to be confined inside the current sheet.

Space weather efforts need local as well as global observations to fulfill the objective of protecting satellites and terrestrial power grids from major substorm events and help in terrestrial climate modeling. Understanding of the microscopic plasma effects of the midtail neutral sheet will help explain conditions during the critical pre-onset time before

major substorm events. This work resolves some of the problems in understanding the current sheet as well as developing tools for future studies.

LIST OF REFERENCES

Akasofu, S.-I. and Chapman, S. C., Solar-Terrestrial Physics, Oxford University Press, 1972.

Alekseyev, I. I. and A. P. Kropotkin, Interaction of energetic particles with the neutral sheet in the tail of the magnetosphere, Geomagnetism and Aeronomy, 10, 615 - 619, 1970.

Alfvèn, H. and C.-G. Fälthammar, Cosmical Electrodynamics, 222 pp., Clarendon Press, Oxford, 1963.

Allen, J., H. Sauer, L. Frank and P. Reiff, Effects of the March 1989 solar activity, Eos Trans. AGU, 70, 1479, 1486 - 1488, 1989.

Ames, W. F., Nonlinear partial differential equations in engineering, Academic Press, New York, 1967.

Angelopoulos, V., C. F. Kennel, F.V. Coroniti, R. Pellat, M. G. Kivelson, R. J. Walker, C. T. Russell, W. Baumjohann, W. C. Feldman, and J. T. Gosling, Statistical characteristics of bursty bulk flow events, J. Geophys. Res., 99, 21257-21280, 1994.

Ashour-Abdalla, M., J. Berchem and J. Büchner, Large and small scale structures in the plasma sheet: A signature of chaotic motion and resonant effects., Geophys. Res. Lett., 18, 1603 - 1606, 1991.

Ashour-Abdalla, M., J. Berchem, J. Büchner and L. M. Zelenyi, Chaotic scattering and acceleration of ions in the Earth's magnetotail, Geophys. Res. Lett., 17, 2317-2320, 1990.

Ashour-Abdalla, M., J. P. Berchem, J. Büchner and L. M. Zelenyi, Shaping of the magnetotail from the mantle: Global and local structuring, J. Geophys. Res., 98, 5651-5676, 1993.

Ashour-Abdalla, M., J. Büchner and L. M. Zelenyi, The Quasi-Adiabatic Ion Distribution in the Central Plasma Sheet and Its Boundary Layer, J. Geophys. Res., 96, 1601 - 1609, 1991.

Ashour-Abdalla, M., L. M. Zelenyi, J.-M. Bosqued, V. Peroomian, Z. Wang, D. Shriver and R. L. Richard, The formation of the wall region: Consequences in the near Earth magnetotail, Geophys. Res. Lett., 19, 1739 - 1742, 1992.

Ashour-Abdalla, M., L. M. Zelenyi, J. M. Bosqued and R. A. Kovrazhkin, Precipitation of fast ion beams from the plasma sheet boundary layer, Geophy. Res. Let., 19, 617 - 620, 1992.

Ashour-Abdalla, M., L. M. Zelenyi, J. M. Bosqued, V. Peroomian, Z. Wang, D. Schriver and R. Richard, Effects of near-earth stochastic acceleration and reflections of magnetotail ions on the formation of auroral arcs, in *International Conference on Substorms*, 545 - 552, Kiruna, Sweden, 1992.

Ashour-Abdalla, M., L. M. Zelenyi, V. Peroomian and R. L. Richard, On the structure of the magnetotail current sheet, *Geophy. Res. Let.*, **20**, 2019 - 2022, 1993.

Baumjohann, W., Plasma sheet equation of state, in *Proceedings of the International Conference on Substorms (ICS-1)*, **ESA SP-335**, 539-542, ESA, Kiruna, Sweden, 1992.

Baumjohann, W., G. Paschmann and C. A. Cattell, Average Plasma Properties in the Central Plasma Sheet, *J. Geophys. Res.*, **94**, 6597 - 6606, 1989.

Baumjohann, W., G. Paschmann, T. Nagai and H. Luhr, Superposed epoch analysis of the substorm plasma sheet, *J. Geophys. Res.*, **96**, 11605-11608, 1991.

Baumjohann, W., R. J. Pellinen, H. J. Opgenoorth and E. Nielsen, Joint two-dimensional observations of ground magnetic and ionospheric electric fields associated with auroral zone currents: Current systems associated with local auroral break-ups, *Planet. Space Sci.*, **29**, 431 - 447, 1981.

Baumjohann, W., D. Sachsenweger and E. Möbius, Suprathermal ion fluxes in the plasma sheet, *Geophy. Res. Lett.*, **17**, 275-278, 1990.

Beard, D. B., The Magnetotail Magnetic Field, *J. Geophys. Res.*, **84**, 2118 - 2122, 1979.

Beard, D. B., D. Hirschi and K. Propp, The Tailward Magnetopause Field Beyond 10 Re, *J. Geophys. Res.*, **87**, 2533 - 2537, 1982.

Benford, G. and D. L. Book, <u>Relativistic Beam Equilibria</u>, edited by A. Simon and W. B. Thompson, pp 125 - 171, Interscience, NY, 1971.

Bennett, W. H., Magnetically self-focussing streams, *Physical Review*, **45**, 890-897, 1934.

Berchem, J. and C. T. Russell, The Thickness of the Magnetopause Current Layer: ISEE 1 and 2 Observations, *J. Geophys. Res.*, **87**, 2108 - 2114, 1982.

Bernstein, I. B., J. M. Greene and M. D. Kruskal, Exact nonlinear plasma oscillations, *Phys. Rev.* **108**, 546-550, 1957.

Bird, M. K. and D. B. Beard, The self-consistent geomagnetic tail under static conditions, *Planetary and Space Science*, 20, 2057-2072, 1972.

Birdsall, C. K. and A. B. Langdon, <u>Plasma Physics via computer simulation</u>, 479 pp., Adam Hilger, New York, 1991.

137

Birn, J., R. R. Sommer and K. Schindler, Open and closed magnetospheric tail configurations and their stability, *Astrophysics and Space Science*, **35**, 389-402, 1975.

Birn, J., R. R. Sommer and K. Schindler, Self-consistent theory of the quiet magnetotail in three dimensions, *J. of Geophys. Res.*, **82**, 147-154, 1977.

Birn, J., Self-consistent magnetotail theory: General solution for the quiet tail with vanishing field-aligned currents, *J. of Geophy. Res.*, **84**, 5143-5152, 1979.

Birn, J., M. Hesse and K. Schindler, Filamentary structure of a three-dimensional plasmoid, *J. Geophys. Res.*, **94**, 241, 1989.

Birn, J., The distortion of the magnetotail equilibrium structure by a net cross-tail magnetic field, *J. of Geophys. Res.*, **95**, 8019-8028, 1990.

Birn, J., E. W. Hones, Jr., J. D. Craven, L. A. Frank, R. D. Elphinstone, and D. P. Stern, On open and closed field line regions in Tsyganenko's field model and their possible associations with horse collar auroras, *J. of Geophys. Res.*, **96**, 3811-3817, 1991.

Bosqued, J. M., M. Ashour-Abdalla, M. E. Alaoui, V. Peroomian, L. M. Zelenyi and C. P. Escoubet, Dispersed Ion Structures at the Poleward Edge of the Auroral Oval: Low-Altitude Observations and Numerical Modeling, *J. of Geophys. Res.*, **98**, 19,181 - 19,204, 1993.

Bosqued, J. M., M. Ashour-Abdalla, M. E. Alaoui, L. M. Zelenyi and A. Berthelier, AUREOL-3 observations of new boundaries in the auroral ion precipitation, *Geophys. Res. Lett.*, **20**, 1203 - 1206, 1993.

Büchner, J., Correlation-modulated chaotic scattering in the Earth's magnetosphere, *Geophys. Res. Lett.*, **18**, 1595 - 1598, 1991.

Büchner, J., M. Ashour-Abdalla and L. M. Zelenyi, Ion distribution in the plasma sheet of the earth's magnetotail, *Adv. Space Res.*, **11**, 183 - 187, 1991.

Büchner, J., M. Kuznetsova and L. M. Zelenyi, Sheared Field Tearing Mode Instability and Creation of Flux Ropes in the Earth Magnetotail, *Geophys. Res. Lett.*, **18**, 385, 1991.

Büchner, J. and L. M. Zelenyi, Deterministic chaos in the dynamics of charged particles near a magnetic field reversal, *Physics Letters A.*, **118**, 395 - 397, 1986.

Büchner, J. and L. M. Zelenyi, Chaotization of the electron motion as the cause of an internal magnetotail instability and substorm onset., *J. of Geophys. Res.*, **92**, 13,456 - 13,466, 1987.

Büchner, J. and L. M. Zelenyi, Regular and chaotic charged particle motion in magnetotail-like field reversals 1. Basic theory of trapped motion, *J. of Geophys. Res.*, **94**, 11,821-11,842, 1989.

Büchner, J. and L. M. Zelenyi, Mechanisms of disruption of the energy storage in magnetotail-like systems, *Adv. Space Res.*, **10**, 145 - 148, 1990.

Büchner, J. and L. M. Zelenyi, Regular and chaotic particle motion in sheared magnetic field reversals, *Adv. Space Res.*, **11**, 177 - 182, 1991.

Burkhart, G. R. and J. Chen, Differential Memory in the Earth's Magnetotail, *J. of Geophys. Res.*, **96**, 14033 - 14049, 1991.

Burkhart, G. R. and J. Chen, Chaotic Scattering of Pitch Angles in the Current Sheet of the Magnetotail, *J. of Geophys. Res.*, **97**, 6479 - 6491, 1992.

Burkhart, G. R. and J. Chen, Particle Motion in x-Dependent Harris-Like Magnetotail Models, *J. of Geophys. Res.*, **98**, 89-97, 1993.

Burkhart, G. R., J. F. Drake and J. Chen, Magnetic Reconnection in Collisionless Plasmas: Prescribed Fields, *J. of Geophys. Res.*, **95**, 18833 - 18848, 1990.

Burkhart, G. R., J. F. Drake and J. Chen, Structure of the Dissipation Region During Magnetic Reconnection in Collisionless Plasma, *J. of Geophys. Res.*, **96**, 11539-11553, 1991.

Burkhart, G. R., J. F. Drake, P. B. Dusenbery and T. W. Speiser, Ion Tearing in a Magnetotail Configuration With an Embedded Thin Current Sheet, *J. of Geophys. Res.*, **97**, 16749 - 16756, 1992.

Burkhart, G. R., J. F. Drake, P. B. Dusenbery and T. W. Speiser, A Particle Model for Magnetotail Neutral Sheet Equilibria, *J. of Geophys. Res.*, **97**, 13799 - 13815, 1992.

Burkhart, G. R., P. B. Dusenbery and T. W. Speiser, Comment on "Physics of the Magnetotail Current Sheet" *Phys Fluids B*, **5**, 2663 (1993), 1993.

Burkhart, G. R., P. B. Dusenbery, T. W. Speiser and R. E. Lopez, Hybrid Simulations of Thin Current Sheets, *J. of Geophys. Res.*, **98**, 1993.

Burkhart, G. R., R. E. Lopez, P. B. Dusenbery and T. W. Speiser, Observational support for the current sheet catastrophe model of substorm current disruption, *Geophys. Res. Lett.*, **19**, 1635 - 1638, 1992.

Burkhart, G. R., J. Richard F. Martin, P. B. Dusenbery and T. W. Speiser, Neutral line chaos and phase space structure., *Geophys. Res. Lett.*, **18**, 1591 - 1594, 1991.

Chapman, S. C., Parameterization of Chaotic Particle Dynamics in Simple Time-Dependent Models of a Collapsing Magnetotail: A two scale model., in *International Conference on Substorms*, 559 - 564, Kiruna, Sweden, 1992.

Chapman, S. C., Properties of single-particle dynamics in a parabolic magnetic reversal with general time dependence., *J. of Geophys. Res.*, **99**, 5977 - 5985, 1994.

Chen, F. F., Introduction to plasma physics and controlled fusion, Volume 1: Plasma Physics, 421 pp., Plenum Press, New York, 1990.

Chen, J., Nonlinear Dynamics of Charged Particles in the Magnetotail, *J. of Geophys. Res.*, **97**, 15011 - 15050, 1992.

Chen, J., Physics of the magnetotail current sheet, *Physics of Fluids*, **B5**, 2663-2670, 1992.

Chen, J., G. R. Burkhart and C. Y. Huang, Observational signatures of nonlinear magnetotail particle dynamics, *Geophys. Res. Lett.*, **17**, 2237 - 2240, 1990.

Chen, J., H. G. Mitchell and P. J. Palmadesso, Differential memory in the tri-linear model magnetotail, *J. Geophys. Res.*, **95**, 15,141-15,156, 1990.

Chen, J. and P. J. Palmadesso, Chaos and nonlinear dynamics of single-particle orbits in a magnetotaillike magnetic field, *J. of Geophys. Res.*, **91**, 1499-1508, 1986.

Chen, J., J. L. Rexford and Y. C. Lee, Fractal boundaries in magnetotail particle dynamics, *Geophys. Res. Lett.*, **17**, 1049 - 1052, 1990.

Cowley, S. W. H., A note on the motion of charged particles in one-dimensional magnetic current sheets, *Planet. and Space Sci.*, 26, 539-545, 1978.

Cowley, S. W. H., The effect of pressure anisotropy on the equilibrium structure of magnetic current sheets., *Planet. Space Sci.*, **26**, 1037 - 1061, 1978.

Daniels, W. E., Jr., GLSWS - General least squares with statistics, University of Maryland Technical Report 579, College Park, MD, 1966.

Donovan, E. F. and G. Rostoker, Internal Consistency of the Tsyganenko Magnetic Field Model and the Heppner-Maynard Empirical Model of the Ionospheric Electric Field Distribution., *Geophys. Res. Lett.*, **18**, 1043 - 1046, 1991.

Doxas, I., W. Horton, K. Sandusky, T. Tajima and R. Steinolfson, Numerical Study of the Current Sheet and Plasma Sheet Boundary Layer in a Magnetotail Model, *J. of Geophys. Res.*, **95**, 12033 - 12043, 1990.

Dragt, A. J., Trapped Orbits in a Magnetic Dipole Field, *Rev. of Geophys.*, 255 - 297, 1965.

Dragt, A. J. and J. M. Finn, Insolubility of trapped particle motion in a magnetic dipole field, *J. of Geophys. Res.*, **81**, 2327-2340, 1976.

Eastwood, J. W., Consistency of fields and particle motion in the 'Speiser' model of the current sheet, *Planet. and Space Sci.*, **20**, 1555-1568, 1972.

Eastwood, J. W., The warm current sheet model, and it's implications on the temporal behaviour of the geomagnetic tail, *Planet. and Space Sci.*, **22**, 1641-1668, 1974.

Eastwood, J. W., Some properties of the current sheet in the geomagnetic tail, *Planet. and Space Sci.*, **23**, 1-14, 1975.

Fairfield, D. H., On the average configuration of the geomagnetic tail, *J. of Geophys. Res.*, **84**, 1950-1958, 1979.

Fairfield, D. H., A statistical determination of the shape and position of the geomagnetic neutral sheet, *J. Geophys. Res.*, **85**, 775-780, 1980.

Fairfield, D. H., The magnetic field of the equatorial magnetotail from 10 to 40 R_E, *J. Geophys. Res.*, **91**, 4238-4244, 1986.

Fairfield, D. H., M. H. Acuna, L. J. Zanetti and T. A. Potemra, The magnetic field of the equatorial magnetotail: AMPTE/CCE observations at R <8.8 Re, *J. of Geophys. Res.*, **92**, 7432 - 7442, 1987.

Fetter, A. L. and J. D. Walecka, Theoretical mechanics of particles and continua, 570 pp., McGraw-Hill, Inc., New York, 1980.

Frank, L. A., Plasmas in the Earth's magnetotail, *Space Sci. Rev.*, **42**, 211-240, 1985.

Frank, L. A., C. Y. Huang, and T. E. Eastman, Currents in the Earth's magnetotail, in *Magnetospheric Currents*, T. A. Potemra, editor, pp. 147-157, American Geophysical Union, Washington, DC, 1984.

Fridman, M. and J. Lemaire, Relationship between auroral electrons fluxes and field aligned electric potential difference, *J. of Geophys. Res.*, **85**, 664-670, 1980.

Gosling, J. T., D. J. McComas, M. F. Thomsen, S. J. Bame, and C. T. Russell, The warped neutral sheet and plasma sheet in the near-Earth geomagnetic tail, *J. Geophys. Res.*, **91**, 7093-7099, 1986.

Gray, P. C. and L. C. Lee, Particle pitch angle diffusion due to nonadiabatic effects in the plasma sheet, *J. of Geophys. Res.*, **87**, 7445-7452, 1982.

Hada, T., A. Nishida, T. Terasawa, and E. W. Hones, Jr., Bi-directional electron pitch angle anisotropy in the plasma sheet, *J. Geophys. Res.*, **86**, 11,211-11,224, 1981.

Harris, E. G., On a plasma sheath separating regions of oppositely directed magnetic field, *Il Nuovo Cimento*, **23**, 115-121, 1962.

Heppner, J. P., and N. C. Maynard, Empirical high-latitude electric field models, *J. Geophys. Res.*, **92**, 4467-4489, 1987.

Hesse, M. and J. Birn, Three-dimensional MHD modeling of magnetotail dynamics for different polytropic indices, *J. Geophys. Res.*, **97**, 3965-3976, 1992.

Hockney, R. W. and J. W. Eastwood, Computer simulation using particles, 540 pp., IOP Publishing Ltd, New York, 1988.

Holland, D. L. and J. Chen, Effects of collisions on the nonlinear particle dynamics in the magnetotail, *Geophys. Res. Lett.*, **18**, 1579 - 1582, 1991.

Holland, D. L. and J. Chen, On chaotic conductivity in the magnetotail, *Geophys. Res. Lett.*, **19**, 1231 - 1234, 1992.

Holland, D. L. and J. Chen, Self-consistent current sheet structures in the quiet-time magnetotail, *Geophys. Res. Lett.*, **20**, 1775 - 1778, 1993.

Horton, W., C. Liu, J. Hernandez and T. Tajima, Stochastic mixing of protons from chaotic orbits in the nightside geomagnetosphere, *Geophys. Res. Lett.*, **18**, 1575 - 1578, 1991.

Horton, W. and T. Tajima, Collisionless Conductivity and Stochastic Heating in the Geomagnetic Tail, *J. of Geophys. Res.*, **96**, 15811 - 15829, 1991.

Horton, W. and T. Tajima, Transport from chaotic orbits in the geomagnetic tail., *Geophys. Res. Lett.*, **18**, 1583 - 1586, 1991.

Huang, C. Y. and L. A. Frank, A statistical study of the central plasma sheet: implications for substorm models, *Geophys. Res. Lett.*, **13**, 652-655, 1986.

Huang, C. Y. and L. A. Frank, Reply to Cattell and Elphic, *Geophys. Res. Lett.*, **14**, 776 - 778, 1987.

Huang, C. Y., and L. A. Frank, Magnitude of B_z in the neutral sheet of the magnetotail, *J. Geophys. Res.*, **99**, 73-82, 1994a.

Huang, C. Y. and L. A. Frank, A Statistical Survey of the Central Plasma Sheet, *J. of Geophys. Res.*, **99**, 83 - 95, 1994.

Hurricane, O. A., R. Pellat, and F. V. Coroniti, A new approach to low-frequency "MHD-like" waves in magnetospheric plasmas, *J. Geophys. Res.*, **100**, 19,421-19,428, 1995.

Ichimaru, S., <u>Basic principles of plasma physics, a statistical approach</u>, 324 pp., W. A. Benjamin, Inc., Advanced Book Program, Reading, MA, 1973.

Jackson, J. D., <u>Classical Electrodynamics</u>, 848 pp., John Wiley and Sons, Inc., New York, 1975.

Kan, J. R., On the Structure of the Magnetotail Current Sheet, *J. of Geophys. Res.*, **78**, 3773-3781, 1973.

Kan, J. R., Tail-like reconfiguration of the plasma sheet during the substorm growth phase, *Geophys. Res. Lett.*, **17**, 2309 - 2312, 1990.

Kan, J. R. and S.-I. Akasofu, Electrodynamics of Solar Wind-Magnetosphere-Ionosphere Interactions, *Geophys. Res. Lett.*, **17**, 83 - 108, 1989.

Kan, J. R., W. Sun and W. Baumjohann, A hybrid equation of state for the quasi-static central plasma sheet, *Geophys. Res. Lett.*, **19**, 421 - 424, 1992.

Kaufmann, R. L., Substorm Currents: Growth Phase and Onset, *J. of Geophys. Res.*, **92**, 7471-7486, 1987.

Kaufmann, R. L. and D. J. Larson, Electric Field Mapping and Auroral Birkeland Currents, *J. of Geophys. Res.*, **94**, 15307-15319, 1989.

Kaufmann, R. L., D. J. Larson, P. Beidl and C. Lu, Mapping and Energization in the Magnetotail 1. Magnetospheric Boundaries, *J. of Geophys. Res.*, **98**, 9307-9320, 1993.

Kaufmann, R. L., D. J. Larson and C. Lu, Mapping and Distortion of Auroral Structures in the Quiet Magnetosphere, *J. of Geophys. Res.*, **95**, 7973-7994, 1990.

Kaufmann, R. L., D. J. Larson and C. Lu, Mapping and Energization in the Magnetotail 2. Particle Acceleration, *J. of Geophys. Res.*, **98**, 9321-9333, 1993.

Kaufmann, R. L. and C. Lu, Cross-Tail Current: Resonant Orbits, *J. of Geophys. Res.*, **98**, 15447 - 15465, 1993.

Kiessling, M., Existence and uniqueness of the pressure profile p(A) of a current-carrying quasineutral equilibrium plasma, *J. Math Phys.*, **29**, 1258 - 1263, 1988.

Kiessling, M. and K. Schindler, Analytical Stability Analysis for a Two-Dimensional Self-Consistent Magnetotail Model by Use of Statistical Mechanics, *J. of Geophys. Res.*, **92**, 5795 - 5806, 1987.

Kiessling, M. and H. J. Ziegler, A Theory of Self-Consistent Two-Dimensional Tail Equilibria for Quasineutral e⁻ H⁺ O⁺, *J. of Geophys. Res.*, **94**, 261-271, 1988.

Kistler, L. M., W. Baumjohann, T. Nagai and E. Möbius, Superposed Epoch Analysis of Pressure and Magnetic Field Configuration Changes in the Plasma Sheet, *J. of Geophys. Res.*, **98**, 9249 - 9258, 1993.

Kistler, L. M., E. Möbius, W. Baumjohann, G. Paschmann and D. C. Hamilton, Pressure Changes in the Plasma Sheet During Substorm Injections, *J. Geophys. Res.*, **97**, 2, 1992.

Kistler, L. M., E. Möbius, B. Klecker, G. Gloeckler, F. M. Ipavich and D. C. Hamilton, Spatial Variations in the Suprathermal Ion Distributions During Substorms in the Plasma Sheet, *J. of Geophys. Res.*, **95**, 18,871 - 18,885, 1990.

Koonin, S. E. and D. C. Meredith, <u>Computational Physics - Fortran Version</u>, 635 pp., Addison-Wesley Publishing Company, Redwood City, CA, 1990.

Krall, N. A., and A. W. Trivelpiece, <u>Principles of Plasma Physics</u>, p 119, McGraw-Hill Book Co., New York, 1973.

Landau, L. D., E. M. Lifshitz and L. P. Pitaevskii, <u>Electrodynamics of Continuous Media</u>, 460 pp., Pergamon Press, Inc., Tarrytown, NY, 1993.

Lembege, B. and R. Pellat, Stability of a thick two-dimensional quasineutral sheet, *Physics of Fluids*, **25**, 1995-2004, 1982.

Li, X. and T. W. Speiser, An Estimation of the Electric Field in the Magnetotail Current Sheet Using the Observed Energetic Ion Bulk Flow, *Geophys. Res. Lett.*, **18**, 1967 - 1970, 1991.

Lifshitz, E. M. and L. P. Pitaevskii, <u>Physical Kinetics</u>, 452 pp., Pergamon Press, Inc., Tarrytown, NY, 1993.

Liu, W. W., An explicit bounce average calculation of adiabatic particle drifts, *J. of Geophys. Res.*, **99**, 2383 - 2386, 1994.

Longmire, C. L., <u>Elementary Plasma Physics</u>, 296 pp., John Wiley & Sons, New York, 1963.

Lu, C., <u>Study of Cross-Tail Current Carriers in Magnetotail</u>, Ph. D. Thesis, University of New Hampshire, 1993.

Lui, A. T. Y., D. C. Hamilton, Radial profiles of quiet time magnetospheric parameters, *J. Geophys. Res.*, **97**, A12, 19325-19332, 1992.

Lyons, L. R., Electron energization in the geomagnetic tail current sheet, *J. of Geophys. Res.*, **89**, 5479-5487, 1984.

Lyons, L. R. and T. W. Speiser, Evidence for current sheet acceleration in the geomagnetic tail, *J. of Geophys. Res.*, **87**, 2276-2286, 1982.

Lyons, L. R. and T. W. Speiser, Ohm's Law for a Current Sheet, *J. of Geophys. Res.*, **90**, 8543-8546, 1985.

Martin, R. F. J., Chaotic Particle Dynamics Near a Two-Dimensional Magnetic Neutral Point With Application to the Geomagnetic Tail, *J. of Geophys. Res.*, **91**, 11985 - 11992, 1986.

Martin, R. F. J., The effect of plasma sheet thickness on ion acceleration near a magnetic neutral line, in Ion Accleration in the Magnetosphere and Ionosphere, pp 141 - 145, 1986.

Martin, R. F. J., A Predicted Energetic Ion Signature of a Neutral Line in the Geomagnetic Tail, *J. of Geophys. Res.*, **93**, 11521 - 11526, 1988.

Martin, R. F. J., D. F. Johnson and T. W. Speiser, The energetic ion signature of an O-type neutral line in the geomagnetic tail, SPI Conference Proceedings and Reprint Series, **11**, 203 - 206, 1991.

Martin, R. F. J. and T. W. Speiser, Nonlinear dynamics of the neutral line Hamiltonian, SPI Conference Proceedings and Reprint Series, **11**, 311 - 334, Scientific Publishers, Inc., 1991.

Maynard, N. C., F. D. Williams, W. J. Burke, Mapping ionospheric convection patterns to the magnetosphere, *J. Geophys. Res.*, **100**, A2, 1713-1721, 1995.

McComas, D. J., C. T. Russell, R. C. Elphic and S. J. Bame, The near-earth cross-tail current sheet: detailed ISEE 1 and 2 case studies, *J. of Geophys. Res.*, **91**, 4287-4301, 1986.

Mitchell, D. G., D. J. Williams, C. Y. Huang, L. A. Frank and C. T. Russell, Current carriers in the near-earth cross-tail current sheet during substorm growth phase, *Geophys. Res. Lett.*, **17**, 583 - 586, 1990.

Möbius, E., Energetic particles in the environment of the Earth's magnetosphere, *Journal of Atmospheric and Terrestrial Physics,* **52**, 1169-1184, 1990.

Möbius, E., Sources and Acceleration of Energeric Particles in Planetary Magnetospheres, *The Astrophysical Journal Supplemental Series*, **90**, 521 - 530, 1994.

Nakamura, M., G. Paschmann, W. Baumjohann and N. Skopke, Ion Distributions and Flows in and Near the Plasma Sheet Boundary Layer, *J. of Geophys. Res.*, **97**, 1449 -

1460, 1992.

Nicholson, D. R., Plasma theory, 292 pp., John Wiley & Sons, Inc., New York, 1983.

Northrop, T. G., *Rev. of Geophys.*, Adiabatic Charged-Particle Motion, **1**, 283 - 304, 1963.

Northrop, T. G., The Adiabatic Motion of Charged Particles, 109 pp., Interscience Publishers, New York, 1963.

Ogino, T., R. J. Walker, and M. Ashour-Abdalla, A global magnetohydrodynamic simulation of the response of the magnetosphere to a northward turning of the interplanetary magnetic field, *J. Geophys. Res.*, **99**, 11,027-11,042, 1994.

Olsen, W. P. (Ed.), *Quantitative Modeling of Magnetospheric Processes*, 655 pp, American Geophysical Union, Washington, D. C., 1979.

Parker, E. N., Newtonian development of the Dynamical Properties of Ionized Gases of Low Density, *Physical Review*, **107**, 924-933, 1957.

Parks, G. K., Physics of Space Plasmas, 538 pp., Addison-Wesley Publishing Company, Redwood City, CA, 1991.

Paterson, W. R., L. A. Frank, S. Kokubun, T. Yamamoto, and R. P. Lepping, Geotail observations of magnetospheric currents, (abstract), *EOS Trans. AGU*, **76**, F485, 1995.

Peredo, M. and D. P. Stern, On the position of the near-Earth neutral sheet: A comparison of magnetic model predictions with empirical formulas, *J. of Geophys. Res.*, **96**, 19521-19524, 1991.

Pockels, F., *Uber die partielle differentialgleichung $\Delta u + k^2 u = 0$ und deren auftreten in der mathematischen physik*, 340 pp., Druck und Verlag Von B. G. Teubner, Leipzig, 1891.

Press, W. A., S. A. Teukolsky, W. T. Vetterling and B. P. Flannery, Numerical recipes in FORTRAN: the Art of Scientific Computing, 963 pp., Cambridge University Press, New York, 1992.

Pritchett, P. L. and F. V. Coroniti, Formation and Stability of the Self-Consistent One-Dimensional Tail Current Sheet, *J. of Geophys. Res.*, **97**, 16773 - 16787, 1992.

Pritchett, P. L. and F. V. Coroniti, Interaction of reflected ions with the firehose marginally stable current sheet: Implications for plasma sheet convection, *Geophys. Res. Lett.*, **19**, 1631 - 1634, 1992.

Pritchett, P. L., F. V. Coroniti, R. Pellat and H. Karimabadi, Collisionless reconnection in two-dimensional magnetotail equilibria, *J. of Geophys. Res.*, **96**, 11,523-1,538, 1991.

146

Pulkkinen, T. I., D. N. Baker, D. H. Fairfield, R. J. Pellinen, J.S. Murphree, R. D. Elphinstone, R. L. McPherron, J. F. Fennell, R. E. Lopez, and T. Nagai, Modeling the growth phase of a substorm using the Tsyganenko model and multi-spacecraft observations: CDAW-9, *Geophys. Res. Lett.*, **18**, 1963-1966, 1991.

Pulkkinen, T. I., D. N. Baker, R. J. Pellinen, J. Büchner, H. E. J. Koskinen, R. E. Lopez, R. L. Dyson, and L. A. Frank, Particle scattering and current sheet stability in the geomagnetic tail during the substorm growth phase, *J. Geophys. Res.*, **97**, 19,283-19,297, 1992.

Pulkkinen, T. I., D. N. Baker, D. G. Mitchell, R. L. McPherron, C. Y. Huang, and L. A. Frank, This current sheets in the magnetotail during substorms: CDAW 6 revisited, *J. Geophys. Res.*, **99**, 5793-5803, 1994.

Rich, F. J., V. M. Vasyliunas and R. A. Wolf, On the Balance of Stresses in the Plasma Sheet, *J. of Geophys. Res.*, **77**, 4670 - 4676, 1972.

Robinson, R. M., R. R. Vondrak, K. Miller, T. Dabbs and D. Hardy, On Calculating Ionospheric Conductances From the Flux and Energy of Precipitating Electrons, *J. of Geophys. Res.*, **92**, 2565 - 2569, 1987.

Rostoker, G., and S. Skone, Magnetic flux mapping considerations in the auroral oval and the Earth's magnetotail, *J. Geophys. Res.*, **98**, 1377-1384, 1993.

Sachsenweger, D., M. Scholer and E. Mobius, Test particle acceleration in a magnetotail reconnection configuration, *J. of Geophys. Res.*, **16**, 1027-1030, 1989.

Sanny, J., R. L. McPherron, C. T. Russell, D. N. Baker, T. I. Pulkkinen, and A. Nishida, Growth-phase thinning of the near-Earth current sheet during the CDAW 6 substorm, *J. Geophys. Res.*, **99**, 5805-5816, 1994.

Schindler, K., A self-consistent theory of the tail of the magnetosphere, in Earth's Magnetospheric Processes, edited by B. M. McCormac, pp 200 - 209, D. Reidel Publishing Company, Dordrecht, Holland, 1972.

Schindler, K., Plasma and fields in the magnetospheric tail, *Space Sci. Rev.*, **17**, 589 - 614, 1975.

Schindler, K., Theories of tail structures, *Space Sci. Rev.*, **23**, 365 - 374, 1979.

Schwarzschild, M., A numerical model for a triaxial stellar system in dynamical equilibrium, *The Astrophysical Journal*, **232**, 236-247, 1979.

Sergeev, V. A., Penetration of the B_y-component of the interplanetary magnetic field (IMF) into the tail of the magnetosphere, *Geomag. and Aeronomy*, **27**, 528-531, 1987.

Sergeev, V. A., D. G. Mitchell, C. T. Russell, and D. J. Williams, Structure of the tail plasma/current sheet at ~11 R_E and its changes in the course of a substorm, *J. Geophys. Res.*, **98**, 17,345-17,365, 1993.

Sonnerup, B. U. Ö., Adiabatic particle orbits in a magnetic null sheet, *J. of Geophys. Res.*, **76**, 8211-8222, 1971.

Speiser, T. W., Particle trajectories in model current sheets 1. Analytical solutions, *J. of Geophys. Res.*, **70**, 4219-4226, 1965.

Speiser, T. W., Particle trajectories in model current sheets 2. Applications to auroras using a geomagnetic tail model, *J. of Geophys. Res.*, **72**, 3919-3932, 1967.

Speiser, T. W., On the Uncoupling of Parallel and Perpendicular Particle Motion in a Neutral Sheet, *J. of Geophys. Res.*, **73**, 1112 - 1113, 1968.

Speiser, T. W., Kinetic aspects of tail dynamics: Theory and simulation, in <u>Monograph on Magnetotail Physics</u>, Johns Hopkins University Press, 1986.

Speiser, T. W., Plasma Sheet Theories, in <u>AGU Monograph on Magnetosphere Ionosphere Plasma Models</u>, 1987.

Speiser, T. W., Processes in the magnetotail neutral sheet, *Physica Scripta*, **T18**, 119-127, 1987.

Speiser, T. W., Particle dynamics in the Earth's magnetospheric tail, *Geofisica Internacional*, **30**, 219 - 224, 1991.

Speiser, T. W., Particle motion in the tail current sheet, *Adv. Space Res.*, **11**, 151 - 159, 1991.

Speiser, T. W., P. B. Dusenbery, J. R. F. Martin and D. J. Williams, Particle orbits in magnetospheric current sheets: Accelerated flows, neutral line signature, and transistions to chaos, in <u>Modeling Magnetospheric Plasma Processes</u>, pp 71 - 79, American Geophysical Union, 1991.

Speiser, T. W. and R. F. M. Jr, Energetic Ions as Remote Probes of X Type Neutral Lines in the Geomagnetic Tail, *J. of Geophys. Res.*, **97**, 10775 - 10785, 1992.

Speiser, T. W. and L. R. Lyons, Comparison of an analytical approximation for particle motion in a current sheet with precise numerical calculations, *J. of Geophys. Res.*, **89**, 147-158, 1984.

Spence, H. E., M. G. Kivelson and R. J. Walker, Comparison of Field Aligned Currents at Ionospheric and Magnetospheric Altitudes, *Adv. Space Res.*, **8**, 343 - 346 (9), 1988.

Spitzer, L. J., Physics of Fully Ionized Gases, 170 pp., Interscience Publishers, New York, 1962.

Stern, D. P., Representation of Magnetic Fields in Space, *Reviews of Geophysics and Space Physics*, **14**, 199-214, 1976.

Stern, D. P., Adiabatic Particle Motion in a Nearly Drift-Free Magnetic Field: Application to the Geomagnetic Tail, *J. of Geophys. Res.*, **83**, 1079 - 1088, 1978.

Stern, D. P. and P. Palmadesso, Drift-Free Magnetic Geometries in Adiabatic Motion, *J. of Geophys. Res.*, **80**, 4244-4248, 1975.

Stern, D. P. and N. A. Tsyganenko, Uses and Limitations of the Tsyganenko Magnetic Field Models, *Eos, Transactions, American Geophysical Union*, **73**, 489, 493-494, 1992.

Sugiura, M., A fundamental magnetosphere-ionosphere coupling mode involving field-aligned currents as deduced from DE-2 observations, *Geophys. Res. Lett.*, **11**, 877 - 880, 1984.

Tajima, T., Computational Plasma Physics: With Applications to Fusion and Astrophysics, 503 pp., Addison-Wesley, Reading, MA, 1989.

Toichi, T., Two-Dimensional Equilibrium Solution of the Plasma Sheet and its Applications to the Problem of the Tail Magnetosphere., *Cosmic Electrodynamics*, **3**, 81-96, 1972.

Tsyganenko, N. A., Global quantitative models of the geomagnetic field in the cislunar magnetosphere for different disturbance levels, *Planetary and Space Science*, **35**, 1347-1358, 1987.

Tsyganenko, N. A., A magnetospheric magnetic field model with a warped tail current sheet, *Planetary and Space Science*, **37**, 5-20, 1989.

Tsyganenko, N. A., On the re-distribution of the magnetic field and plasma in the near nightside magnetosphere during a substorm growth phase, *Planetary and Space Science*, **37**, 183-192, 1989.

Tsyganenko, N. A., Quantitative models of the magnetospheric magnetic field: methods and results, *Space Science Reviews*, **54**, 75 - 186, 1990.

Tsyganenko, N. A. and A. V. Usmanov, Determination of the magnetospheric current system parameters and development of experimental geomagnetic field models based on data from IMP and HEOS satellites, *Planetary and Space Science*, **30**, 985-998, 1982.

Usadi, A., R. A. Wolf, M. Heinemann, and W. Horton, Does chaos alter the ensemble averaged drift equations?, to be published, *J. Geophys. Res.*, **101**, 1996.

Voigt, G.-H. and R. A. Wolf, Quasi-Static Magnetospheric MHD Processes and the "Ground State" of the Magnetosphere, *Rev. of Geophys.*, **26**, 823 - 843, 1988.

Walker, G. W., On the distribution of a gas in an electrical field, *London, Edinburgh and Dublin Philosophical Magazine and Journal of Science*, **44**, Series 5, 529-538, 1900.

Walker, G. W., On some problems in the distribution of a gas, in *Festschrift Ludwig Boltzmann Gewidmet zum sechzigsten geburtstage 20. Februar 1904.*, Verlag Von Johann Ambrosius Barth, Leipzig, 1904.

Walker, G. W., Some problems illustrating the forms of nebulae, *Proc. Roy. Soc.*, **91**, 410-420, 1915.

Whipple, E. C., T. G. Northrop and T. J. Birmingham, Adiabatic theory in regions of strong field gradients, *J. of Geophys. Res.*, **91**, 4149-4156, 1986.

Whipple, E. C., M. Rosenberg and M. Brittnacher, Magnetotail acceleration using generalized drift theory: A kinetic merging scenario, *Geophys. Res. Lett.*, **17**, 1045 - 1048, 1990.

Winglee, R. M., and R. S. Steinolfson, Energy storage and dissipation in the magnetotail during substorms 1. Particle simulations, *J. Geophys. Res.*, **98**, 7519-7535, 1993.

Winglee, R. M., Non-MHD influences on the magnetospheric current system, *J. Geophys. Res.*, **99**, A7, 13437-13454, 1994.

Wolf, R. A. and D. H. Pontius, Jr., Particle drift in the earth's plasma sheet, *Geophys. Res. Lett.*, **20**, 1455-1458, 1993.

Zwingmann, W., Self-consistent magnetotail theory: Equilibrium structures including arbitrary variation along the tail axis, *J. of Geophys. Res.*, **88**, 9101-9108, 1983.

Zwingmann, W., Particle simulation of magnetic reconnection in collision-free plasma sheets, in *Proceedings of an International Workshop on Reconnection in Space Plasma, held in Potsdam, GDR, 5-9 September 1988*, **2**, 67-70, European Space Agency, Potsdam, GDR, 1988.

Zwingmann, W., J. Wallace, K. Schindler and J. Birn, Particle Simulation of Magnetic Reconnection in the Magnetotail Configuration, *J. of Geophys. Res.*, **95**, 20877-20888, 1990.

Appendix A: MACROSCOPIC VARIABLES OF A PLASMA

The subscript s designates particle species. The subscripts α and β are coordinate indices. The derivation of these quantities can be found in [*Ichimaru*, 1973; *Krall and Trivelpiece*, 1986; *Nicholson*, 1992; *Parks*, 1991].

Number Density

$$n_s(\mathbf{x}) = \int f_s(\mathbf{v}) d^3 v$$

Mass Density

$$\rho_{mass}(\mathbf{x}) = \sum_s m_s \int f_s(\mathbf{v}) d^3 v$$

Charge Density

$$\rho_s(\mathbf{x}) = q_s \int f_s(\mathbf{v}) d^3 v$$

Bulk Velocity (convection velocity)

$$u_{s,\alpha}(\mathbf{x}) = \frac{1}{n_s(\mathbf{x})} \int v_\alpha f_s(\mathbf{v}) d^3 v$$

Bulk Flow Tensor

$$U_{s,\alpha\beta}(\mathbf{x}) = m_s n_s u_{s,\alpha} u_{s,\beta}$$

Current Density

$$\mathbf{j}_{s,\alpha}(\mathbf{x}) = q_s \int v_\alpha f_s(\mathbf{v}) d^3 v$$

Heat Flux Vector

$$\mathbf{Q}_{s,\alpha}(\mathbf{x}) = \frac{m_s}{2} \int \sum_{\beta=1}^{3} (v_{s,\beta} - u_{s,\beta})^2 (v_{s,\alpha} - u_{s,\alpha}) f_s(\mathbf{v}) d^3 v$$

Pressure Tensor

$$P_{s,\alpha\beta}(\mathbf{x}) = m_s \int (v_{s,\alpha} - u_{s,\alpha})(v_{s,\beta} - u_{s,\beta}) f_s(\mathbf{v}) d^3 v$$

Momentum Tensor, where $\Pi_{s,\alpha\beta} = P_{s,\alpha\beta} + U_{s,\alpha\beta}$

$$\Pi_{s,\alpha\beta}(\mathbf{x}) = m_s \int v_\alpha v_\beta f_s(\mathbf{v}) d^3 v$$

Computing Environment of the UNH Space Plasma Physics Group

RS/6000 Model 320

(1) 32 MB Memory-Board

(1) 16 MB Memory Board

(1) 1.6 GB HD

19" Color Monitor

sppibm.unh.edu

CD ROM

1/4" Tape Drive

IBM 10P laser printer 600 dpi

RS/6000 Model 320

(1) 32 MB Memory Board

(1) 320 MB HD

(1) 2.4 GB HD

19" B&W Monitor (8508)

space.unh.edu

Macintosh
Quadra 700
20MB Memory
400 MB HD
16" Color monitor
sppmac.unh.edu

Apple CD ROM

LaCie 1200 dpi Color Scanner

SCSI

Ethernet

To World

SGI Indigo^2

(1) 128 MB Memory

(1) 2.0 & 9.0 GB HDs'

(1) 21 MB Floptical Drive

20" Color monitor

CD ROM

2 GB, 4mm DAT

Tektronix Phaser III color printer

DAT - Digital Audio Tape
GB - Gigabyte
HD - Hard Disk Drive
MB - Megabyte
SCSI - Small Computer System Interface

Appendix C: SOFTWARE AVAILABILITY

Internet Location

Machine - sppibm.unh.edu

World Wide Web Location:

- Open the following URL using Mosaic, Netscape, or any other browser:
  http://sppibm.unh.edu:1963/Welcome.html

In the event that no direct computer access is available please write to:

University of New Hampshire
Department of Physics
College of Engineering and Physical Science
DeMerritt Hall
Durham, New Hampshire 03824-3568

Physics Department Phone: (603) 862-1950
Professor Richard Kaufmann: (603) 862-2759
EMAIL: Dick.Kaufmann@unh.edu
Space Plasma Physics Lab: (603) 862-2780

This information was valid as of May, 1996.

Test Particle Numerical Experiment Framework				
partrj.f Particle Tracing	magfld.f Field Line Maker	slices.f	bigfilter.f	Assorted Postpro- cessing codes
PARCOM.FOR	EWBCOM.FOR MAGCOM.FOR	PROCOM.FOR	BIGCOM.FOR	PARCOM.FOR & BIGCOM.FOR
Shared subroutines in share_lib.a				
CONSTS.FOR (Radius of Earth, π, 2π, fundamental charge, proton rest mass, Boltzmann's constant, etc.)				
Field Access Subroutines: do_bfield(x,y,z), do_efield(x,y,z), and do_afield(x,y,z) Where (x,y,z) is in either Earth radii (Re) or meters				
BEVALS.FOR Provides unified access to all field models Bx, By, Bz are in Both Tesla and nanoTesla Ex, Ey, Ez are in millivolts/meter and Volts/meter Ax, Ay, Az are in Webers/meter				
ALLCOM.FOR				
T89COM.FOR	HARPOL.FOR	BRDCOM.FOR	SHEETC.FOR	BASICS.FOR
Tsyganenko 1989 Model	Harris Type	Beard's Model	Simple Sheet model	Miscellaneous (Dipole, Ring)

Appendix E: SUMMARY OF DATA FILE TYPES

File suffixes are in **bold**, *programs* and *subroutines* are italicized.

if; The "Initial Final" file summarizes the particles' injection, forward and backward time integration final step as well as some magnetic field model information. This datafile is generated by subroutine *write_if* which is called by *partrj*.

JLRE	ERRMAX			This is the datafile header. The 'o' subscript indicates a constant quantity.
Bxo	Byo	Bzo	[nT]	
Exo	Eyo	Ezo	[mV/m]	
xo	yo	zo	[RE]	
Begin::	W	PA	Phase	These nine lines summarize a single particle. For every particle traced an entry similar to this is appened to the 'if' datafile.
xbegin	ybegin	zbegin		
Vx	Vy	Vz		
Inject::	W	PA	Phase	
Vx	Vy	Vz		
End::	W	PA	Phase	
Xend	Yend	Zend		
Vx	Vy	Vz		
CPU	Tparticle	Kappa	(Un)Trapped	

rvt; Saves the position, velocity, and time for an entire particle trajectory.

x, R_E	y, R_E	z, R_E	v_x, m/s	v_y, m/s	v_z, m/s	time, sec

sos; Saves information needed to generate surface of section plots for specified planes.

x, R_E	y, R_E	z, R_E	v_x, m/s	v_y, m/s	v_z, m/s	time, sec

155

rkt; Saves the (x,y, z=0) position, energy, kappa, and time for an entire particle trajectory.

x, R_E	y, R_E	Energy, keV	$\kappa = \sqrt{R_{min}/\rho_{max}}$	time, sec

run; During runtime this data is output to the terminal at the beginning of each new particle tracing and can be dumped to a datafile.

Energy, keV	Particle Pitch Angle	Particle Phase Angle

nj; Saves j_x, j_z, and number density for trapped and untrapped particles. This is an older format that maintains backward compatibility with *Lu* [1993]. It is useful for 1-D models and for comparison with the results of the integration of $f(v)$ method.

njp; All moments of the distribution function are saved in this file.

Datafile Header (Done once at the top of the datafile)

Winject	Wminimum	Wmaximum	charge	species mass	
B_x, nT	B_y, nT	B_z, nT	E_x, mV/m	E_y, mV/m	E_z, mV/m
# of particles	# trapped	# untrapped	n_o, m^3	v_{max}, m/sec	afact, m^{-3}s^{-1}
x gridmin	x gridmax	y gridmin	y gridmax	z gridmin	z gridmax
# of xboxes, x foldflag, dx		# of yboxes, y foldflag, dy		# of zboxes, z foldflag, dz	

X_{box} number		Y_{box} number		Z_{box} number			
	x, R_E	y, R_E	z, R_E	boxave	n, m^3	θ_b	ϕ_b
		Q_x	Q_y	Q_z	Jm^{-2}s^{-1}		
		u_x, m/s	u_y, m/s	u_z, m/s	j_x, A/m^2	j_y, A/m^2	j_z, A/m^2
		Π_{xx}	Π_{xy}	Π_{xz}	Π_{yy}	Π_{yz}	Π_{zz}
		P_{xx}	P_{xy}	P_{xz}	P_{yy}	P_{yz}	P_{zz}

fvc; This file contains all the distribution functions, $f(\mathbf{v})$, for each cell in the simulation grid. The c in the filename suffix indicates that cartesian coordinates were used. The distribution functions are generated by the *partrj* program and the subroutine *write_df* writes this data as well as **fv** ($f(v_{\parallel}, v_{\perp})$) and **fap** ($f(\alpha, \varphi)$) datafiles.

Datafile Header (done once at the top of the datafile), same as **njp** header.								
Do for all X boxes								
	Do for all Y boxes							
		X_{box}	Y_{box}	Z_{box}	nvcube	nvcube	nvcube	
		na	natr	naut	btusav	charge	mass	dz	velmax
		Do for all Z boxes						
			x, R_E	y, R_E	z, R_E	θ_b	ϕ_b	
		end do						
		Do for all V_x, V_y, V_z boxes						
			Do for all Z boxes					
				$f(\mathbf{v})$				
			end do					
		end do						
	end do							
end do								

nvcube - Number of velocity boxes for each side of the velocity cube

na - Total number of particles traced $na = naut + natr$

natr - Number of *trapped* particles.

naut - Number of *untrapped* particles.

θ_b & ϕ_b - The polar and azimuthal angles between the z axis and **B** (in radians).

ntp_o; Parallel and perpendicular temperatures and pressures computed by program *bigfilter* and subroutine *filter_njp* from njp datafiles. The temperature is calculated using

$P = nT$ where temperature is in eV.

x, R_E	y, R_E	z, R_E	n, m^3	$T_{\parallel}$, eV	$T_{\perp}$, eV	T, eV	$P_{\parallel}$, Pa	$P_{\perp}$, Pa	P, Pa

njp_o; Number and current density extracted from **njp** datafile by *bigfilter* and *filter_njp*.

x, R_E	y, R_E	z, R_E	n, m^3	j_x, A/m^2	j_y, A/m^2	j_z, A/m^2

pten_o; Extracted from **njp** datafile by subroutine *filter_njp*. Note that θ_b and ϕ_b are in degrees and all P_{ij} are in Pascals.

x, R_E	y, R_E	z, R_E	θ_b	ϕ_b	P_{xx}	P_{xy}	P_{xz}	P_{yy}	P_{yz}	P_{zz}

qflux_o; Heat flux, extracted from **njp** datafile by *bigfilter* and subroutine *filter_njp*.

x, R_E	y, R_E	z, R_E	Q_x, $Jm^{-2}s^{-1}$	Q_y, $Jm^{-2}s^{-1}$	Q_z, $Jm^{-2}s^{-1}$	$|Q|$, $Jm^{-2}s^{-1}$

vbulk_o; Convection velocity extracted from **njp** datafile by subroutine *filter_njp*.

x, R_E	y, R_E	z, R_E	u_x, m/s	u_y, m/s	u_z, m/s	$|u|$, m/s

betafire; Computed using **njp** data by subroutine *filter_njp*.

x, R_E	y, R_E	z, R_E	Plasma Beta	firehose	$P_{\parallel}/P_{\perp}$	$T_{\parallel}/T_{\perp}$

f_*, where '*' is a wildcard and could be *em, inertial, JexB, JixB, mom, part*, etc.. These files represent the various forces that can be calculated for the plasma.

x, R_E	y, R_E	z, R_E	$|f|$	f_x	f_y	f_z	$f_{||x}$	$f_{||y}$	$f_{||z}$	$|f_{||}|$	below on same line			
							$f_{\perp x}$	$f_{\perp y}$	$f_{\perp z}$	$|f_\perp|$	$f_{\perp 2x}$	$f_{\perp 2y}$	$f_{\perp 2z}$	$|f_2|$

_n, _t, _p, _pot; Datafiles containing the coefficients of polynomial fits to density, temperature, pressure, and electric potential. These coefficients are generated by *b_glsin_gen* which calls the program *glsws*, an implementation of the Levenberg-Marquardt method.

$$
\begin{aligned}
f(x, y, z;p) = &\ [p_{000} + p_{001}z + p_{002}z^2 + p_{003}z^3 + p_{004}z^4 + p_{005}z^5] \\
&+ [p_{100} + p_{101}z + p_{102}z^2 + p_{103}z^3 + p_{104}z^4 + p_{105}z^5]x \\
&+ [p_{200} + p_{201}z + p_{202}z^2 + p_{203}z^3 + p_{204}z^4 + p_{205}z^5]x^2
\end{aligned}
$$

The datafile header is the polynomial degree in the x, y, and z directions. For example the above equation would have a header file with 2 0 5 and eighteen lines of polynomial coefficients p_{ijk} since $(2 + 1) \times (0 + 1) \times (5 + 1) = 18$.

_je; The _je datafiles are the electron currents calculated by *jelectron* using the method described in chapter three. Note that the _je datafiles cannot be calculated without the _n, _t, and _p coefficient files since n, T, and Φ are calculated from the polynomials.

x, R_E	y, R_E	z, R_E	n, m^3	T	Φ	j_x, A/m^2	j_y, A/m^2	j_z, A/m^2

_js; These datafiles are the sum of the ion and electron currents. The ion currents can be retrieved from the **njp_o** files.

x, R_E	y, R_E	z, R_E	j_x, A/m^2	j_y, A/m^2	j_z, A/m^2

Appendix F: PROGRAM SUBROUTINE SUMMARY

Main Program:
partrj.f: Trace charged particles in complex B and E fields.

Non-specific plotting routine:
get_pflag.f: Ask user if particles are to be plotted or run as batch
plotxyz.f: Plot the new step if this is the nplot'th point

General program Initialization:
filemenu.f: Set flags signaling what files will be needed.
filehelp.f: Describes relative data file sizes for user
partrj_io.f: Open all output data files for program partrj.f
vinject_menu.f: Menu of the different particle injection methods
inject_rndm.f: Randomizes the injection point: see pinject_menu
injhelp.f: Describes the different injection methods that can be used
scatopt.f: Ask user about activating random scattering option.
get_evans.f: Ask user for type of particle injection.
get_hemisp.f: Pitch angle preference for particle injection
get_method.f: Choose numerical method (Runge-Kutta or Bulirsch-Stoer)
get_pflag: Ask user if particles are to be plotted or run as batch
pinitial.f: Determine numerous initial parameters before tracing begins
pinject_menu.f: Set up the randomizer option in injection position
xyzstart.f: Get injection point in [Re]. Values converted to [meters].
getvelmx.f: Establish a maximum velocity for all f(v) calculations
set_foldflag.f: Get flags signaling what grid direction should be folded
set_hvnarr.f: Set the preferred normal coordinate
set_pcount.f: Ask user for the number of particles to be plotted or run.

Grid and Cutoff:
getboxes.f: Get the number of boxes for each lattice direction.
gcflags.f: Get flags signaling what range cutoff/gridding will occur.
gcflags.f: Orient user to gridding and cutoff method
gcvals.f: Queries for Cutoff & Gridding ranges (Returned in [Meters])
gridinit.f: Set up all the gridding of coordinate space for tracing.

Particle calculations:
parinp.f: This subroutine is called before starting EACH trajectory.
calcvepa: Select and calculate velocity, energy, pitch & phase angles
pitcha.f: Given (Tpar,Tperp), randomly select pitch & phase angles
calang.f: Calculate (Vx,Vy,Vz) given (x,y,z) and (Pitch,Phase) & Vo
change.f: Get parameters needed to determine the initial velocity vector.
epaphi.f: Calculate Energy and Pitch & Phase angles at (x,y,z)
vxvyvz.f: Evaluate (vx,vy,vz) given vmag, pitchr, phaser, thetab
f_pitch.f: .   Calculate angle between particle and field vectors (radians)

Forward tracing & Backtracking:

forward.f:	Setup ODE driver based on user choice of RK or BS method.
backtrack.f:	Backtrack to last edge crossed.
backtrold.f:	Interpolate pitch and phase angles to get box edge crossing
tracer.f:	See "Numerical Recipes" for details
	odeint(ystart,nvar,x1,x2,eps,h1,hmin,nok,nbad,
	rkqc(y,dydx,n,x,htry,eps,yscal,hdid,hnext,derivs)
	rk4(y,dydx,n,x,h,yout,derivs)
	bsstep(y,dydx,nv,x,htry,eps,yscal,hdid,hnext,derivs)
	mmid(y,dydx,nvar,xs,htot,nstep,yout,derivs)
	rzextr(iest,xest,yest,yz,dy,nv,nuse)
	pzextr(iest,xest,yest,yz,dy,nv,nuse)
derivs.f:	Calculates derivatives for $F = q(E + V \times B)$ and dr/ds & dV/ds
sortorder.f:	Sort the BACKRVT key ORDER by the time field
scatter:	Scatter a particle using Gaussian distribution

Box crossing:

kcalc.f:	Calculate box and edge numbers for the given position
kfold.f:	Fold box edge numbers to increase statistics
boxexitcheck.f:	Determine if backtracing is necessary and/or cut stepsize
boxselect.f:	Get the box numbers for output files.
incnjdata.f:	Update time and net distance traveled in the current box
multivalue.f:	Determine IF the stepsize should be reduced
stepcutter.f:	Determine HOW the stepsize should be reduced
finishcheck.f:	Signal end of tracing if simulation boundary exceeded

Buffer Stuff:

buffer.f:	Flush buffer since buffer full or trajectory completed.
dflush.f:	Use buffer values to update f(x,y,z), n(z), and J(x,y,z).
fbeupdate.f:	Update beginning and endpoint of trajectory
rvtupdate.f:	Update (r,V,t) trajectory array with new position
timeupdate.f:	Update the elapsed time for forward & backward tracing

Distribution function:

incdfap.f:	Increment the distribution function f(pitch,phase).
incdfvc.f:	Increment the distribution function f(Vx,Vy,Vz).
incdfvpp.f:	Increment the distribution function f(Vpar,Vperp).
fluid_fvc.f:	Calculate macroscopic plasma quantities using f(Vx,Vy,Vz).
setup_df.f:	Initialize the distribution function arrays to zero.
setup_nj.f:	Initialize n(z), Jx, Jy, and Jz for a single particle orbit.

Plasma Parameters from Box Crossing Method:

dencur.f:	Calculate the particle and current density for an orbit
nj_ave.f:	Calculate the average number and current densities.

Single Trajectory data products:

pcanonical.f: Calculate the canonical momentum, given the parameters.
moment.f: Calculate the magnetic moment and canonical momentum Py
jzinvr.f: Calculate Jx and Jz invariants at (x,y,z)
f_kappa.f: Calculate Buchner & Zelenyi Kappa parameter

Generate Output Files:

rw_header.f: READ or WRITE data file header with grid & model info
write_cp.f: Write out the Circle Plot data file.
write_df.f: Write f(alpha,phi) or f(Vpar,Vperp) distribution function.
write_if.f: Output initial and final trajectory data to a file.
write_nj.f: Write out the Current Density/Number Density data.
write_rkt.f: Write a file with (x,y,z,kappa,t)
write_rvt.f: Write a file with (x,y,z,Vx,Vy,Vz,t)

Debugging subroutines: All are in printout.f